Semiclassical Quantization for the States of Cuprous Oxide in Consideration of the Band Structure

Master's thesis of
Michael Marquardt

March 18, 2021

Examiner: Apl. Prof. Dr. Jörg Main
Co-Examiner: Prof. Dr. Maria Daghofer

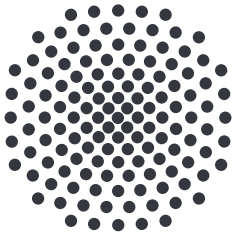

Institut für Theoretische Physik I
Universität Stuttgart
Pfaffenwaldring 57, 70550 Stuttgart

Contents

1 Introduction

Excitons are atom-like states in semiconductors like cuprous oxide (Cu_2O) formed by an electron and a positively charged hole. They are created by exciting an electron from the valence band into the conduction band where the electron forms a bound hydrogen-like state with the hole remaining in the valence band. In this thesis we will focus on excitons of the yellow series which have excitation energies corresponding to wavelengths of about 590 nm [1].

Excitons in cuprous oxide have been studied intensively in experiments [1–3] and quantum mechanical calculations [4, 5]. Those investigations showed that there are similarities to the hydrogen atom but also deviations caused by the band structure of the crystal. For the hydrogen atom it was possible to connect the quantum mechanical energy spectrum to classical Keplerian orbits in the Bohr-Sommerfeld model. The question arises whether this is possible for excitons in cuprous oxide as well.

Semiclassical trace formulas relate fluctuations of the density of states to classical periodic orbits where the frequencies are related to the action or period of the periodic orbits while the amplitude is related to stability properties of the orbits. In this thesis we want to apply semiclassical theories for the calculation and interpretation of exciton spectra.

In order to take the band structure of Cu_2O into account in classical calculations we treat the quasispin and hole spin degrees of freedom with an adiabatic approach. Thereby, we assume the spin dynamics to be much faster than the classical motion and calculate the spin-dependent part of the Hamiltonian quantum mechanically while the exciton dynamics is treated classically.

Cuprous oxide has a cubic O_h symmetry. Therefore, it has distinct symmetry planes in which two-dimensional classical exciton orbits occur. In order to simplify the problem we limit ourselves to orbits in the plane orthogonal to the [001] axis.

For investigating the classical exciton dynamics we show a Poincaré surface of section and search for periodic orbits in the plane. Furthermore, we calculate the action, period and stability properties of these orbits and use them for semiclassical calculations.

1.1 Structure of the thesis

In chapter 2 we present the theoretical foundations and methods. In section 2.1 we talk about the semiconductor cuprous oxide, its symmetries and the band structure. In section 2.2 we present the semiclassical trace formulas which allow for calculating the density of states from classical periodic orbits. In section 2.3 we show how to find and simulate classical exciton orbits and how to calculate the orbit parameters. In section 2.4 we will explain how to calculate the frequencies of a scaled energy spectrum in semiclassical calculations and we show a quantum mechanical equivalent we can compare with.

In chapter 3 we present our results. In section 3.1 we search for periodic orbits at constant $n_{\text{eff}} = 5$ and calculate the frequencies and amplitudes of the scaled spectrum semiclassically. In section 3.2 we investigate the energy dependence of the periodic-orbit parameters.

2 Theoretical foundations and methods

2.1 Excitons in cuprous oxide

Excitons are states in semiconductors. An electron is excited from the valence band into the conduction band and forms an atom-like structure with the hole remaining in the valence band. The early experiments with excitons were made in cuprous oxide (Cu_2O) by Gross [2]. Since then experimental techniques have made enormous progress and in 2014 Kazimierczuk et al. [1] realized excitons with principal quantum numbers up to $n = 25$ and extensions larger than 2 µm. They did their experiments in natural Cu_2O because, although it can be fabricated artificially [6, 7], natural Cu_2O is of better quality until now. One reason why cuprous oxide is used in exciton experiments quite frequently is that the excitation energy of the excitons corresponds to frequencies in the visible spectra. Another reason is that they have a high Rydberg energy and therefore a strong splitting of the energy levels and large radii [1].

An exciton consists of an electron and a hole both with a charge of $\pm e$ which looks quite similar to the hydrogen atom. Nevertheless, the exciton is affected by the band structure of the semiconductor which means that it does not share exactly the same Hamiltonian as the hydrogen atom. Also experiments showed a deviation from the hydrogen-like behavior [3].

2.1.1 Symmetry

Figure 2.1 shows the molecular structure of the semiconductor Cu_2O. It consists of copper atoms arranged in an fcc lattice and oxygen atoms arranged in a bcc lattice [10]. Both lattices are shifted by 1/4 of the lattice side against one another. The Cu_2O crystal has cubic O_h symmetry which is also projected onto the band structure and therefore the Hamiltonian of the system [11]. The symmetry operations of this symmetry group are listed in table 2.1.

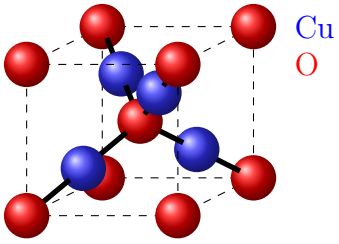

Figure 2.1: Molecular structure of cuprous oxide. The red oxygen atoms are arranged in a bcc lattice and the blue copper atoms are arranged in an fcc lattice shifted by 1/4 of the lattice side in each direction.

Table 2.1: Symmetry operations of the O_h group [8, 9].

Symmetry operation	Explanation
E	Identity
$8C_3$	Threefold rotations around the [111] axis and equivalents
$3C_2$	Twofold rotations around the [001] axis and equivalents
$6C_4$	Fourfold rotations around the [001] axis and equivalents
$6C_2$	Twofold rotations around the [110] axis and equivalents
I	Inversion
$8S_6$	Improper rotations around the [111] axis and equivalents
$6S_4$	Improper rotations around the [001] axis and equivalents
$3\sigma_\mathrm{h}$	Reflections at planes normal to the [001] axis and equivalents
$6\sigma_\mathrm{d}$	Reflections at planes normal to the [110] axis and equivalents

Table 2.2: Symmetry operations of the $C_{4\mathrm{v}}$ group [8, 9].

Symmetry operation	Explanation
E	Identity
C_2	Twofold rotations around the [001] axis
$2C_4$	Fourfold rotations around the [001] axis
$3\sigma_\mathrm{h}$	Reflections at planes normal to the [100] and [010] axis
$6\sigma_\mathrm{d}$	Reflections at planes normal to the [110] and $[\bar{1}10]$ axis

An n-fold rotation C_n means to rotate by multiples of $360°/n$ around the given axis. The $8C_3$ for example denotes a rotation by $\pm 120°$ around the axes [111], $[\bar{1}11]$, $[1\bar{1}1]$ and $[11\bar{1}]$. The 8 is the total number of non identical operations of this type which is the number of possible rotation angles times the number of possible axes. Note that a rotation by 120° around [111] would be identical with a rotation by $-120°$ around $[\overline{111}]$. There are only 6 C_4 operations because some of them would be identical with the C_2 operations. An improper rotation is a combination of a rotation and a reflection. It occurs when the system is a mirror image of itself after the rotation.

There are two different reflection operations in the O_h group. Also the Hamiltonian is reflected at these symmetry planes which means that classical trajectories in these planes will stay there forever [9, 12]. This will be important because we want to simulate classical exciton orbits and in order to simplify our system we limit ourselves to trajectories in the symmetry plane orthogonal to [001]. This makes the exciton orbits two-dimensional. The dynamics in the other σ_h symmetry planes will be the same but in the σ_d planes they will be different.

The symmetry group corresponding to the symmetry plane orthogonal to [001] is $C_{4\mathrm{v}}$. The knowledge of this symmetry can be useful when searching for starting conditions for periodic exciton orbits. The symmetry operations of the $C_{4\mathrm{v}}$ group are listed in table 2.2.

2.1.2 Band structure

Excitons in Cu_2O can be described through the Hamiltonian [5, 9, 11]

$$H = E_\mathrm{g} + H_\mathrm{e}(\boldsymbol{p}_\mathrm{e}) + H_\mathrm{h}(\boldsymbol{p}_\mathrm{h}, \boldsymbol{I}, \boldsymbol{S}_\mathrm{h}) + V(\boldsymbol{r}_\mathrm{e} - \boldsymbol{r}_\mathrm{h}) \tag{2.1}$$

with gap energy E_g, the momentum $\boldsymbol{p}$ dependent Hamiltonians of electron (e) and hole (h) so as the Coulomb potential $V(\boldsymbol{r}_\mathrm{e} - \boldsymbol{r}_\mathrm{h})$ depending on the distance between electron and hole $\boldsymbol{r}_\mathrm{e} - \boldsymbol{r}_\mathrm{h}$. The gap energy for cuprous oxide so as further material parameter can be seen in appendix B. The quasispin $\boldsymbol{I}$ is introduced in order to account for the cubic O_h symmetry of the system and interacts with the hole spin $\boldsymbol{S}_\mathrm{h}$. The corresponding hole

Hamiltonian reads

$$\begin{aligned} H_{\mathrm{h}}\left(\boldsymbol{p}_{\mathrm{h}}, \boldsymbol{I}, \boldsymbol{S}_{\mathrm{h}}\right) = H_{\mathrm{SO}}\left(\boldsymbol{I}, \boldsymbol{S}_{\mathrm{h}}\right) + \frac{1}{2\hbar^2 m_0}\Big[& \hbar^2(\gamma_1 + 4\gamma_2)\boldsymbol{p}_{\mathrm{h}}^2 \\ & +2(\eta_1 + 2\eta_2)\boldsymbol{p}_{\mathrm{h}}^2\left(\boldsymbol{I}\cdot\boldsymbol{S}_{\mathrm{h}}\right) \\ & -6\gamma_2\left[p_{\mathrm{h}1}^2 I_1^2 + \text{c.p.}\right] \\ & -12\eta_2\left[p_{\mathrm{h}1}^2 I_1 S_{\mathrm{h}1} + \text{c.p.}\right] \\ & -12\gamma_3\left[\{p_{\mathrm{h}1}, p_{\mathrm{h}2}\}\{I_1, I_2\} + \text{c.p.}\right] \\ & -12\eta_3\left[\{p_{\mathrm{h}1}, p_{\mathrm{h}2}\}\left(I_1 S_{\mathrm{h}2} + I_2 S_{\mathrm{h}1}\right) + \text{c.p.}\right]\Big] \end{aligned} \tag{2.2}$$

where c.p. means the cyclic permutation of the indices (e.g $I_1 I_2 + c.p. = I_1 I_2 + I_2 I_3 + I_3 I_1$) and with the symmetric product $\{A, B\} = \frac{1}{2}(AB + BA)$. The mass m_0 is the standard electron mass and γ_i and η_i are the Luttinger parameters [3, 4] which result from fits to experimental data. They account for the effective mass of the hole in the crystal lattice. As one can see it depends on the direction of the momentum as well as on the spins. The term H_{SO} in the Hamiltonian denotes the spin-orbit coupling

$$H_{\mathrm{SO}}\left(\boldsymbol{I}, \boldsymbol{S}_{\mathrm{h}}\right) = \frac{2}{3}\Delta\left(\mathbb{1} + \frac{1}{\hbar^2}\boldsymbol{I}\cdot\boldsymbol{S}_{\mathrm{h}}\right) \tag{2.3}$$

with parameter Δ and identity $\mathbb{1}$.

The electron Hamiltonian is just the momentum term

$$H_{\mathrm{e}}(\boldsymbol{p}_{\mathrm{e}}) = \frac{\boldsymbol{p}_{\mathrm{e}}^2}{2m_{\mathrm{e}}} \tag{2.4}$$

where m_{e} is the effective mass of the electron in the conductance band.

The Coulomb potential is

$$V(\boldsymbol{r}_{\mathrm{e}} - \boldsymbol{r}_{\mathrm{h}}) = \frac{e^2}{4\pi\varepsilon\varepsilon_0|\boldsymbol{r}_{\mathrm{e}} - \boldsymbol{r}_{\mathrm{h}}|} \tag{2.5}$$

with the dielectric constant ε.

Combining all components and expressing the system in relative and center-of-mass

coordinates

$$\begin{aligned} M &= m_\mathrm{h} + m_\mathrm{e}, \\ \mu &= \frac{m_\mathrm{h} + m_\mathrm{e}}{m_\mathrm{h} m_\mathrm{e}}, \\ \boldsymbol{r} &= \boldsymbol{r}_\mathrm{h} - \boldsymbol{r}_\mathrm{e}, \\ \boldsymbol{p} &= \frac{m_\mathrm{e}\boldsymbol{p}_\mathrm{h} - m_\mathrm{h}\boldsymbol{p}_\mathrm{e}}{M}, \\ \boldsymbol{R} &= \frac{m_\mathrm{h}\boldsymbol{r}_\mathrm{h} + m_\mathrm{e}\boldsymbol{r}_\mathrm{e}}{M}, \\ \boldsymbol{P} &= \boldsymbol{p}_\mathrm{h} + \boldsymbol{p}_\mathrm{e}, \end{aligned} \tag{2.6}$$

the Hamiltonian reads

$$H = E_\mathrm{g} + \frac{\boldsymbol{p}^2}{2m_\mathrm{e}} + H_\mathrm{h}\left(\boldsymbol{p}, \boldsymbol{I}, \boldsymbol{S}_\mathrm{h}\right) - \frac{e^2}{4\pi\varepsilon\varepsilon_0|\boldsymbol{r}|} \tag{2.7}$$

where the center-of-mass momentum $\boldsymbol{P}$ is neglected. Introducing the new parameter $\gamma_1' = \gamma_1 + m_0/m_e$ the Hamiltonian changes to

$$H = \frac{\gamma_1'\boldsymbol{p}^2}{2m_0} - \frac{e^2}{4\pi\varepsilon\varepsilon_0 r} + \tilde{H}_\mathrm{b}\left(\boldsymbol{p}_\mathrm{h}, \boldsymbol{I}, \boldsymbol{S}_\mathrm{h}\right) \tag{2.8}$$

with

$$\begin{aligned} \tilde{H}_\mathrm{b}\left(\boldsymbol{p}_\mathrm{h}, \boldsymbol{I}, \boldsymbol{S}_\mathrm{h}\right) = E_\mathrm{g} & \\ + \frac{2}{3}\Delta\left(\mathbb{1} + \frac{1}{\hbar^2}\boldsymbol{I}\cdot\boldsymbol{S}_\mathrm{h}\right) & \\ + \frac{2\gamma_2}{\hbar^2 m_0}\boldsymbol{p}^2 & \\ + \frac{\eta_1 + 2\eta_2}{\hbar^2 m_0}\boldsymbol{p}^2\left(\mathbb{1} + \boldsymbol{I}\cdot\boldsymbol{S}_\mathrm{h}\right) & \\ - \frac{3\gamma_2}{\hbar^2 m_0}\left[p_1^2 I_1^2 + \text{c.p.}\right] & \\ - \frac{6\eta_2}{\hbar^2 m_0}\left[p_1^2 I_1 S_{\mathrm{h}1} + \text{c.p.}\right] & \\ - \frac{6\gamma_3}{\hbar^2 m_0}\left[\{p_1, p_2\}\{I_1, I_2\} + \text{c.p.}\right] & \\ - \frac{6\eta_3}{\hbar^2 m_0}\left[\{p_1, p_2\}\left(I_1 S_{\mathrm{h}2} + I_2 S_{\mathrm{h}1}\right) + \text{c.p.}\right]. & \end{aligned} \tag{2.9}$$

Besides $\boldsymbol{r}$ and $\boldsymbol{p}$ additional degrees of freedom arise in the Hamiltonian because of the quasispin $\boldsymbol{I}$ and the hole spin $\boldsymbol{S}_\mathrm{h}$. Furthermore, we shift the energy by $-E_\mathrm{g}$ what eliminates it in the Hamiltonian.

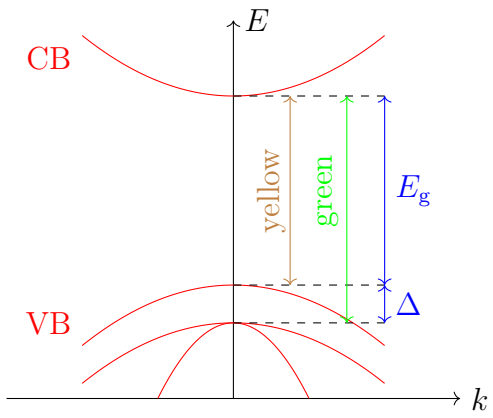

Figure 2.2: Schematic plot of the band structure of cuprous oxide. One can see the conduction band (CB) and the valence band (VB) which is split up due to spin-orbit coupling (Δ) and the interaction of the hole spin with the crystal lattice. The excitons are divided in series named according to the energy which is necessary to excite an electron from the VB to the CB. In this thesis we investigate excitons of the yellow series.

A schematic view of the band structure of cuprous oxide is shown in figure 2.2. The valence band splits up because of the band structure term $\tilde{H}_\mathrm{b}\left(\boldsymbol{p}_\mathrm{h}, \boldsymbol{I}, \boldsymbol{S}_\mathrm{h}\right)$ in the Hamiltonian (2.8). The excitons are classified in series according to their excitation energy. There are the yellow, green, blue and violet series but since the both last arise from a splitting of the conduction band they are not considered in our Hamiltonian [11]. In this thesis we want to investigate excitons of the yellow series which belongs to a total spin of $\boldsymbol{I} + \boldsymbol{S}_\mathrm{h} = 1/2$ and which have excitation energies corresponding to wavelengths of about 590 nm [1].

2.1.3 Quantum mechanical treatment of excitons in cuprous oxide

Energy spectra of the yellow exciton series are already measured experimentally [1, 13, 14] and invested quantum mechanically [3, 13, 14]. In order to get the energy spectrum one can solve the quantum mechanical Hamiltonian in a complete basis [5, 11, 15]. Those investigations revealed that there are significant deviations from the hydrogen-like series. One can introduce a quantum defect $\delta_{n,l}$ describing the energy levels as

$$E_{n,l} = -\frac{\mathrm{Ry}}{(n-\delta_{n,l})^2} \tag{2.10}$$

with principal quantum number n and azimuthal quantum number l in analogy to the hydrogen atom [16]. With the quantum defects a new effective quantum number $n_\mathrm{eff} = n - \delta_{n,l}$ is introduced. The factor Ry is the ideal Rydberg energy in the hydrogen-like case and for the excitons in Cu_2O it is

$$\mathrm{Ry} = \frac{\hbar^2 \gamma_1'}{2 a_\mathrm{exc}^2 m_0} \tag{2.11}$$

with

$$a_{\text{exc}} = \frac{4\pi\varepsilon\varepsilon_0\hbar^2\gamma_1'}{e^2 m_0}. \tag{2.12}$$

In analogy to the hydrogen atom we can introduce exciton-Hartree units with

$$e = \frac{m_0}{\gamma_1'} = \hbar = \frac{1}{4\pi\varepsilon\varepsilon_0} \equiv 1. \tag{2.13}$$

The new units can be found in appendix C.

2.2 Semiclassical theories

Now that we have seen the quantum mechanical treatment of excitons it is time to explain some semiclassical theories. The idea behind semiclassical theories is that one can use classical dynamics in order to derive quantum mechanical quantities, especially the energy density. We will start with torus quantization because of didactic reasons. Then the Barry-Tabor formula and Gutzwiller's trace formula are derived. They allow for calculating the energy density from the sum over all classical periodic exciton orbits. In this thesis we will actually not calculate an energy density but it's Fourier transform. This allows for investigating which classical exciton orbits are responsible for which peaks and comparing this to the Fourier transform of a corresponding quantum mechanical spectrum. In order to make the prefactor clear and to be convenient with books and lectures we do not use exciton-Hartree units in this section.

2.2.1 Torus quantization

Torus quantization is one method for calculating quantized energy levels from classical systems [17]. We start with the WKB method (Wenzel, Kramer, Brillouin) for a one-dimensional system with position q and momentum p oscillating between two points $q = a, b$. With energy E and potential V we can write down the Schrödinger equation as

$$\Psi'' + \frac{2m}{\hbar^2}(E - V(q))\Psi = 0. \tag{2.14}$$

We make the ansatz

$$\Psi(q) = A(q)\exp\left(\mathrm{i}\frac{S(q)}{\hbar}\right) \tag{2.15}$$

for the wave function Ψ. By evaluating equation (2.14) one finds

$$A \propto (S')^{-1/2}, \tag{2.16}$$

$$S'^2 = 2m(E-V) + \hbar^2 \left[\frac{3}{4} \left(\frac{S''}{S'} \right)^2 - \frac{1}{2} \frac{S'''}{S'} \right]. \tag{2.17}$$

Neglecting terms in $\hbar^2$ leads to

$$S(q) \approx \pm \int \sqrt{2m(E-V(q))}\, \mathrm{d}q = \pm \int p\, \mathrm{d}q. \tag{2.18}$$

The problem is that A diverges for $p = 0$ and therefore at the turning points ($q = a, b$). One can solve this problem by linearizing the potential near those points with

$$E - V(q) \approx F_0(q-a), \tag{2.19}$$

or with b instead of a. After some calculations and comparisons the resulting semiclassical wave function turns out to be

$$\Psi(q) \propto \cos\left(\frac{1}{\hbar} \int_q^a p\, \mathrm{d}q' - \frac{\pi}{4} \right) \overset{!}{\propto} \cos\left(\frac{1}{\hbar} \int_b^q p\, \mathrm{d}q' - \frac{\pi}{4} \right). \tag{2.20}$$

It follows the quantization condition for bound states

$$\int_b^a p\, \mathrm{d}q = \pi\hbar \left(n + \frac{1}{2} \right), \qquad n \in \mathbb{N}_0. \tag{2.21}$$

The integration equals the classical action over half the period of a periodic movement.

As mentioned above this is only applicable for one-dimensional systems. Usually one wants to treat two- or three-dimensional systems. At this point torus quantization comes into play. It looks for the points where the action S has singularities or caustics and defines it piece by piece as $S(\boldsymbol{q})$ or $\overline{S}(\boldsymbol{p})$ with

$$\overline{S}(\boldsymbol{p}) = S(\boldsymbol{q}) - \boldsymbol{p}\boldsymbol{q}, \tag{2.22}$$

$$\boldsymbol{q} = -\boldsymbol{\nabla}_{\boldsymbol{p}} \overline{S}, \tag{2.23}$$

$$0 = H\left(-\boldsymbol{\nabla}_{\boldsymbol{p}} \overline{S}, \boldsymbol{p} \right) - E. \tag{2.24}$$

For the one-dimensional case the Maslov index function is defined as

$$\sigma_p(t) = \sigma_q(t) - \operatorname{sign}\left(\frac{\mathrm{d}p}{\mathrm{d}q} \right) \tag{2.25}$$

where t is some variable like time describing the path. The function is defined as σ_q in each q sector and analogously for p.

Every time a singularity or caustic is passed the space is changed from q to p sector or the other way around and the function increases or decreases by one. The Maslov index is defined as

$$\mu \equiv \frac{[\sigma]}{2} \tag{2.26}$$

where $[\sigma]$ denotes the change of σ over one period.

The semiclassical wave function is now defined as

$$\Psi(q) = B(q) \exp\left(\mathrm{i} \left[\frac{S(q)}{\hbar} - \sigma_q \frac{\pi}{4} \right] \right) \qquad \text{in each } q \text{ sector}, \tag{2.27}$$

$$\Psi(p) = \overline{B}(p) \exp\left(\mathrm{i} \left[\frac{\overline{S}(p)}{\hbar} - \sigma_p \frac{\pi}{4} \right] \right) \qquad \text{in each } p \text{ sector}, \tag{2.28}$$

where the phase experiences a shift at every singularity or caustic. The amplitude B is not of interest at the moment but evaluating the phase one gets the quantization condition

$$[S] = 2\pi\hbar \left(n + \frac{\alpha}{4} \right), \qquad n \in \mathbb{N}_0 \tag{2.29}$$

which equals (2.21) where $\alpha = 2$ because a one-dimensional vibration needs four changes between q and p sector (four points where $\mathrm{d}p/\mathrm{d}q$ changes sign).

In N dimensions the singularities/caustics occur at $\det \left| \frac{\partial p_l}{\partial q_m} \right| = 0$ which is why the Maslov index function is defined as

$$\sigma_{\boldsymbol{p}}(t) = \sigma_{\boldsymbol{q}}(t) - \operatorname{sgn}\left(\frac{\partial p_l}{\partial q_m} \right) \tag{2.30}$$

with

$$\operatorname{sgn}\left(\frac{\partial p_l}{\partial q_m} \right) = \sum_{i=1}^{N} \operatorname{sign}(\lambda_i), \tag{2.31}$$

where λ_i are the eigenvalues of the matrix $\frac{\partial p_l}{\partial q_m}$. In analogy to the one-dimensional system the quantization condition is

$$[S]_{C_k} = 2\pi\hbar \left(n_k + \frac{\alpha_k}{4} \right), \qquad n \in \mathbb{N}_0 \tag{2.32}$$

where C_k describes one of N independent paths on the torus. This leads to N quantum numbers n_k. The problem with this is that it is difficult to find these paths C_k. The Berry-Tabor formula which is presented in the following does not use the paths C_k but periodic orbits instead.

2.2.2 Berry-Tabor formula

In order to derive the Berry-Tabor formula for two-dimensional systems we start with the EKB quantization (Einstein, Keller, Brillouin) [17, 18]. It uses the ansatz

$$J_k = \hbar\left(n_k + \frac{\mu_k}{4}\right), \qquad n_k \in \mathbb{N}_0, \tag{2.33}$$

$$E(\boldsymbol{n}) = H(\boldsymbol{J}) \tag{2.34}$$

for the action variables J_k which is similar to the quantization condition from torus quantization. For an integrable system with dimension $N = 2$ the density of states is then given by

$$\rho(E) = \sum_{n_1=0}^{\infty}\sum_{n_2=0}^{\infty}\delta(E - E(n_1, n_2)) \tag{2.35}$$

which can be transformed into

$$\begin{aligned}\rho(E) = &\sum_{M_1,M_2=-\infty}^{\infty}\int \mathrm{d}n_1 \int \mathrm{d}n_2\, \delta(E - E(n_1, n_2))\exp(2\pi\mathrm{i}(M_1 n_1 + M_2 n_2)) \\ &+ \frac{1}{2}\sum_{M=-\infty}^{\infty}\int \mathrm{d}n_1\, \delta(E - E(n_1, 0))\exp(2\pi\mathrm{i}M n_1) \\ &+ \frac{1}{2}\sum_{M=-\infty}^{\infty}\int \mathrm{d}n_2\, \delta(E - E(0, n_2))\exp(2\pi\mathrm{i}M n_2) \\ &+ \frac{1}{4}\delta(E - E(0, 0))\end{aligned} \tag{2.36}$$

by using Poisson's summation formula. The second and third term can be treated as a semiclassical correction of order $\hbar$ and the fourth term is not of interest here because it is connected only to one specific energy $E(0, 0)$. The equation is therefore reduced to the first term which is called $\rho^{(2)}(E)$ in the following. By using (2.33) one can write it as

$$\begin{aligned}\rho^{(2)}(E) = &\frac{1}{\hbar^2}\sum_{M_1,M_2}\exp\Big(-\mathrm{i}\frac{\pi}{2}(M_1\mu_1 + M_2\mu_2)\Big) \\ &\times \int_{\hbar\mu_1/4}^{\infty}\mathrm{d}J_1 \int_{\hbar\mu_2/4}^{\infty}\mathrm{d}J_2\, \delta(E - H(J_1, J_2))\exp\left(\frac{2\pi\mathrm{i}}{\hbar}(M_1 J_1 + M_2 J_2)\right).\end{aligned} \tag{2.37}$$

The term with $M_1 = M_2 = 0$ is called Thomas-Fermi term

$$\tilde{\rho}^{(2)}(E) = \frac{1}{(2\pi\hbar)^2}\int \mathrm{d}\boldsymbol{p}\int \mathrm{d}\boldsymbol{q}\, \delta(E - H(\boldsymbol{p}, \boldsymbol{q})). \tag{2.38}$$

It is the mean density of states. The remaining oscillating part is calculated by replacing the delta function with

$$\delta(x) = \frac{1}{2\pi\hbar}\int_{-\infty}^{\infty} \exp\Big(\mathrm{i}\frac{\tau x}{\hbar}\Big)\,\mathrm{d}\tau. \tag{2.39}$$

It becomes

$$\delta\rho^{(2)}(E) = \frac{1}{2\pi\hbar^3}\sum_{M_1\neq 0\neq M_2} \exp\Big(-\mathrm{i}\frac{\pi}{2}\boldsymbol{M}\boldsymbol{\mu}\Big)\int \mathrm{d}J_1 \int \mathrm{d}J_2\, \exp(\mathrm{i}\phi(\boldsymbol{J})), \tag{2.40}$$

$$\phi(\boldsymbol{J}) = \frac{1}{\hbar}\left(2\pi\boldsymbol{M}\boldsymbol{J} + \tau(E - H(\boldsymbol{J}))\right). \tag{2.41}$$

The term oscillates strongly except for the stationary phase $\boldsymbol{\nabla}\phi(\boldsymbol{J}) = 0$ which leads to

$$2\pi M_i = \tau\omega_i(J_1, J_2) = \tau\frac{\partial H}{\partial J_i}, \tag{2.42}$$

$$\frac{M_1}{M_2} = \frac{\omega_1}{\omega_2} \in \mathbb{Q}. \tag{2.43}$$

The M_i turn out to be winding numbers of resonant tori which means that only periodic orbits contribute to $\rho^{(2)}(E)$. After some further calculations the Berry-Tabor formula for integrable systems is derived:

$$\rho^{(2)}(E) = \tilde{\rho}^{(2)}(E) + \sum_{\boldsymbol{M}\neq 0}\frac{T_{\boldsymbol{M}}}{\pi\sqrt{\hbar^3 M_2^3|g_E''|}}\cos\left(\frac{S_{\boldsymbol{M}}}{\hbar} - \frac{\pi}{2}\sigma_{\boldsymbol{M}} - \frac{\pi}{4}\right) \tag{2.44}$$

Thereby $T_{\boldsymbol{M}}$ is the period and $S_{\boldsymbol{M}}$ the action of the periodic orbit with winding number $\boldsymbol{M} = (M_1, M_2)$. The function g_E defines the relation between the both action variables on the energy surface via

$$E = H(J_1, J_2 = g_E(J_1)). \tag{2.45}$$

The Maslov index $\sigma_{\boldsymbol{M}}$ is defined as

$$\sigma_{\boldsymbol{M}} = \sum_{i=1}^{2}\mathrm{sign}(\lambda_i) \tag{2.46}$$

with λ_i being the eigenvalues of the Hesse matrix $\partial^2 H/\partial J_i\partial J_j$.

As with the torus quantization before we have the problem that the Berry-Tabor formula is limited to a fixed number of dimensions. Gutzwiller's trace formula which is derived in the following is applicable for arbitrary dimensions.

2.2.3 Gutzwiller's trace formula

In order to derive Gutzwiller's trace formula for isolated orbits [17, 19, 20] one starts from the retarded Green's function

$$G_E^+ = \sum_n \frac{|n\rangle \langle n|}{E - E_n + i\varepsilon} \tag{2.47}$$

with states $|n\rangle$ and energy eigenvalues E_n. The density of states can be expressed through this operator as

$$\rho(E) = \sum_n c_n \delta(E - E_n) = -\frac{1}{\pi} \operatorname{Im}\left(\operatorname{tr}\left(G_E^+\right)\right) \tag{2.48}$$

by using

$$\frac{1}{x + i\varepsilon} = P\frac{1}{x} - \mathrm{i}\pi\delta(x) \tag{2.49}$$

with the Cauchy principal value P. The Green's operator can be expressed through the quantum mechanical propagator $K_{\mathrm{qm}}(\boldsymbol{q}, t, \boldsymbol{q}', t' = 0)$ as

$$\begin{aligned} G_E^+(\boldsymbol{q}, \boldsymbol{q}') &= \sum_n \frac{\langle \boldsymbol{q}|n\rangle \langle n|\boldsymbol{q}'\rangle}{E - H + \mathrm{i}\varepsilon} \\ &= \frac{1}{i\hbar} \int_0^\infty \mathrm{d}t \, \exp\left(\frac{\mathrm{i}}{\hbar}(E + \mathrm{i}\varepsilon)t\right) \sum_n \Psi_n^*(\boldsymbol{q}) \Psi_n(\boldsymbol{q}') \exp\left(-\frac{\mathrm{i}}{\hbar} E_n t\right) \\ &= \frac{1}{i\hbar} \int_0^\infty \mathrm{d}t \, \exp\left(\frac{\mathrm{i}}{\hbar}(E + \mathrm{i}\varepsilon)t\right) K_{\mathrm{qm}}(\boldsymbol{q}, t, \boldsymbol{q}', t' = 0). \end{aligned} \tag{2.50}$$

The propagator can be expressed through Feynman's path integrals and then be brought to the semiclassical Van-Vleck formula

$$K_{\mathrm{SCL}}(\boldsymbol{q}, t, \boldsymbol{q}', t' = 0) = (2\pi\mathrm{i}\hbar)^{-N/2} \sum_{\mathrm{SCL}} \sqrt{|c|} \exp\left(\frac{\mathrm{i}}{\hbar} R(\boldsymbol{q}, \boldsymbol{q}', t) - \mathrm{i}\frac{\pi}{2}\kappa\right) \tag{2.51}$$

by using stationary phase approximation. The sum is taken over all classical trajectories with same start and end point $\boldsymbol{q} = \boldsymbol{q}'$. The variables are

$$R(\boldsymbol{q}, \boldsymbol{q}', t) = \int_0^\infty \mathrm{d}\tau \, L(\dot{\boldsymbol{q}}, \boldsymbol{q}, \tau), \tag{2.52}$$

$$c = \det\left(\frac{\partial^2 R}{\partial \boldsymbol{q} \partial \boldsymbol{q}'}\right), \tag{2.53}$$

with Lagrange function L and κ is the number of caustics along the path. Inserting this in Green's function and using stationary phase approximation ($E = -\dot{R}(t_0 = 0)$) leads to

$$G^+_{E,\mathrm{SCL}} = \frac{2\pi}{(2\pi \mathrm{i}\hbar)^{(N+1)/2}} \sum_{\text{SCL, } E \text{ fixed}} \sqrt{|D|} \exp\Big\{ \mathrm{i} S(\boldsymbol{q}, \boldsymbol{q}', E) - \mathrm{i}\frac{\pi}{2}\mu \Big\} \tag{2.54}$$

with action

$$S(\boldsymbol{q}, \boldsymbol{q}', E) = R(\boldsymbol{q}, \boldsymbol{q}', t) + Et = \int_{\boldsymbol{q}'}^{\boldsymbol{q}} \boldsymbol{p} \mathrm{d}\tilde{\boldsymbol{q}}, \tag{2.55}$$

the determinant

$$D = \frac{c}{(\frac{\partial^2 R}{\partial t^2})_{t_0}} = \det \begin{pmatrix} \frac{\partial^2 S}{\partial \boldsymbol{q} \partial \boldsymbol{q}'} & \frac{\partial^2 S}{\partial \boldsymbol{q}' \partial E} \\ \frac{\partial^2 S}{\partial \boldsymbol{q} \partial E} & \frac{\partial^2 S}{\partial E \partial E} \end{pmatrix} \tag{2.56}$$

and the Maslov index

$$\mu = \begin{cases} \kappa & \frac{\partial^2 R}{\partial t^2}|_{t_0} > 0, \\ \kappa + 1 & \frac{\partial^2 R}{\partial t^2}|_{t_0} \leq 0. \end{cases} \tag{2.57}$$

The density $\rho(E)$ is now split up into a fluctuating part $\rho_{\mathrm{fl}}(E)$ and an average density

$$\tilde{\rho}(E) = \frac{1}{(2\pi\hbar)^N} \int \mathrm{d}\boldsymbol{p}\, \mathrm{d}\boldsymbol{q}\, \delta(E - H(\boldsymbol{p}, \boldsymbol{q})) \tag{2.58}$$

called the Thomas-Fermi term. It is the N-dimensional version of equation (2.38). The fluctuating part is

$$\rho_{\mathrm{fl}}(E) = -\frac{1}{\pi} \mathrm{Im} \left\{ \frac{2\pi}{(2\pi \mathrm{i}\hbar)^{(N+1)/2}} \int \mathrm{d}\boldsymbol{q} \sum_{\mathrm{CT}} |D|^{1/2} \exp\left(\frac{\mathrm{i} S(\boldsymbol{q}, \boldsymbol{q}, E)}{\hbar} - \mathrm{i}\mu\frac{\pi}{2} \right) \right\}. \tag{2.59}$$

The sum goes over all closed trajectories (CT). Another stationary phase with

$$0 = \left(\frac{\partial S(\boldsymbol{q}, \boldsymbol{q}, E)}{\partial \boldsymbol{q}} \right)_{\boldsymbol{q}_0} = \left(\frac{\partial S(\boldsymbol{q}, \boldsymbol{q}', E)}{\partial \boldsymbol{q}} + \frac{\partial S(\boldsymbol{q}, \boldsymbol{q}', E)}{\partial \boldsymbol{q}'} \right)_{\boldsymbol{q}=\boldsymbol{q}'=\boldsymbol{q}_0} = \boldsymbol{p} - \boldsymbol{p}' \tag{2.60}$$

leads to the momentum $\boldsymbol{p}$ being equal at start and end of the trajectory. This is why only periodic orbits contribute to the sum. Splitting the position into $\boldsymbol{q} = (x, q_{\perp,1}, ..., q_{\perp,N-1}) = (x, \boldsymbol{q}_\perp)$ where x is locally the coordinate parallel to trajectory allows for transforming the determinant into

$$D = -\frac{\partial^2 S}{\partial E \partial x} \frac{\partial^2 S}{\partial E \partial x'} \det\left(\frac{\partial S}{\partial \boldsymbol{q}_\perp \partial \boldsymbol{q}'_\perp} \right) = (-1)^N \frac{1}{\dot{x}\dot{x}'} \det\left(\frac{\partial \boldsymbol{p}'_\perp}{\partial \boldsymbol{q}_\perp} \right). \tag{2.61}$$

Linearizing the action near the periodic orbit leads to

$$S(\boldsymbol{q},\boldsymbol{q},E) = \underbrace{\oint \boldsymbol{p}\,\mathrm{d}\boldsymbol{q}}_{S_{\mathrm{PO}}} + \frac{1}{2}\sum_{i,j=1}^{N-1} W_{ij}(x) q_{\perp,i} q_{\perp,j}, \tag{2.62}$$

$$W_{ij}(x) = \left(\frac{\partial^2 S}{\partial \boldsymbol{q}_\perp \partial \boldsymbol{q}_\perp} + \frac{\partial^2 S}{\partial \boldsymbol{q}_\perp \partial \boldsymbol{q}'_\perp} + \frac{\partial^2 S}{\partial \boldsymbol{q}'_\perp \partial \boldsymbol{q}_\perp} + \frac{\partial^2 S}{\partial \boldsymbol{q}'_\perp \partial \boldsymbol{q}'_\perp}\right)_{\boldsymbol{q}_\perp = \boldsymbol{q}'_\perp = 0}. \tag{2.63}$$

Inserting this and integrating over the orthogonal components using Fresnel integrals the density can be transformed into

$$\rho_{\mathrm{fl}}(E) = -\frac{1}{\pi}\,\mathrm{Im}\left\{\frac{1}{\mathrm{i}\hbar}\sum_{\mathrm{PO}} \exp\left(\mathrm{i}\frac{S_{\mathrm{PO}}}{\hbar} - \mathrm{i}\frac{\pi}{2}(\mu+\nu)\right)\int \mathrm{d}x\,|D(x)|^{1/2}|\det(\boldsymbol{W}(x))|^{-1/2}\right\} \tag{2.64}$$

where the determinants can be replaced with

$$\left|\frac{\det \boldsymbol{W}(x)}{D(x)}\right| = \dot{x}^2 |\det(\boldsymbol{M}_{\mathrm{PO}} - \mathbb{1})| \tag{2.65}$$

with the monodromy matrix $\boldsymbol{M}_{\mathrm{PO}}$. The integral then reduces to

$$\int \mathrm{d}x\,\frac{1}{\dot{x}} = \int_{\mathrm{PPO}} \mathrm{d}t \frac{\dot{x}}{\dot{x}} = T_{\mathrm{PPO}} \tag{2.66}$$

where the integral is taken over the primitive periodic orbit (PPO) which is the underlying orbit with the lowest possible time period T_{PPO}.

This finally leads to Gutzwiller's trace formula

$$\rho(E) = \tilde{\rho}(E) + \frac{1}{\pi\hbar}\sum_{\mathrm{PO}} \frac{T_{\mathrm{PPO}}}{\sqrt{|\det(\boldsymbol{M}_{\mathrm{PO}} - \mathbb{1})|}} \cos\left(\frac{S_{\mathrm{PO}}}{\hbar} - \frac{\pi}{2}\sigma_{\mathrm{PO}}\right) \tag{2.67}$$

with Maslov index $\sigma_{\mathrm{PO}} = \mu + \nu$. Besides the Maslov index it contains only the time period T_{PPO}, the monodromy matrix $\boldsymbol{M}_{\mathrm{PO}}$ and the action S_{PO}. All of these orbit parameters can be calculated in simulations of classical exciton orbits.

2.3 Investigation of the classical exciton dynamics

In the previous chapter we have seen how to compare classical results to quantum mechanical calculations by using trace formulas. In this section we will see how the

classical orbits are simulated and how the relevant parameters are calculated, namely the action, period and monodromy matrix. At first the treatment of the additional degrees of freedom through quasispin and hole spin is explained. Then the simulation of classical orbits is explained including the problem of finding starting conditions for periodic orbits. We continue with introducing the stability matrix from which the monodromy matrix is a submatrix. The chapter is closed by explaining how the necessary parameters can be calculated from the simulations.

2.3.1 Adiabatic approach

The Hamiltonian of our system (2.8) depends on the position and the momentum but also on the quasispin and the hole spin which introduces additional degrees of freedom. Earlier investigations showed that it is not suitable to treat the spin dynamics classically [21, 22]. Therefore, the spin dependence of the Hamiltonian is treated quantum mechanically.

At first we make an adiabatic approach which means that we consider the spin dynamics being much faster than the exciton motion [9, 23]. The wave function can now be expressed as product

$$\Psi = \Phi(\boldsymbol{p})X(\boldsymbol{p}, \boldsymbol{I}, \boldsymbol{S}_\mathrm{h}) \tag{2.68}$$

of a part Φ only depending on the momentum and a part X which depends also on the spins. This wave function fulfills the stationary Schrödinger equation

$$E_n\Psi = \left[\frac{\boldsymbol{p}^2}{2} - \frac{1}{r} + \tilde{H}_\mathrm{b}(\boldsymbol{p}, \boldsymbol{I}, \boldsymbol{S}_\mathrm{h})\right]\Psi \tag{2.69}$$

with energy eigenvalues E_n. The spin-dependent part acts on the band-structure term as

$$W_n(\boldsymbol{p})X = \tilde{H}_\mathrm{b}(\boldsymbol{p}, \boldsymbol{I}, \boldsymbol{S}_\mathrm{h})X, \tag{2.70}$$

with momentum dependent eigenvalues $W_n(\boldsymbol{p})$. The equation can be solved quantum mechanically for a fixed position and momentum because we assume the spins to react almost instantaneously to changes in $\boldsymbol{r}$ and $\boldsymbol{p}$.

This is done by introducing a matrix representation in the basis of combined quasispin and the hole spin as

$$\begin{pmatrix} |1, 1/2, & 1, & 1/2\rangle \\ |1, 1/2, & 1, & -1/2\rangle \\ |1, 1/2, & 0, & 1/2\rangle \\ |1, 1/2, & 0, & -1/2\rangle \\ |1, 1/2, & -1, & 1/2\rangle \\ |1, 1/2, & -1, & -1/2\rangle \end{pmatrix} \tag{2.71}$$

with states $|j_I, j_{S_\mathrm{h}}, m_I, m_{S_\mathrm{h}}\rangle$ where j, m are the quantum numbers of the corresponding spins. This leads to a 6×6 matrix form of the spin Hamiltonian

$$\begin{aligned}
\tilde{H}_\mathbf{b} = & \frac{2}{3}\Delta\left(\mathbb{1} + \boldsymbol{I}\cdot\boldsymbol{S}_\mathrm{h}\right) \\
& + \frac{2\gamma_2}{\gamma_1'}\boldsymbol{p}^2 \\
& + \frac{\eta_1 + 2\eta_2}{\gamma_1'}\boldsymbol{p}^2\left(\mathbb{1} + \boldsymbol{I}\cdot\boldsymbol{S}_\mathrm{h}\right) \\
& - \frac{3\gamma_2}{\gamma_1'}\left[p_1^2 I_1^2 + \text{c.p.}\right] \\
& - \frac{6\eta_2}{\gamma_1'}\left[p_1^2 I_1 S_{\mathrm{h}1} + \text{c.p.}\right] \\
& - \frac{6\gamma_3}{\gamma_1'}\left[\{p_1, p_2\}\{I_1, I_2\} + \text{c.p.}\right] \\
& - \frac{6\eta_3}{\gamma_1'}\left[\{p_1, p_2\}\left(I_1 S_{\mathrm{h}2} + I_2 S_{\mathrm{h}1}\right) + \text{c.p.}\right].
\end{aligned} \tag{2.72}$$

The matrix representation of the spin operators can be derived from the creation and annihilation operator

$$J_+ = J_1 + \mathrm{i}J_2, \qquad J_- = J_1 - \mathrm{i}J_2 \tag{2.73}$$

with

$$J_+ |j, m\rangle = \sqrt{(j-m)(j+m+1)}\,|j, m+1\rangle\,, \tag{2.74}$$

$$J_- |j, m\rangle = \sqrt{(j+m)(j-m+1)}\,|j, m-1\rangle\,, \tag{2.75}$$

$$J_3 |j, m\rangle = m\,|j, m\rangle \tag{2.76}$$

where J is a spin operator and j, m are the spin quantum numbers of one spin. The spin matrices turn out to be

$$I_1 = \frac{1}{\sqrt{2}}\begin{pmatrix} 0&0&1&0&0&0\\ 0&0&0&1&0&0\\ 1&0&0&0&1&0\\ 0&1&0&0&0&1\\ 0&0&1&0&0&0\\ 0&0&0&1&0&0 \end{pmatrix}, \qquad S_{\mathrm{h}1} = \frac{1}{2}\begin{pmatrix} 0&1&0&0&0&0\\ 1&0&0&0&0&0\\ 0&0&0&1&0&0\\ 0&0&1&0&0&0\\ 0&0&0&0&0&1\\ 0&0&0&0&1&0 \end{pmatrix},$$

$$I_2 = \frac{\mathrm{i}}{\sqrt{2}}\begin{pmatrix} 0&0&-1&0&0&0\\ 0&0&0&-1&0&0\\ 1&0&0&0&-1&0\\ 0&1&0&0&0&-1\\ 0&0&1&0&0&0\\ 0&0&0&1&0&0 \end{pmatrix}, \quad S_{\mathrm{h}2} = \frac{\mathrm{i}}{2}\begin{pmatrix} 0&-1&0&0&0&0\\ 1&0&0&0&0&0\\ 0&0&0&-1&0&0\\ 0&0&1&0&0&0\\ 0&0&0&0&0&-1\\ 0&0&0&0&1&0 \end{pmatrix}, \tag{2.77}$$

$$I_3 = \begin{pmatrix} 1 & 0 & 0 & 0 & 0 & 0 \\ 0 & 1 & 0 & 0 & 0 & 0 \\ 0 & 0 & 0 & 0 & 0 & 0 \\ 0 & 0 & 0 & 0 & 0 & 0 \\ 0 & 0 & 0 & 0 & -1 & 0 \\ 0 & 0 & 0 & 0 & 0 & -1 \end{pmatrix}, \qquad S_{\mathrm{h}3} = \frac{1}{2} \begin{pmatrix} 1 & 0 & 0 & 0 & 0 & 0 \\ 0 & -1 & 0 & 0 & 0 & 0 \\ 0 & 0 & 1 & 0 & 0 & 0 \\ 0 & 0 & 0 & -1 & 0 & 0 \\ 0 & 0 & 0 & 0 & 1 & 0 \\ 0 & 0 & 0 & 0 & 0 & -1 \end{pmatrix}.$$

Solving this by diagionalyzing the spin Hamiltonian generates six eigenvalues $W_n(\boldsymbol{p})$ occurring in pairs of two degenerate eigenvalues (Kramer's theorem [24]). Writing the components of the Schrödinger equation we get

$$\begin{aligned} E_n \Phi X = X \left[\frac{\boldsymbol{p}^2}{2} - \frac{1}{r} \right] \Phi \\ + \Phi \tilde{H}_{\mathrm{b}}(\boldsymbol{p}, \boldsymbol{I}, \boldsymbol{S}_{\mathrm{h}}) X \\ - \frac{1}{r}(\Phi X) + X \frac{1}{r} \Phi. \end{aligned} \tag{2.78}$$

The last line occurs because $X(\boldsymbol{p}; \boldsymbol{I}, \boldsymbol{S}_{\mathrm{h}})$ depends on the momentum which makes the position operator acting on it. Due to the spin motion being much faster we treat this term as a small perturbation and neglect it.

Finally we are able to reduce the Hamiltonian to

$$H\Phi = \left[\frac{\boldsymbol{p}^2}{2} - \frac{1}{r} + W_n(\boldsymbol{p}) \right] \Phi = E_n \Phi \tag{2.79}$$

which does not depend on the spins any more. In this thesis we are interested in the yellow exciton series which belongs to a total spin of 1/2. When solving the eigenvalue problem for $W_n(\boldsymbol{p})$ we take all spins into account, also the green series with a spin of 3/2. Therefore, the lowest pair of degenerate eigenvalues $W_n(\boldsymbol{p})$ is taken for the yellow series because we expect the spins to stay on their energy surface.

Now we can make the Hamiltonian (2.79) classical:

$$H = \frac{\boldsymbol{p}^2}{2} - \frac{1}{r} + W_n(\boldsymbol{p}) = E. \tag{2.80}$$

In classical dynamics we are no longer searching for energy eigenvalues but in simulating trajectories at fixed energy E.

2.3.2 Classical exciton dynamics

Now that the spins are no longer a part of the classical Hamiltonian we want to simulate classical exciton orbits. From the semiclassical theories we know that we need to find

periodic orbits because only they contribute to the trace formulas. In this thesis we want to make a first approach of using semiclassical theories for excitons in cuprous oxide which is why we simplify the system further.

From the cubic O_h symmetry of Cu_2O we know that there are rotation axes. On these axes one-dimensional orbits occur but since they propagate straightly to the core they have zero angular momentum and are therefore not of interest in the fluctuating part of the spectrum. This works analogously for the nine symmetry planes ($3\sigma_\mathrm{h}$ and $6\sigma_\mathrm{d}$) at which the system can be mirrored. Orbits which are set up in these planes should stay there and are therefore two-dimensional. In this thesis we choose to search for orbits only in the symmetry plane orthogonal to [001].

Before we can start with investigating the classical exciton dynamics a regularization is introduce because of the Coulomb singularity in the Hamiltonian at $\boldsymbol{r} = 0$. This can reduce the accuracy for orbits which come close to this region. In this thesis Kustaanheimo-Stiefel (KS) coordinates [9, 25] are used which are generated not only by a transformation of space but also of time. One specialty of the KS coordinates is that they can be applied only for a even number of space coordinates which makes it necessary to append a zero to our position and momentum in order to get a four-dimensional space

$$\boldsymbol{r} = (r_1, r_2, r_3, 0)^\mathsf{T}, \tag{2.81}$$

$$\boldsymbol{p} = (p_1, p_2, p_3, 0)^\mathsf{T}. \tag{2.82}$$

The KS transformations are defined by

$$\boldsymbol{L}(\boldsymbol{U}) = \frac{1}{2}\begin{pmatrix} U_3 & -U_4 & U_1 & -U_2 \\ U_4 & U_3 & U_2 & U_1 \\ U_1 & U_2 & -U_3 & -U_4 \\ U_2 & -U_1 & -U_4 & U_3 \end{pmatrix}, \tag{2.83}$$

$$\boldsymbol{r} = \boldsymbol{L}(\boldsymbol{U})\boldsymbol{U} = \frac{1}{2}\begin{pmatrix} 2(U_1U_3 - U_2U_4) \\ 2(U_1U_4 + U_2U_3) \\ U_1^2 + U_2^2 - U_3^2 - U_4^2 \\ 0 \end{pmatrix}, \tag{2.84}$$

$$\boldsymbol{p} = \frac{2}{U^2}\boldsymbol{L}(\boldsymbol{U})\boldsymbol{P} = \frac{1}{U^2}\begin{pmatrix} U_3P_1 - U_4P_2 + U_1P_3 - U_2P_4 \\ U_4P_1 + U_3P_2 + U_2P_3 + U_1P_4 \\ U_1P_1 + U_2P_2 - U_3P_3 - U_4P_4 \\ U_2P_1 - U_1P_2 - U_4P_3 + U_3P_4 \end{pmatrix} \tag{2.85}$$

with the new four-dimensional position $\boldsymbol{U}$ and momentum $\boldsymbol{P}$. The Hamiltonian

$$H = \frac{p^2}{2} - \frac{1}{r} + \tilde{H}_\mathrm{b} = \frac{P^2}{2U^2} - \frac{2}{U^2} + \tilde{H}_\mathrm{b} \tag{2.86}$$

can be transformed with a Poincaré transformation [9, 26]

$$\tilde{H} = g(\boldsymbol{U}, \boldsymbol{P})(H - E) \tag{2.87}$$

where E is the energy. The singularity at $U = 0$ can now be eliminated by choosing

$$g(\boldsymbol{U}, \boldsymbol{P}) = U^2 \tag{2.88}$$

what leads to the new Hamiltonian

$$\tilde{H} = \frac{P^2}{2} - 2 + \tilde{H}_{\mathrm{b}}^{\mathrm{reg}}(\boldsymbol{U}, \boldsymbol{P}) - 2EU^2 \tag{2.89}$$

where $\tilde{H}_{\mathrm{b}}^{\mathrm{reg}} = U^2 \tilde{H}_{\mathrm{b}}$. The time t transforms to the the KS time τ with

$$\frac{\mathrm{d}t}{\mathrm{d}\tau} = g(\boldsymbol{U}, \boldsymbol{P}) = U^2 = 2r. \tag{2.90}$$

The KS transformation is a cotangent lift transformation which means that the new coordinates $\boldsymbol{\Gamma} = (\boldsymbol{U}, \boldsymbol{P})^{\intercal}$ are still canonically conjugated. Hamilton's equation of motion reads

$$\frac{\mathrm{d}\boldsymbol{\Gamma}}{\mathrm{d}\tau} = \boldsymbol{J}\frac{\partial H}{\partial \boldsymbol{\Gamma}} \tag{2.91}$$

with

$$\boldsymbol{J} = \begin{pmatrix} 0 & \mathbb{1} \\ -\mathbb{1} & 0 \end{pmatrix}. \tag{2.92}$$

This is the equation we have to integrate when simulating the exciton orbits.

2.3.3 Periodic orbit search

In the following it will be shown how the classical exciton dynamics can be simulated and how to search for periodic orbits in the symmetry plane orthogonal to [001].

At the beginning of the simulation a start position $\boldsymbol{r}_0$ is given in form of a start radius r_0 and a start angle φ_0. The z component is thereby zero because we want to stay in the symmetry plane. In this thesis we restrict ourselves to such orbits which have points where the velocity is orthogonal to the position. This reduces the search to finding the start position $\boldsymbol{r}_0$ because the absolute of the velocity $\boldsymbol{v}_0$ is given by the choice of a fixed energy. Because of the $C_{4\mathrm{v}}$ symmetry of the symmetry plane it is likely that at least two of the points with orthogonal velocity are located either at $\varphi = 0°$ or $\varphi = 45°$. This is why only these two angles are used when searching for starting conditions of periodic

orbits which reduces the effort to a one-dimensional root search in the absolute $|\boldsymbol{r}_0|$. Note that because of the $C_{4\mathrm{v}}$ symmetry it would be sufficient to look for further angles between 0° and 45°.

The starting conditions are transformed into KS coordinates with

$$\boldsymbol{U}_0 = \begin{pmatrix} \sqrt{2r_0}\cos\left(\frac{\theta_0}{2}\right)\cos\left(\frac{\varphi_0+\alpha_0}{2}\right) \\ \sqrt{2r_0}\cos\left(\frac{\theta_0}{2}\right)\sin\left(\frac{\varphi_0+\alpha_0}{2}\right) \\ \sqrt{2r_0}\sin\left(\frac{\theta_0}{2}\right)\cos\left(\frac{\varphi_0-\alpha_0}{2}\right) \\ \sqrt{2r_0}\sin\left(\frac{\theta_0}{2}\right)\sin\left(\frac{\varphi_0-\alpha_0}{2}\right) \end{pmatrix}. \tag{2.93}$$

The angle θ_0 is 90° because the simulation takes place in the xy-plane. The parameter α_0 can be chosen arbitrarily because the new coordinates have an additional dimension. It is set to zero and remains constant during the simulation.

The start momentum cannot be calculated so easily because it is derived from the conservation of energy. In contrast to the hydrogen like case the Hamiltonian (2.89) depends on $W_n(\boldsymbol{U}, \boldsymbol{P})$ which depends also on the momentum itself. In order to solve that problem a four-dimensional root search $\boldsymbol{f}(\boldsymbol{P}) = (f_1, f_2, f_3, f_4)^\intercal = \boldsymbol{0}$ is done where the four equations

$$f_1(\boldsymbol{P}) = \frac{\boldsymbol{P}^2}{2} - E\boldsymbol{U}^2 + W_n(\boldsymbol{U}, \boldsymbol{P}) - 2, \tag{2.94}$$

$$f_2(\boldsymbol{P}) = \boldsymbol{U}\dot{\boldsymbol{U}} = \boldsymbol{U}\frac{\partial \tilde{H}}{\partial \boldsymbol{P}}, \tag{2.95}$$

$$f_3(\boldsymbol{P}) = U_1\dot{U}_1 + U_2\dot{U}_2 - U_3\dot{U}_3 - U_4\dot{U}_4, \tag{2.96}$$

$$f_4(\boldsymbol{P}) = U_2\dot{U}_1 - U_1\dot{U}_2 - U_4\dot{U}_3 + U_2\dot{U}_4 \tag{2.97}$$

must be zero. Thereby $\dot{\boldsymbol{U}}$ is the derivative of the position with respect to τ which equals $\partial H/\partial \boldsymbol{P}$. The first equation (2.94) is the conservation of energy, the second one (2.95) refers to the initial velocity being orthogonal to the position vector ($\hat{e}_r$) and the third equation (2.96) equals $v_z = 0$ which can be seen in line three of transformation (2.85). From the same transformation one can derive the bilinear relation

$$U_2P_1 - U_1P_2 - U_4P_3 + U_3P_4 = 0 \tag{2.98}$$

since the fourth component has to be zero. For solving the equation system it is necessary to calculate

$$\frac{\partial \tilde{H}}{\partial \boldsymbol{P}} = \boldsymbol{P} + \frac{\partial W_n}{\partial \boldsymbol{P}} \tag{2.99}$$

with the derivative of $\partial W_n/\partial \boldsymbol{P}$ which cannot be done analytically. It is therefore calculated numerically with a five-point formula

$$\frac{\partial W_n(\boldsymbol{P})}{\partial P_i} = \frac{-W_n(\boldsymbol{P}+2\mathrm{d}P\hat{e}_i) + 8W_n(\boldsymbol{P}+\mathrm{d}P\hat{e}_i) - 8W_n(\boldsymbol{P}-\mathrm{d}P\hat{e}_i) + W_n(\boldsymbol{P}-2\mathrm{d}P\hat{e}_i)}{12\mathrm{d}P} \tag{2.100}$$

where $\hat{\boldsymbol{e}}_i = (\delta_{i1}, \delta_{i2}, \delta_{i3}, \delta_{i4})^\intercal$ and $\mathrm{d}P$ being a fixed parameter which was optimized for stable results. This can be done analogously for $\boldsymbol{U}$ but with another parameter $\mathrm{d}U$.

In order to succeed in this root search one needs a good initial guess for $\boldsymbol{P}$. This is done by first assuming the perturbation W_n to be zero. In that case it would just be the hydrogen like case with an absolute of

$$P_0^{(0)} = \sqrt{2EU^2 + 4} \tag{2.101}$$

and in the direction of $\hat{e}_\varphi$. This guess can be improved by inserting the resulting momentum into $W_n(\boldsymbol{P}_0)$ and calculating the momentum again. The root search is done using the algorithm *HYBRD1* [27].

After setting up the particle it is integrated for some time. Now we check whether it returns to the start position or not. In order to search for specific orbits the number of cycles around the core n_{cycle} is fixed which means that the position angle φ changes by $2\pi n_{\mathrm{cycle}}$ during the simulation. In order to decide whether an orbit is periodic or not it is checked whether the radial velocity

$$\frac{\mathrm{d}r}{\mathrm{d}t} = \frac{\mathrm{d}\tau}{\mathrm{d}t}\frac{\mathrm{d}(U^2/2)}{\mathrm{d}\tau} = \frac{1}{U^2}\boldsymbol{U}\frac{\mathrm{d}\boldsymbol{U}}{\mathrm{d}\tau} \tag{2.102}$$

is zero. The actual search algorithm is a root search in $\boldsymbol{U}\dot{\boldsymbol{U}}(r_0) = 0$ using *HYBRD1* [27] again. The starting radius r_0 is thereby varied and a new orbit is simulated for every searching step. Note that the resulting orbit is not necessarily periodic with n_{cycle} but can also be periodic with $2n_{\mathrm{cycle}}$ in case the position does not return to the starting position. This happens because of the mirror symmetry of the Hamiltonian.

2.3.4 Periodic orbit parameters

For the semiclassical calculations we need to know about the action, period and the monodromy matrix of each periodic orbit. We also need the second derivative of $g_E(J_1) = J_2$ in the Berry-Tabor formula (2.44).

The classical action is

$$S = \oint \boldsymbol{p}\,\mathrm{d}\boldsymbol{r} = \oint \boldsymbol{P}\,\mathrm{d}\boldsymbol{U} = \oint \boldsymbol{P}\frac{\mathrm{d}U}{\mathrm{d}\tau}\,\mathrm{d}\tau. \tag{2.103}$$

It follows that the derivative of the action is

$$\frac{\mathrm{d}S}{\mathrm{d}\tau} = \boldsymbol{P}\dot{\boldsymbol{U}}. \tag{2.104}$$

By using this equation it is possible to integrate the action during the integration of the system with Hamilton's equation of motion (2.91). The time has to be integrated too since the KS transformation uses a nonlinear time transformation. From equation (2.90) one gets

$$\frac{\mathrm{d}t}{\mathrm{d}\tau} = U^2. \tag{2.105}$$

The monodromy matrix is a submatrix of the stability matrix which is why the stability matrix must be calculated. The stability of an orbit describes what happens when a small deviation $\Delta\boldsymbol{\Gamma}(0)$ is applied to the start coordinates $\boldsymbol{\Gamma}(t=0)$. The stability matrix $\boldsymbol{M}(0,t)$ [17] is the linearized response and connects this deviation $\Delta\boldsymbol{\Gamma}(0)$ to the deviation $\Delta\boldsymbol{\Gamma}(t)$ at time t by

$$\Delta\boldsymbol{\Gamma}(t) = \boldsymbol{M}(0,t)\Delta\boldsymbol{\Gamma}(0). \tag{2.106}$$

The time evolution of the stability matrix can be derived from Hamilton's equation of motion (2.91) like

$$\begin{aligned}
\frac{\mathrm{d}\boldsymbol{M}_{ij}}{\mathrm{d}\tau} &= \frac{\mathrm{d}}{\mathrm{d}\tau}\frac{\partial\Gamma_i(\tau)}{\partial\Gamma_j(0)} \\
&= \frac{\partial}{\partial\Gamma_j(0)}\frac{\mathrm{d}\Gamma_i(\tau)}{\mathrm{d}\tau} \\
&= \frac{\partial\Gamma_l(\tau)}{\partial\Gamma_j(0)}\frac{\partial}{\partial\Gamma_l(\tau)}J_{ik}\frac{\partial H}{\partial\Gamma_k(\tau)} \\
&= J_{ik}\frac{\partial^2 H}{\partial\Gamma_k(\tau)\partial\Gamma_l(\tau)}M_{lj}(0,\tau).
\end{aligned} \tag{2.107}$$

This equation depends on the second derivative of the Hamiltonian in each direction

$$\frac{\partial^2\tilde{H}}{\partial\Gamma_i\partial\Gamma_j} = \begin{pmatrix} -4E\delta_{kl} & 0 \\ 0 & \delta_{kl} \end{pmatrix}_{ij} + \frac{\partial^2 W_n}{\partial\Gamma_i\partial\Gamma_j}, \qquad k,l \in [1,2,3,4]. \tag{2.108}$$

In order to calculate this numerically the five-point formula (2.100) is used two times like

$$\frac{\partial^2 W_n}{\partial \Gamma_i \partial \Gamma_j} = \frac{\sum_{\kappa=-1,1} -\kappa \partial_j W_n(\mathbf{\Gamma} + \kappa 2 \mathrm{d}\Gamma_i \hat{e}_i) + \kappa 8 \partial_j W_n(\mathbf{\Gamma} + \kappa \mathrm{d}\Gamma_i \hat{e}_i)}{12 \mathrm{d}\Gamma_i} \tag{2.109}$$

where $\partial_j W_n = \partial W_n / \partial \Gamma_j$ can be calculated using the original formula. The parameter $\mathrm{d}\Gamma_i$ is thereby chosen differently depending on whether Γ_i is a position or momentum variable.

Originally a three-point formula was used but it turned out that it has not the necessary accuracy and that this in fact slowed down the integration algorithm *RKSUITE* [28] which uses adaptive step size control. Therefore, the more precise five-point formula is also faster than the three-point formula regardless the factor four in the number calculations of W_n.

The function $g_E(J_1) = J_2$ was defined via equation (2.45) and defines the relation of the action variables on the energy surface. In contrast to the other parameters the action variables J_i cannot be easily integrated with the system. Nevertheless, it is possible to calculate them numerically by calculating them from the classical action

$$S_{\boldsymbol{M}} = 2\pi M_1 J_1 + 2\pi M_2 J_2 \tag{2.110}$$

where we have the winding numbers $\boldsymbol{M} = (M_1, M_2)$ again. Simulating a series of periodic orbits with varying M_1 but constant M_2 allows for calculating the derivative

$$J_1 = \frac{1}{2\pi} \frac{\partial S_{\boldsymbol{M}}}{\partial M_1} \tag{2.111}$$

numerically. Using equation (2.110) one can calculate J_2 as

$$J_2 = \frac{S_{\boldsymbol{M}}}{2\pi M_2} - \frac{M_1}{M_2} J_1. \tag{2.112}$$

Note that this works of course only for constant energy. Now that J_1 and J_2 are known also g_E is known. The second derivative has to be calculated numerically too.

In this thesis we use a polynomial fit to the action in order to derive J_1 and J_2 through the analytical derivative of this polynomial. The resulting curve $J_2(J_1)$ is smooth and can be evaluated at a high number of equally spaced points. These points are used for applying a numerical two-point derivative twice. The resulting points $g''_E(J_1)$ can be interpolated with fits again.

The second derivative of the function g_E can also be calculated using the stability matrix [29, 30]. The corresponding formula is

$$g_E'' = \frac{2}{\pi M_2^3 \Delta S} \left[\frac{1}{\sqrt{\det(\boldsymbol{M}_{\mathrm{s},xy} - \mathbb{1})}} + \frac{1}{\sqrt{-\det(\boldsymbol{M}_{\mathrm{u},xy} - \mathbb{1})}} \right]^{-2} \tag{2.113}$$

with

$$\Delta S = \frac{1}{2}(S_{\mathrm{u}} - S_{\mathrm{s}}). \tag{2.114}$$

Thereby the index s labels the quantities of the stable and u the quantities of the unstable partner orbit. Note that this formula holds only for M_2, S and $\boldsymbol{M}$ being parameters of the primitive periodic orbit.

Now that we have seen how the parameters can be calculated let us explain the stability matrix in more detail.

Properties of the stability matrix

The stability matrix is symplectic what is defined as

$$\boldsymbol{M}^{\intercal} \boldsymbol{J} \boldsymbol{M} = \boldsymbol{J}. \tag{2.115}$$

It follows that the eigenvalues λ occur in quadruplets of

$$\lambda_i, \lambda_i^*, \frac{1}{\lambda_i}, \frac{1}{\lambda_i^*}. \tag{2.116}$$

For the case of real eigenvalues or complex eigenvalues with an absolute of one this reduces to pairs of $\lambda_i, \lambda_i^{-1}$ since $|\lambda_i| = 1 \Rightarrow \lambda_i^* = \lambda_i^{-1}$.

The stability matrix for a periodic orbit with period T is

$$\begin{aligned} \boldsymbol{M}(0, nT) &= \boldsymbol{M}(T, nT)\boldsymbol{M}(0, T) \\ &= (\boldsymbol{M}(0, T))^n \end{aligned} \tag{2.117}$$

after n periods. In this thesis we will only investigate the stability of periodic orbits which is why the stability matrix $\boldsymbol{M}$ without given arguments is defined as the stability matrix after one period $\boldsymbol{M}(0, T)$. It follows that the deviation after n periods is

$$\Delta\boldsymbol{\gamma}_i(nT) = \lambda_i^n \Delta\boldsymbol{\gamma}_i(0) \tag{2.118}$$

where $\Delta\boldsymbol{\gamma}_i$ is an eigenvector belonging to λ_i.

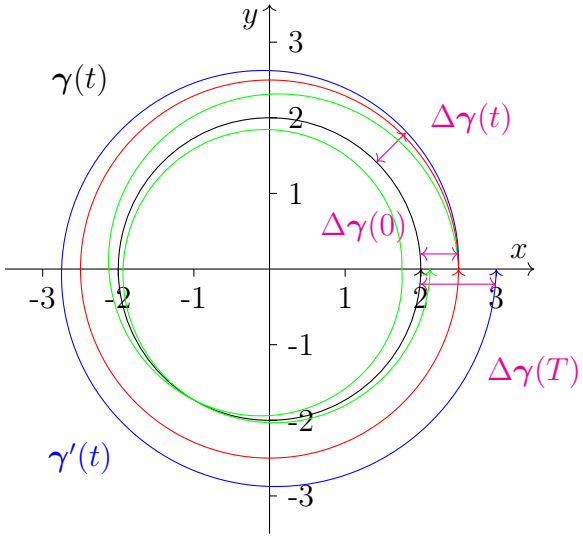

Figure 2.3: The black circle is the original periodic orbit starting at $\boldsymbol{r} = (2, 0)$. The figure shows what happens when applying a deviation $\Delta\boldsymbol{\gamma}(0)$ to the x position. The red orbit is the case for a stability eigenvalue of $\lambda_x = 1$ where the new orbit is periodic again. In case of the blue orbit it would be $\lambda_x = 2$. Since the response is linear for small deviations the distance to the original orbit will increase over time. The green curve has an eigenvalue of $\lambda_x = -1/2$. After time T the orbit is at $(1.75, 0)$ and at $(2.125, 0)$ after $2T$. The original orbit will be approximated after some time.

Eigenvalues and eigenvectors

The stability matrix can be connected to the Liapunov exponent

$$\begin{aligned} L &= \lim_{t\to\infty} \frac{1}{t} \ln(\sup|\lambda_i(t)|) \\ &= \lim_{n\to\infty} \frac{1}{nT} \ln(\sup|\lambda_i(T)|^n) \\ &= \frac{1}{T} \ln(\sup|\lambda_i(T)|) \end{aligned} \tag{2.119}$$

where $\sup|\lambda_i(t)|$ is the maximum eigenvalue of $\boldsymbol{M}(0, t)$. The orbit is stable if $L = 0$ which is the case for $\sup|\lambda_i(t)| = 1$ and unstable for $L > 0$ ($\sup|\lambda_i(t)| > 1$). The case $\sup|\lambda_i(t)| < 1$ and $L < 0$ can therefore not occur because of the symplectic structure of the stability matrix.

Figure 2.3 explains how the eigenvalues affect the behavior of a periodic orbit. For an eigenvalue of $\lambda_i = 1$ the orbit is stable because the deviation will be the same after an arbitrary number of periods. For $|\lambda_i| > 1$ the deviation becomes larger with increasing time and the orbit therefore unstable. For $|\lambda_i| < 1$ the deviation becomes smaller and the new orbit tends to the original orbit for $t \to \infty$. This looks like the orbit is even more stable but the symplectic structure of the stability matrix states that there must be a direction in which $|\lambda_j| = \left|\lambda_i^{-1}\right| > 1$ which is why the orbit is unstable regardless. As one can see in the figure a negative eigenvalue will cause to the deviation to change sign after each period.

This was quite intuitive but as told before the eigenvalues and also the eigenvectors can be complex. In the following it will be explained how a complex eigenvalue affects the orbit.

The eigenvalues can be expressed through the complex exponent ϕ with

$$\lambda_{i,i+1} = \exp\{\pm\phi_i\} = \exp\{\pm(u_i + \mathrm{i}v_i)\} \tag{2.120}$$

where u_i and v_i are real. For the case of complex eigenvalues with $u = 0$ the eigenvectors have the form

$$\boldsymbol{\Lambda}_{i,i+1} = \boldsymbol{R}_i \pm \mathrm{i}\boldsymbol{I}_i. \tag{2.121}$$

The stability matrix acts on the vectors $\boldsymbol{R}_i$ like

$$\begin{aligned}\boldsymbol{M}\boldsymbol{R}_i &= \boldsymbol{M}\left[\frac{1}{2}\left(\boldsymbol{R}_i + \mathrm{i}\boldsymbol{I}_i\right) + \frac{1}{2}\left(\boldsymbol{R}_i - \mathrm{i}\boldsymbol{I}_i\right)\right] \\ &= \exp(\mathrm{i}v_i)\frac{1}{2}\left(\boldsymbol{R}_i + \mathrm{i}\boldsymbol{I}_i\right) + \exp(-\mathrm{i}v_i)\frac{1}{2}\left(\boldsymbol{R}_i - \mathrm{i}\boldsymbol{I}_i\right) \\ &= \cos(v_i)\boldsymbol{R}_i - \sin(v_i)\boldsymbol{I}_i \end{aligned} \tag{2.122}$$

and analogously on $\boldsymbol{I}_i$ like

$$\boldsymbol{M}\boldsymbol{I}_i = \cos(v_i)\boldsymbol{I}_i + \sin(v_i)\boldsymbol{R}_i. \tag{2.123}$$

Together it is possible to let the stability matrix act on a real linear combination of $\boldsymbol{R}_i$ and $\boldsymbol{I}_i$. This results in

$$\boldsymbol{M}\left[a\cos(\theta)\boldsymbol{R}_i + a\sin(\theta)\boldsymbol{I}_i\right] = a\cos(\theta - v_i)\boldsymbol{R}_i + a\sin(\theta - v_i)\boldsymbol{I}_i \tag{2.124}$$

with real numbers a and θ. As one can see the stability matrix causes a rotation in the $\boldsymbol{R}_i$-$\boldsymbol{I}_i$-plane where it is important to mention that $\boldsymbol{R}_i$ and $\boldsymbol{I}_i$ are not necessarily unit vectors.

Furthermore, there is another way to investigate the stability of the periodic orbit by taking a look at the sum

$$b_i \equiv \lambda_i + \lambda_i^{-1} = \exp(\phi_i) + \exp\{-\phi_i\} = 2\cosh(\phi_i). \tag{2.125}$$

The orbit is stable in the corresponding direction if $|b_i| \leq 2$ and else unstable. This value will also be important for interpolating the stability of further periodic exciton orbits from already simulated ones.

Monodromy matrix

The actual number of degrees of freedom is reduced by one for each conserved quantity like energy or angular momentum. The eigenvalues corresponding to the direction of those quantities are one. The monodromy matrix is the nontrivial submatrix of the stability matrix which means that it only contains the eigenvalues corresponding to the other directions. Note that the remaining eigenvalues can be one regardless.

2.4 Customization and scaling of the energy spectra

In order to account for the specialties of excitons in cuprous oxide we adapt the semiclassical trace formulas for our purpose. Since the energy spectrum is shrunk in the limit of high energies [1] we want to stretch it in order to get an oscillating function with about fixed period in order to be able to investigate it's frequencies and compare them to the semiclassical calculations. This is what this section deals with and additionally the Fourier transform of a quantum mechanical spectrum will be shown.

2.4.1 Trace formula for two-dimensional orbits in the three-dimensional system

The problem with the Berry-Tabor formula (2.44) is that it is only valid for two-dimensional systems but excitons in Cu_2O are three-dimensional. Gutzwiller's trace formula (2.67) on the other hand is applicable for an arbitrary number of dimensions but only for periodic orbits which are isolated. As can be seen for example in the Poincaré surface of section in figure 3.1 there will be one central fixed point for which these conditions apply and for which Gutzwiller's trace formula will be used. The other orbits occur in pairs of a stable and an unstable partner orbit and are not isolated.

The monodromy matrix $\boldsymbol{M}_{\mathrm{PO}}$ of these orbits contains two stability eigenvalues for the stability inside the symmetry plane (λ_{xy}, λ_{xy}^{-1}) and two for the stability out of it (λ_z, λ_z^{-1}). Since the orbits are (almost) stable against perturbations out of the plane we treat them as isolated in this direction and calculate the part which depends on λ_z with Gutzwiller. The stability in the plane will be treated with Berry-Tabor.

The determinant in Gutzwiller's trace formula (2.67) can be split up like

$$\rho(E) = \frac{1}{\pi} \sum_{\mathrm{PO}} \frac{1}{\sqrt{|\det(\boldsymbol{M}_z - \mathbb{1})|}} \frac{T_{\mathrm{PPO}}}{\sqrt{|\det(\boldsymbol{M}_{xy} - \mathbb{1})|}} \cos\Big(S_{\mathrm{PO}} - \frac{\pi}{2}\sigma_{\mathrm{PO}}\Big) \tag{2.126}$$

with

$$\sqrt{|\det(\boldsymbol{M}_i - \mathbb{1})|} = \sqrt{\left|(\lambda_i - 1)(\lambda_i^{-1} - 1)\right|} = \left|\lambda_i^{1/2} - \lambda_i^{-1/2}\right|. \tag{2.127}$$

The idea is to keep only the term $\sqrt{|\det(\boldsymbol{M}_z - \mathbb{1})|}$ and replace the remaining part with Berry-Tabor (2.44). It results in the mixed trace formula

$$\rho(E) = \frac{1}{\pi} \sum_{\boldsymbol{M}} \frac{1}{\sqrt{|\det(\boldsymbol{M}_z - \mathbb{1})|}} \frac{T_{\boldsymbol{M}}}{\sqrt{M_2^3 |g_E''|}} \cos\Big(S_{\boldsymbol{M}} - \frac{\pi}{2}\sigma_{\boldsymbol{M}} - \frac{\pi}{4}\Big). \tag{2.128}$$

2.4.2 Scaling of the energy spectrum

As mentioned above we want to stretch the energy spectrum in order to get rid of it's shrinking. Therefore, remember that the energy is expressed through

$$E = -\frac{1}{2n_{\text{eff}}^2} \tag{2.129}$$

with an effective quantum number $n_{\text{eff}} = n - \delta_{n,l}$. Although this quantum number n_{eff} is connected to quantum defects $\delta_{n,l}$ it scales about with the principle quantum number n. The states are therefore approximately equidistant in n_{eff} which is why we want to get the density $\rho(n_{\text{eff}})$ instead of $\rho(E)$. From

$$\frac{\mathrm{d}E}{\mathrm{d}n_{\text{eff}}} = \frac{1}{n_{\text{eff}}^3} \tag{2.130}$$

and

$$\int \rho(n_{\text{eff}}) \mathrm{d}n_{\text{eff}} \stackrel{!}{=} \int \rho(E) \mathrm{d}E = \int \frac{\rho(E)}{n_{\text{eff}}^3} \mathrm{d}n_{\text{eff}} \tag{2.131}$$

it follows for Gutzwiller's trace formula (2.67) that

$$\rho(n_{\text{eff}}) = \frac{\rho(E)}{n_{\text{eff}}^3} = \frac{1}{\pi n_{\text{eff}}^3} \sum_{\text{PO}} \frac{T_{\text{PPO}}}{\sqrt{|\det(\boldsymbol{M} - \mathbb{1})|}} \cos\Big(S_{\text{PO}} - \frac{\pi}{2}\sigma_{\text{PO}}\Big) \tag{2.132}$$

and analogously for the mixed trace formula (2.128). Since the action S scales about with n_{eff} (see figure 3.13) we can easily see in the oscillating cosine that S/n_{eff} is the variable which corresponds to the frequencies in a Fourier transformed spectrum. The corresponding amplitudes $\mathcal{A}(S/n_{\text{eff}})$ are given through the prefactor of the cosine. Originally the amplitude is complex because of the oscillating term with the Maslov index σ but we can also use the absolute of the amplitude $|\mathcal{A}|$. In the hydrogen-like case peaks would occur at multiples of 2π which is why we plot the amplitudes over $S/(2\pi n_{\text{eff}})$ in order to make the deviations from the hydrogen atom evident.

2.4.3 Comparison to the quantum mechanical spectrum

One problem when comparing the quantum mechanical and semiclassical frequencies is that we calculate them from a number of periodic orbits at fixed n_{eff} in the semiclassical case while they result from a scaled energy spectrum in the quantum mechanical case. In the following we will outline how P. Rommel and M. Schumacher [32] keep the energy virtually fixed in the quantum mechanical calculations.

At first we abbreviate the Hamiltonian (2.8) with

$$H = \boldsymbol{p}\boldsymbol{\mathcal{L}}\boldsymbol{p} - \frac{1}{r} + H_{\text{SO}} \tag{2.133}$$

with a linear operator $\boldsymbol{\mathcal{L}}$ depending on quasispin and hole spin which describes all terms in which $\boldsymbol{p}$ occurs. As one can see in equation (2.9) these terms are all of order $\boldsymbol{p}^2$. The H_{SO} term denotes the spin-orbit coupling (2.3). The Schrödinger equation then reeds

$$H\Psi = E\Psi = -\frac{1}{2n_{\text{eff}}^2}\Psi. \tag{2.134}$$

We try to eliminate the energy dependence by multiplying with n_{eff}^2 and scaling the coordinates. When scaling the position with $\boldsymbol{r} = n_{\text{eff}}^2\tilde{\boldsymbol{r}}$ the quantum mechanical momentum has to scale with $\boldsymbol{p} = n_{\text{eff}}^{-2}\tilde{\boldsymbol{p}}$ because of the canonical commutation relation. The new Schrödinger equation becomes

$$\tilde{H}\Psi = n_{\text{eff}}^2 H\Psi = \left(\frac{\tilde{\boldsymbol{p}}\boldsymbol{\mathcal{L}}\tilde{\boldsymbol{p}}}{n_{\text{eff}}^2} - \frac{1}{\tilde{r}} + n_{\text{eff}}^2 H_{\text{SO}}\right)\Psi = -\frac{1}{2}\Psi. \tag{2.135}$$

In order to evolve this near a fixed energy $n_{\text{eff}}^2 H_{\text{SO}}$ is set to $n_0^2 H_{\text{SO}}$ as

$$\tilde{H} = \left(\frac{\tilde{\boldsymbol{p}}\boldsymbol{\mathcal{L}}\tilde{\boldsymbol{p}}}{n_{\text{eff}}^2} - \frac{1}{\tilde{r}} + n_0^2 H_{\text{SO}}\right)\Psi = -\frac{1}{2}\Psi \tag{2.136}$$

where the spin-orbit coupling can now be adjusted in quantum mechanical calculations by choosing n_0. This results in quantized states n_{eff} which depend on the choice of n_0.

In our classical systems we are not limited through canonical commutation relation and are free to choose $\boldsymbol{p} = n_{\text{eff}}^{-1}\tilde{\boldsymbol{p}}$ instead. Our transformed classical Hamiltonian then reads

$$\tilde{H} = \tilde{\boldsymbol{p}}\boldsymbol{\mathcal{L}}\tilde{\boldsymbol{p}} - \frac{1}{\tilde{r}} + n_{\text{eff}}^2 H_{\text{SO}} \tag{2.137}$$

with $\tilde{H} = n_{\text{eff}}^2 E = -1/2$.

To cut a long story short, classical calculations with fixed n_{eff} can be compared to quantum mechanical calculations with fixed $n_0 = n_{\text{eff}}$. Varying n_0 will change the quantum mechanical spectrum while varying n_{eff} changes the classical dynamics.

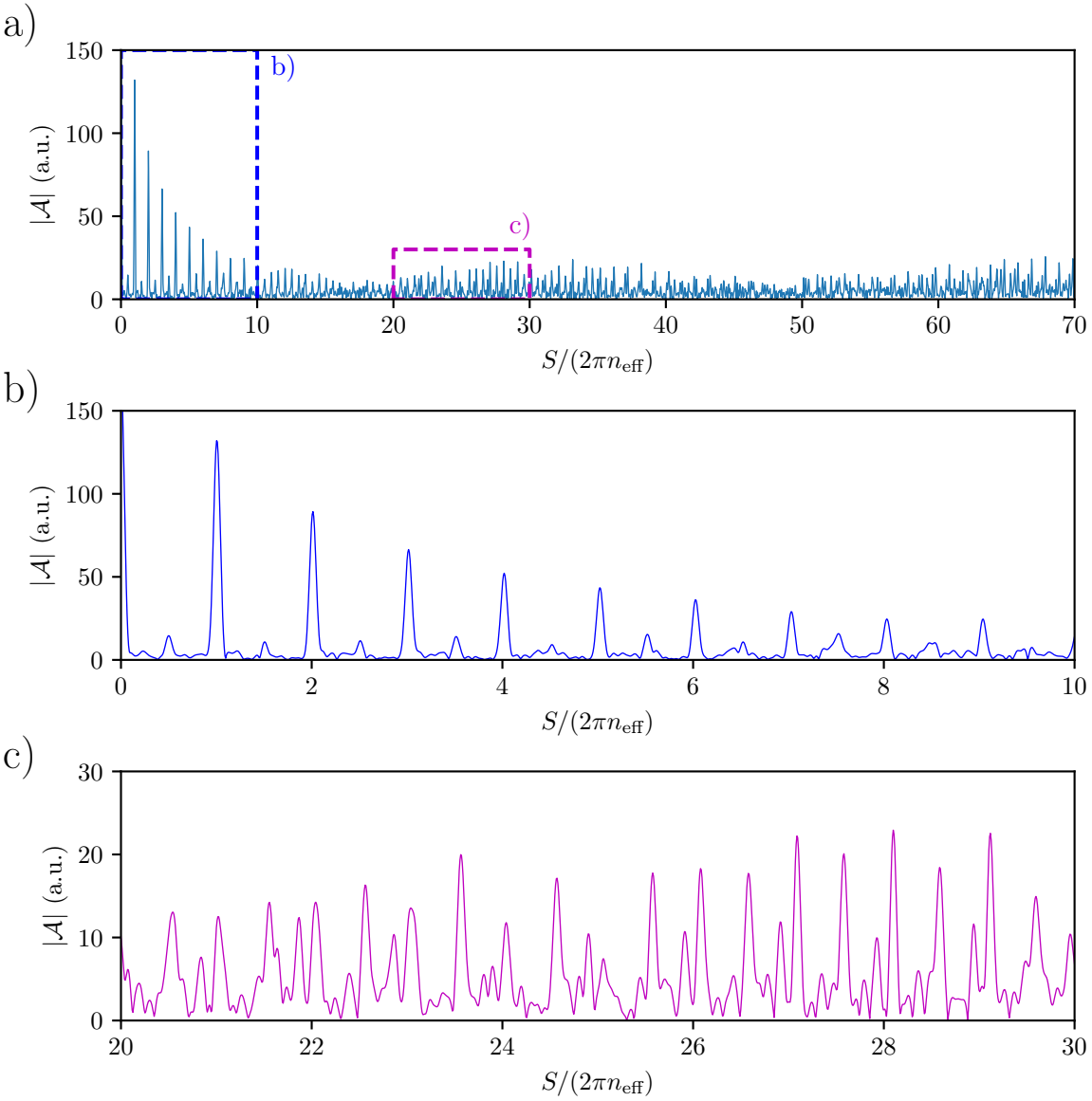

Figure 2.4: Fourier transform of a scaled quantum mechanical spectrum with $n_0 = 5$ done by M. Schumacher [31]. The data is comparable to classical calculations at an energy of $E = -1/(2n_{\text{eff}}^2)$ with $n_{\text{eff}} = 5$. The both lower plots are insights in the upper plot. Subplot b) shows that there are high peaks close to integer numbers of the frequency which corresponds to the scaled classical action $S/(2\pi n_{\text{eff}})$. This is very similar to the hydrogen-like case where those peaks can be assigned to special Kepler ellipses. Subplot c) on the other hand reveals deviations from the hydrogen-like behavior for higher $S/(2\pi n_{\text{eff}})$ as additional peaks occur. It is desired to find classical periodic orbits which belong to the peaks and which reproduce the deviations from the hydrogen-like case.

Figure 2.4 shows the Fourier transform of a scaled quantum mechanical spectrum [31]. Although the peaks have not yet the correct height their position should be about right. We hope to find classical periodic exciton orbits which can be assigned to these peaks by using semiclassical theories. Nevertheless, there are some problems including that M. Schumacher uses slightly different material parameters for his calculations. This might lead to quantitative deviations in our results.

Let us now take a look at the qualitative behavior of the Fourier transformed spectrum. In figure 2.4 b) one can see that there are major peaks near integer values of $S/(2\pi n_{\text{eff}})$ what is similar to the hydrogen atom where these peaks result from classical Keplerian orbits in the Bohr-Sommerfeld model. Nevertheless, the peaks are not exactly at integer values what is a first deviation from the hydrogen-like behavior. Furthermore, additional peaks occur for higher $S/(2\pi n_{\text{eff}})$ like shown in figure 2.4 c).

In the semiclassical case we expect the peaks near integer values to belong to a short orbit which is periodic after one cycle while the other peaks should belong to orbits with higher periods.

3 Results

3.1 Investigations at constant energy

The aim of this section is to calculate the Fourier transformed energy spectrum from the simulated periodic orbits at $n_{\text{eff}} = 5$. Before doing so the orbits are classified using their winding numbers M_1 and M_2 accompanied by a general overview of the orbits' appearance. Then the orbit parameters are investigated in dependence of the winding numbers. We will see that it is possible to interpolate the parameters of most of the orbits which were not simulated by using these dependencies. Afterwards the action variables are calculated and from there the amplitudes and frequencies of the spectrum by using the Berry-Tabor formula.

3.1.1 Orbits and winding numbers

The investigations in this thesis focus on periodic orbits in the symmetry plane of cuprous oxide orthogonal to the [001] axis. Figure 3.1 shows a Poincaré surface of section (PSOS) of the dynamics in this plane at fixed $n_{\text{eff}} = 5$. The central fixed point belongs to the periodic orbit with the highest angular momentum. It appears to be almost circular but slightly deformed according to the squared symmetry of the Hamiltonian. This deformation cannot be seen with the bare eye at $n_{\text{eff}} = 5$.

The central fixed point is surrounded by many rational tori which break up leaving pairs of stable and unstable fixed points according to the Poincaré-Birkhoff theorem [17]. When we go from the center to the edge of the PSOS the angular momentum of the corresponding periodic orbits decreases. Furthermore, not all of the pairs indeed consist of a stable and unstable partner orbit since for most of the shown tori both orbits are marginally stable. This can bee seen directly in the PSOS in figure 3.2 which shows a small region of the former PSOS in more detail. The distinction between stable and unstable fixed points is clearest for the orbit pair with winding number $M_1 = 8$. The stable fixed points are also called elliptic fixed points because a small deviation will stay near the fixed point and form an ellipse as can be seen in the figure. The

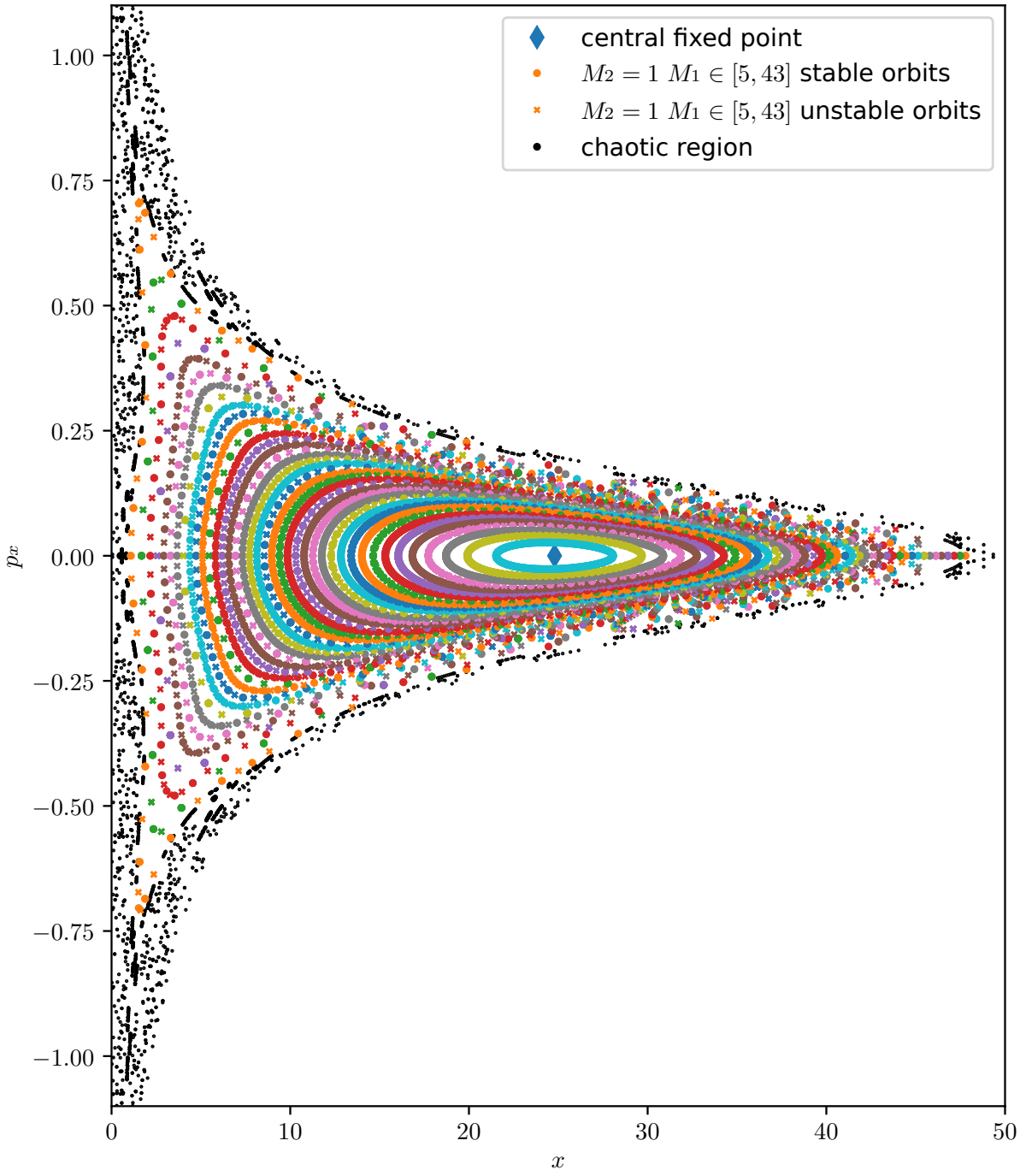

Figure 3.1: Poincaré surface of section at $n_{\text{eff}} = 5$. In the center one can see a stable and isolated fixed point which belongs to the orbit with the highest angular momentum. It is surrounded by tori which break up leaving altering stable and unstable fixed points. The angular momentum of the corresponding orbit pairs is smaller the closer they are to the edge. Beyond the outer torus with $M_1 = 5$ the system becomes chaotic what is indicated through the black dots. The accumulations of black dots indicate further periodic orbits in that region but they belong to winding numbers $M_2 > 1$.

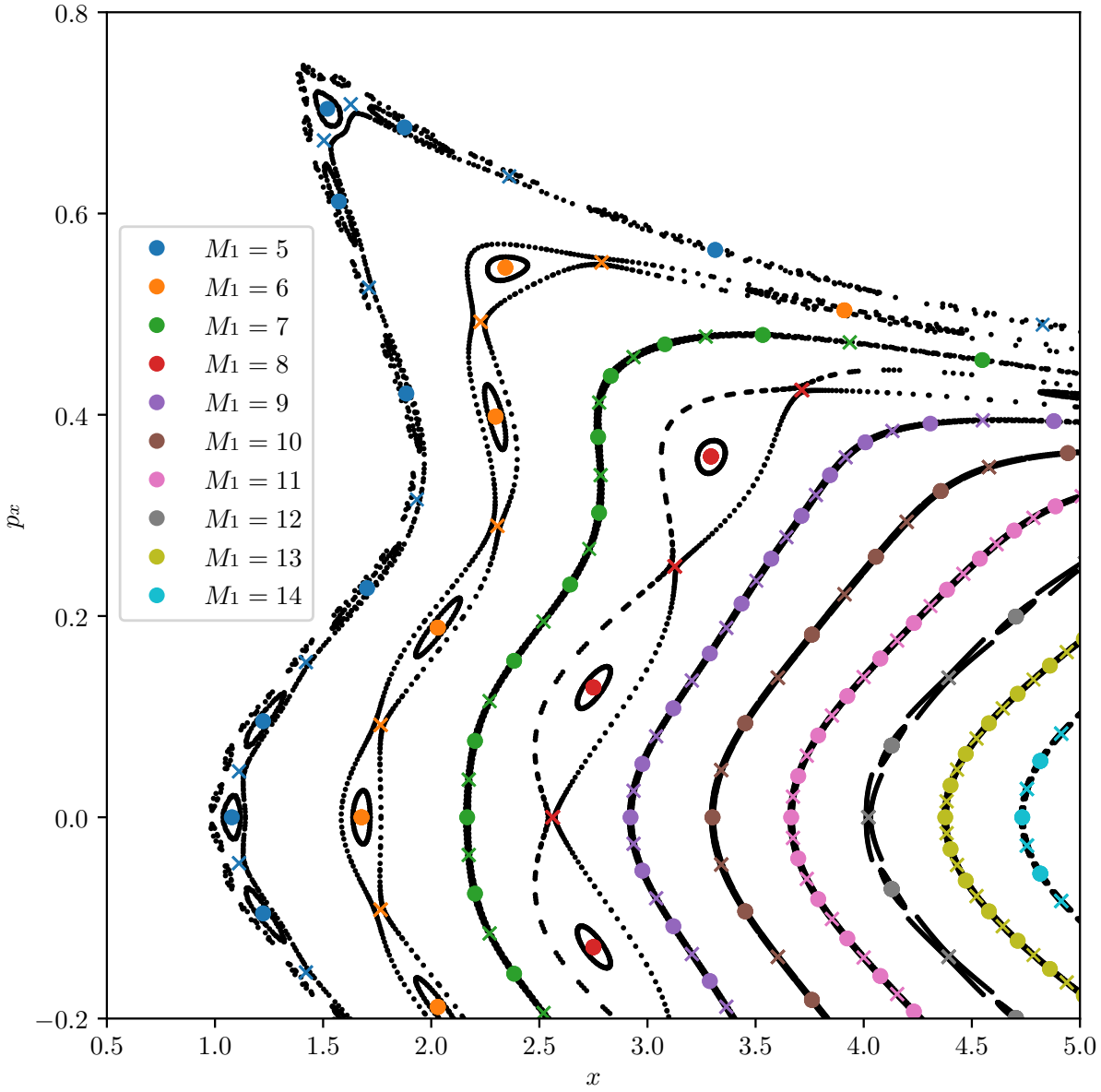

Figure 3.2: Poincaré surface of section at $n_{\text{eff}} = 5$. The black dots belong to non periodic orbits originating from small deviations of the starting conditions of the periodic orbits. The figure reveals that elliptic stable and hyperbolic unstable fixed points can be identified only for $M_1 \in [5, 6, 8, 12]$. The other fixed points show no clear visible difference in their behavior even when taking a closer look at them than in this figure.

unstable fixed points are also called hyperbolic fixed points because a small deviation will move away from the fixed point. In the PSOS you can see a cross where such points appear. A distinction between elliptic and hyperbolic fixed points occurs only for $M_1 \in [5, 6, 8, 12]$, the other tori form lines in the PSOS. As we will see later, the relevant stability eigenvalues of those orbits are also very close to one and for most fixed points it is not possible to identify elliptic and hyperbolic fixed points even by using their stability eigenvalues. The assignment of stable and unstable in the PSOS is done for reasons of classification based on the fact that all orbits with distinct eigenvalues and high symmetries ($M_1 = 4n$, $n \in \mathbb{N}$) have an unstable fixed point on the $p_x = 0$ axis while the orbits with $M_1 \neq 4n$ have a stable fixed point here.

At the edge of the PSOS in figure 3.1 one can see a chaotic region beyond the last torus with $M_1 = 5$ indicated by the black dots. Note that the PSOS contains only orbits with $M_2 = 1$ but also orbits with higher M_2 occur.

The orbits are classified through the winding numbers M_1 and M_2. Figure 3.3 a) shows the appearance of the orbits where M_1 equals the number of ellipses the orbit consists of while M_2 describes the number of rotations of these ellipses around the z-axis which can be seen in figure 3.3 b). Both numbers sum up to the total number of cycles

$$n_{\text{cycle}} = M_1 + M_2. \tag{3.1}$$

Because of the $C_{4\text{v}}$ symmetry of the Hamiltonian in the symmetry plane two orbits are identical when they can be identified by applying $C_{4\text{v}}$ symmetry operations. Having a look at figure 3.3 one can see that the stable partner of an orbit pair has a maximum on a coordinate axis while the unstable pair has one on a bisector. One exception is the case for $M_1 = 4n$, $n \in \mathbb{N}$ where orbits of high symmetry occur. In the stable case maxima are located on both the coordinate axes and the bisectors. In the unstable case there is no maximum located on a coordinate axis or a bisector. An overview of all stable orbits with $M_2 = 1$ can be found in appendix D.

The highest symmetries occur on orbits with $M_1 = 4n$, $n \in \mathbb{N}$ but also orbits with $M_1 = 2n$ have more symmetries than usual. Comparing this to the PSOS in figure 3.2 one can see that orbit pairs with higher symmetry also have a clearer distinction between stable and unstable fixed points. Thereby the $M_1 = 4n$ orbits have a 90° rotation symmetry and can be mirrored at the axes so as their bisectors without being changed. The $M_1 = 2n$ orbits have only a 180° rotation symmetry and can be mirrored at either the axes or their bisectors but not at both. When having a look at the $M_1 = 8$ orbits in figure 3.3 it might look like they have a 45° rotation symmetry but this is not the case because there are slight differences in the appearance of the ellipses on the axis and the one on the bisectors. This direction dependent deformation becomes stronger the lower M_1/M_2 is and can be seen easily at the $M_1 = 5$ orbits.

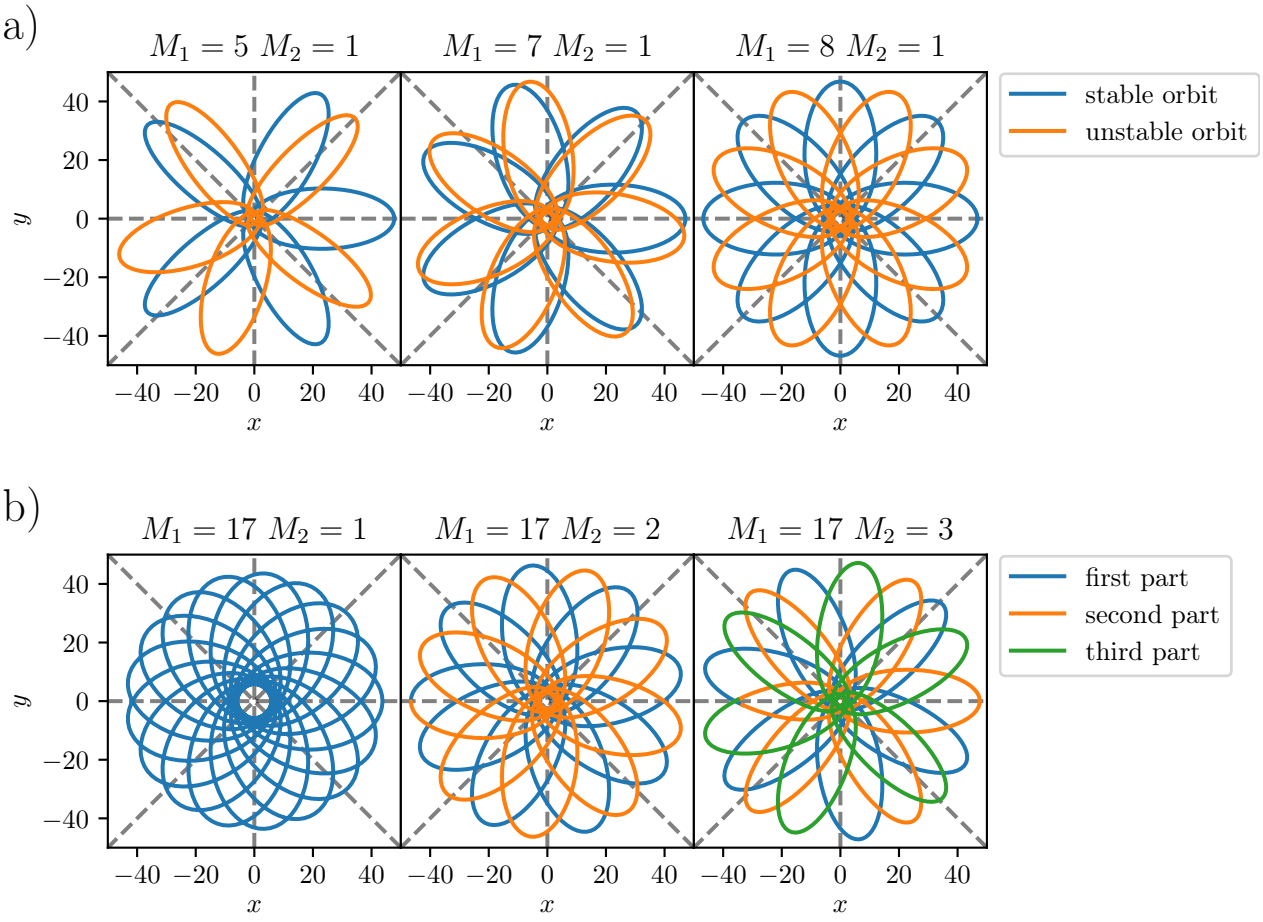

Figure 3.3: Figure a) shows examples for the stable and unstable partner orbits at $n_{\text{eff}} = 5$. The winding number M_1 is defined by the number of Kepler ellipses. The winding number M_2 describes the number of rotations of these ellipses around the center. Figure b) shows orbits with the same M_1 but different M_2 in order to explain what that means for the orbits. For $M_2 = 1$ the quasiparticle passes one neighboring ellipsis after another. In the case of $M_2 = 2$ it passes the blue ellipses first and then the orange one. It works analogously for $M_2 = 3$ and higher.

3.1.2 Orbit parameters

Figure 3.4 shows the time period T and action S of the orbits. Thereby T and S are mean values from the stable and unstable partner orbits which is done because the relative difference between both is smaller than 10^{-7} for most of the orbits and maximal 10^{-4} for orbit pairs with distinct stability. In the case of an unperturbed hydrogen atom it would be $S = 2\pi n_{\text{eff}}$ and $T = 2\pi n_{\text{eff}}^3$ which is why the parameters are scaled like this. In addition it is intuitive that action and period should increase about linearly with $n_{\text{cycle}} = M_1 + M_2$ because a doubled number of cycles around the core will lead to a doubled period. Nevertheless, a deviation from the linear behavior is observed which can be explained by the shape of the ellipses changing when varying M_1/M_2. The deviation is stronger the lower M_1/M_2 is which is expected because of the influence of the band structure being stronger the smaller the distance between electron and hole becomes. The figures in appendix D show that this is indeed the case for low M_1/M_2. Both, action and period, form smooth curves when drawn in dependence of M_1/M_2 even for different values of M_2. This allows for interpolating action and period for arbitrary winding numbers (M_1, M_2) without simulating them explicitly; this is described more detailed in appendix G.

The eigenvalues of the stability matrix are assigned to specific directions by using their eigenvectors. In appendix E the appearance of the eigenvectors and their sorting is described in more detail.

Figure 3.5 a) shows the stability eigenvalues λ_{xy} describing the stability in the plane of symmetry. For most of the shown orbits one cannot see any difference between the stable and unstable orbit because their eigenvalues deviation from one is smaller than the numerical accuracy. Nevertheless, λ_{xy} is clearly distinct from one for some orbits with small M_1/M_2. The actual value of these eigenvalues seems to have no easy dependency on M_1/M_2. The maximal value occurs for $M_1 = 8$, $M_2 = 1$ and the last distinguishable pair occurs at $M_1 = 12$, $M_2 = 1$ where all neighboring orbits' eigenvalues λ_{xy} are one. This can be explained by the higher symmetry of such orbits which makes them shorter in their fundamental region which is also the reason why $M_2 = 3$ provides more unstable orbits than $M_2 = 2$. For $M_2 = 2$ only orbits with an odd M_1 are actual independent because otherwise the orbit would just be two repetitions of an $M_2 = 1$ orbit. Therefore, no orbits with high symmetries can occur while $M_2 = 3$ offers orbits with $M_1 = 16$, 20, 28 and so on which have high symmetries.

The eigenvalue λ_z is shown in figure 3.5 b) and describes the stability out of the plane. As one can see λ_z forms a smooth curve where the eigenvalues of the stable and unstable partner orbits are almost identical. Scaling the eigenvalues from $M_2 = 2$ and $M_2 = 3$ with $\lambda_z^{M_2^{-1}}$ one can see that the eigenvalues of higher M_2 fit in there too. This scaling

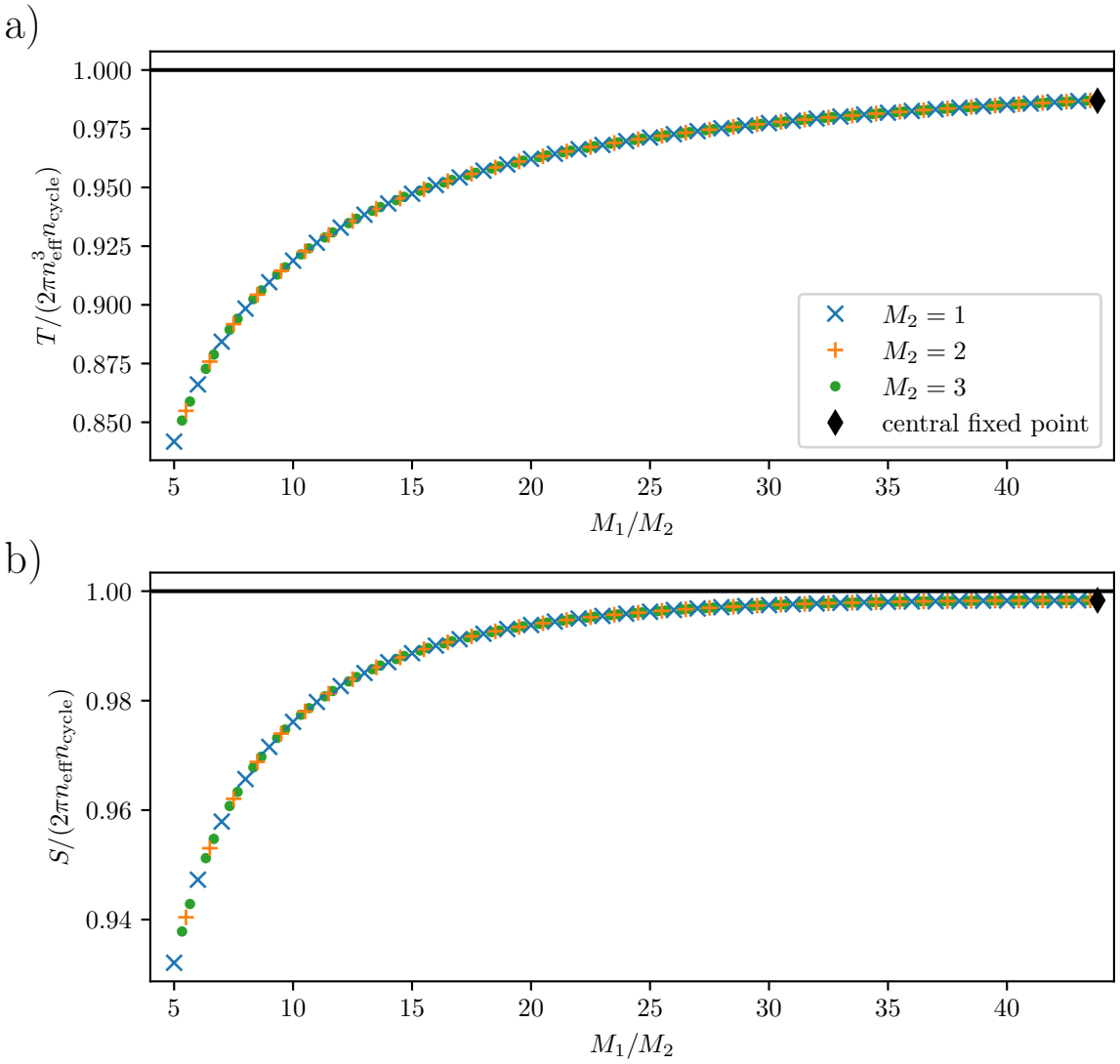

Figure 3.4: Figure a) shows the scaled time period T of the periodic orbits. In the hydrogen-like case the scaling would be $T = 2\pi n_{\mathrm{eff}}^3$ but the perturbed system shows deviations from that behavior. All orbits with $M_2 = 1$, 2 and 3 form a smooth curve what indicates that the period of orbits with higher M_2 can be interpolated from this curve. It will be explained later how the M_1/M_2 ratio of the central fixed point is derived.
The scaled action S in figure b) shows a similar behavior. In the hydrogen-like case the action would scale with $S = 2\pi n_{\mathrm{eff}}$. The fact that all orbits form a smooth curve allows for calculating the action variables through differentiation of the action with respect to M_1. More details can be found in appendix G.

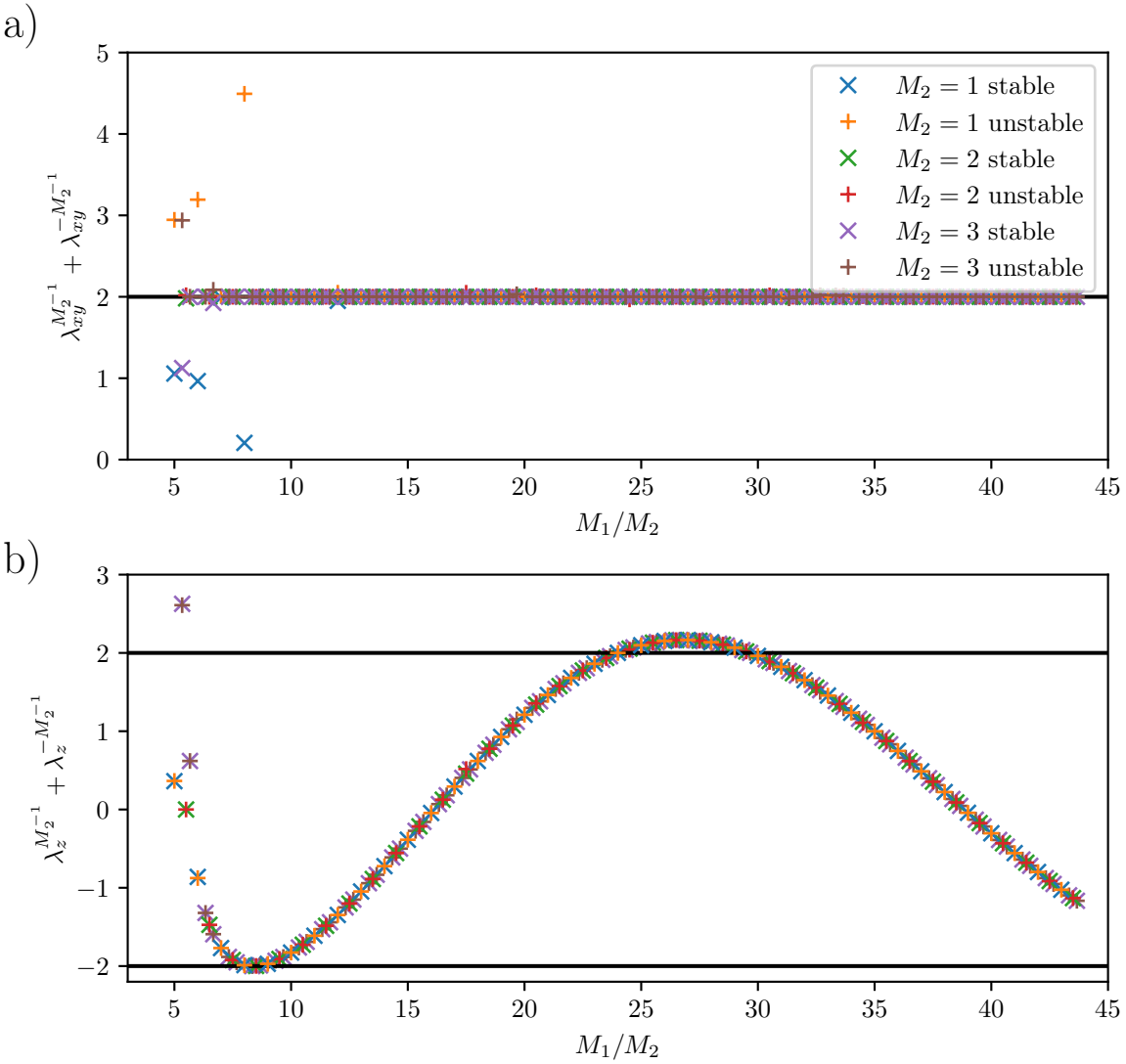

Figure 3.5: Figure a) shows the stability eigenvalues in the plane of symmetry which occur in a pair of λ_{xy} and λ_{xy}^{-1}. They can be represented by their sum $\lambda_{xy} + \lambda_{xy}^{-1}$ where the orbit is stable if the term is between -2 and 2. Only orbits with a low ratio M_1/M_2 show visible differences from 2. The exceptions at $M_1 = 8$ and $M_1 = 12$ can be explained by the higher symmetry of those orbits (see figures D.1 and D.4).
Figure b) shows that the stability eigenvalue out of the plane λ_z turns out to be almost the same for both orbits of a pair. When scaling the eigenvalues for different M_2 with $\lambda_z^{M_2^{-1}}$ they form a smooth curve except for very small ratios $M_1/M_2 < 6$. A fit to this curve allows for interpolating the eigenvalues for higher values of M_2 without simulating those orbits explicitly. The behavior for $M_1/M_2 \in [24.00, 29.68]$ is remarkable because the orbits become unstable here.

results from the stability matrix $\boldsymbol{M}(nT)$ for n periods being $\boldsymbol{M}^n(T)$ and orbits with $M_2 = 2$ being twice as long as orbits with $M_2 = 1$ at the same M_1/M_2 ratio. Therefore, the eigenvalue for $M_2 = 2$ will be the square of the eigenvalue for $M_2 = 1$.

Because all M_2 curves fit together it is possible to interpolate the z-eigenvalues for higher M_2 from this curve what is quite useful when calculating the trace formula amplitude because it is no longer necessary to know each orbit explicitly. The eigenvalues can be calculated from their sum by using

$$\begin{aligned} b &= \lambda + \lambda^{-1}, \\ 0 &= \lambda^2 - b\lambda + 1, \\ \lambda &= \frac{b \pm \sqrt{b^2 - 4}}{2}. \end{aligned} \tag{3.2}$$

Note that the square root term becomes imaginary for an absolute of b smaller than 2 what returns the correct complex eigenvalues at this point. Unfortunately the smooth curve breaks up below $M_1/M_2 = 6$ and an interpolation is no longer possible but this affects only a few orbits per M_2. More information about this can be found in appendix F.

Remarkable is that there is a region $M_1/M_2 \in [24.00, 29.68]$ where the orbits become unstable in z-direction. Such an behavior could be connected to additional bifurcations where the torus breaks up into more than two orbits but until now no such additional orbits were discovered in the [001] symmetry plane. It might be that the partners are located outside the plane. Furthermore, this bifurcation seems to have no effect on the stability in xy-direction because the orbits just remain stable with constant eigenvalues of one.

3.1.3 Trace formula amplitudes

In a next step we want to calculate the amplitudes of the trace formulas which equals the Fourier transform of the scaled quantum mechanical spectrum. Therefore, it is necessary to use separate formulas for the central orbit and the orbit pairs on the rational tori. The central orbit can be taken into account using Gutzwiller's trace formula

$$\rho(n_{\text{eff}}) = \frac{1}{\pi n_{\text{eff}}^3} \sum_{\text{PO}} \frac{T_{\text{PPO}}}{\sqrt{|\det(\boldsymbol{M}_{\text{PO}} - \mathbb{1})|}} \cos\Big(S_{\text{PO}} - \frac{\pi}{2}\sigma_{\text{PO}}\Big) \tag{3.3}$$

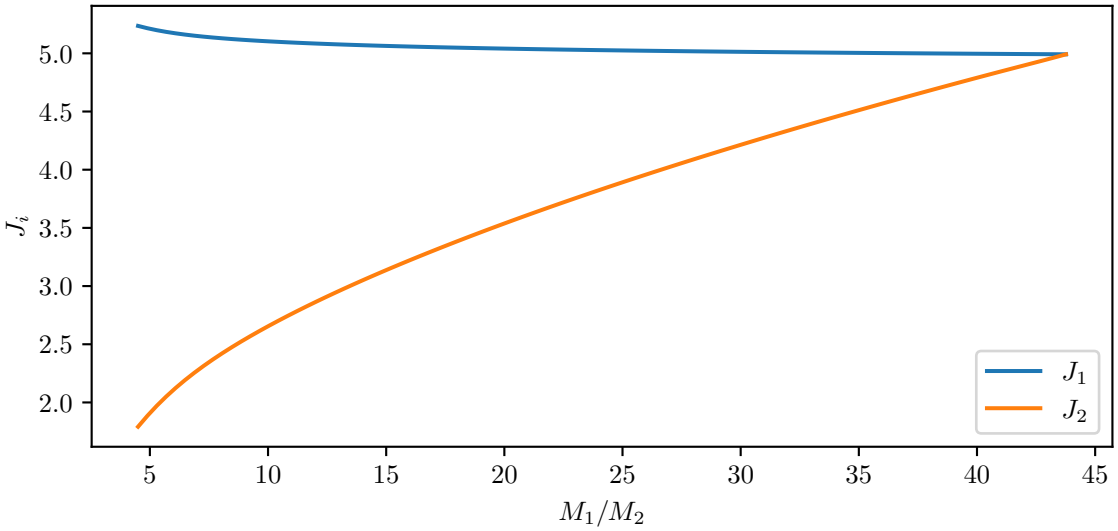

Figure 3.6: The action variables J_1 and J_2 are calculated using the derivative of a polynomial fitted to the action of the orbits with $M_2 = 1$; see appendix G for more details.

since it is stable and isolated. This can be evaluated to

$$\begin{aligned}\rho_{\text{central}}(n_{\text{eff}}) &= \frac{1}{\pi n_{\text{eff}}^3} \sum_{r=1}^{\infty} \frac{T}{\sqrt{|\det(\boldsymbol{M}^r - \mathbb{1})|}} \cos\left(rS - r\frac{\pi}{2}\sigma\right) \\ &= \frac{1}{\pi n_{\text{eff}}^3} \sum_{r=1}^{\infty} \frac{T}{\sqrt{\left|\left(\lambda_{xy}^{r/2} - \lambda_{xy}^{-r/2}\right)^2 \left(\lambda_z^{r/2} - \lambda_z^{-r/2}\right)^2\right|}} \cos\left(rS - r\frac{\pi}{2}\sigma\right) \end{aligned} \tag{3.4}$$

for r repetitions of the orbit. The contribution of an orbit pair is calculated with the mixed Berry-Tabor and Gutzwiller trace formula

$$\rho_{\boldsymbol{M}}(n_{\text{eff}}) = \frac{T_{\boldsymbol{M}}}{\pi n_{\text{eff}}^3 M_2^{3/2} |g_E''|^{1/2} \left|\lambda_z^{1/2} - \lambda_z^{-1/2}\right|} \cos\left(S_{\boldsymbol{M}} - \sigma_{\boldsymbol{M}}\frac{\pi}{2} - \frac{\pi}{4}\right) \tag{3.5}$$

for non-isolated periodic orbits where the winding numbers $\boldsymbol{M} = (M_1, M_2)$ represent the orbit pair. In order to account for multiple repetitions one can rewrite this as

$$\rho_{\boldsymbol{M}}(n_{\text{eff}}) = \sum_{r=1}^{\infty} \frac{rT_{\boldsymbol{M}}}{\pi n_{\text{eff}}^3 (rM_2)^{3/2} |g_E''|^{1/2} \left|\lambda_z^{r/2} - \lambda_z^{-r/2}\right|} \cos\left(rS_{\boldsymbol{M}} - r\sigma_{\boldsymbol{M}}\frac{\pi}{2} - \frac{\pi}{4}\right) \tag{3.6}$$

with $\boldsymbol{M} = (M_1, M_2)$ being the winding numbers of the primitive periodic orbit now. The influence of single orbits and orbit pairs can be investigated by looking at the amplitude

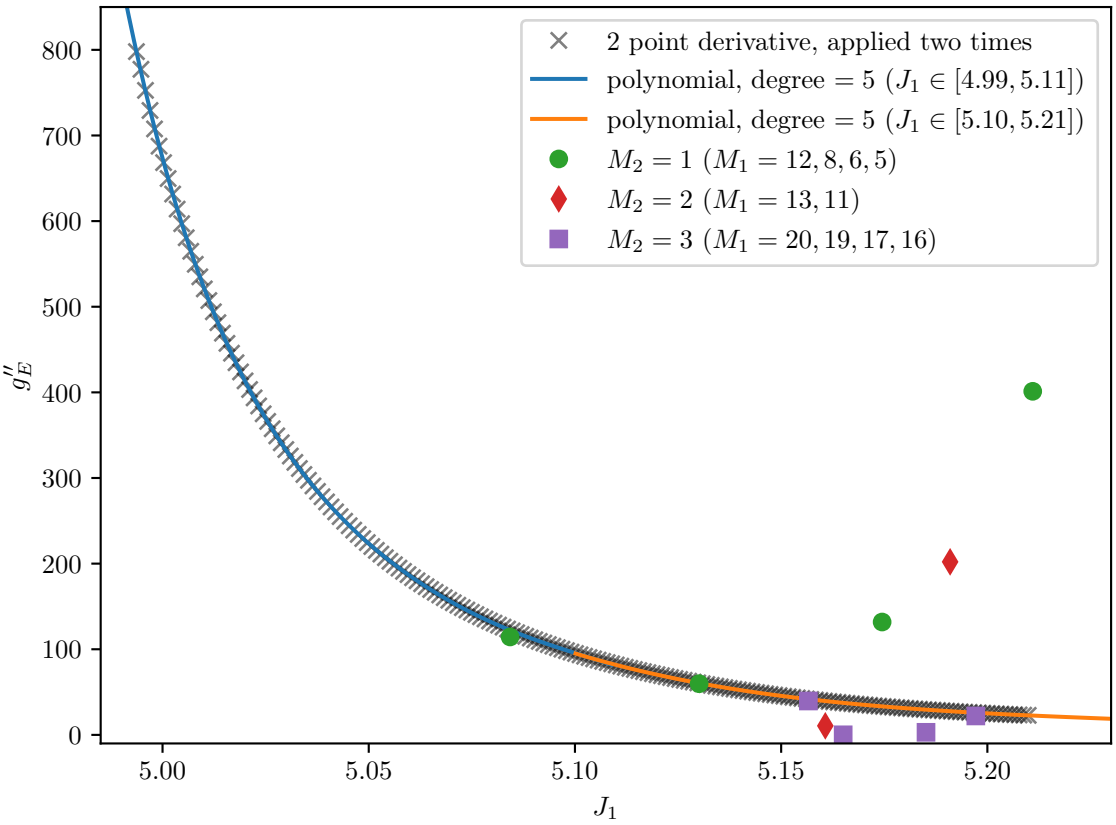

Figure 3.7: Second derivative of $J_2 = g_E(J_1)$. The black x are the numerical second derivative of J_2 after J_1 calculated with a simple 2 point derivative acting on the action variables in figure 3.6. The lines are polynomials fitted to the black x in order to interpolate values in between. The bold points are calculated from the stability eigenvalues using equation (3.7) where the M_1 values label the points from left to right. There are only four points fitting on the curve, two dots and two squares, but those four points represent the orbits $(M_1, M_2) = (12, 1)$, $(8, 1)$, $(20, 3)$ and $(16, 3)$ which are the four shortest orbits with the highest symmetries. They have also the best accuracy because their eigenvalues differ strongly from one and the difference of the action of stable and unstable partner orbit is significantly larger than the numerical noise. Nevertheless, there are three points above the curve also belonging to orbits with high accuracy. The three orbits below the curve on the other hand have only poor accuracy like all other regular orbit pairs with $M_2 \leq 3$ which are not shown here. They have eigenvalues and differences in action which were numerically not resolvable in the simulations. This is why in the following the smooth curves are used for calculations. The fit parameters of these curves are shown in appendix G.

$|\mathcal{A}|$ which is defined as the prefactor of the cosine. This is similar to a Fourier transform in S where we neglect the additional phase related to the Maslov index σ.

Before doing so it is necessary to calculate the function g_E'' which is the second derivative of $g_E(J_1) = J_2$ which describes the connection between the action variables J_1 and J_2 on the energy surface. These variables can be calculated from a polynomial fit to the action S as described in appendix G; the result is shown in figure 3.6. The polynomials for J_1 and J_2 apply not only for $M_2 = 1$ but for all M_2 which is why they can be used to extrapolate the action variables for arbitrary orbit pairs (M_1, M_2).

The central orbit is the limiting case where the radius of the rational torus disappears and the orbit becomes effectively one dimensional (see the PSOS in figure 3.1). The classification with M_1 and M_2 does not hold here but when looking at figure 3.6 one can see that J_1 and J_2 intersect just between $M_1/M_2 = 43$ and 44 and therefore in the area where the central fixed point is located. It turns out that this point with $J_1 = J_2 = 4.99160$ has the same action as the central orbit with $S/2\pi = 4.99160$ and can therefore be connected to it. Using the corresponding ratio $M_1/M_2 = 43.81$ one can plot the central orbit's action and period in figure 3.4 seeing that they fit on the curves too.

For the calculation of g_E'' one can evaluate the polynomials for J_1 and J_2 at a certain number of points between $J_1(M_1 = 43)$ and $J_1(M_1 = 5)$ linearly spaced in J_1. The resulting curve $J_2(J_1)$ can be differentiated by applying a two-point derivative twice. Note that simply differentiating the polynomials analytically would lead to strong deviations at the boundaries which is why it is not done here. In order to get an easy expression for interpolating the values, two polynomials of order 5 are fitted to the resulting curve where the left one is defined until $J_1 = 5.105$ and the second one afterwards. The results are plotted in figure 3.7.

In order to verify the results g_E'' is calculated on a second way using the stability eigenvalues of the stable (s) and unstable (u) partner of an orbit pair with

$$g_E'' = \frac{2}{\pi M_2^3 \Delta S} \left[\frac{1}{\left| \lambda_{\mathrm{s},xy}^{1/2} - \lambda_{\mathrm{s},xy}^{-1/2} \right|} + \frac{1}{\left| \lambda_{\mathrm{u},xy}^{1/2} - \lambda_{\mathrm{u},xy}^{-1/2} \right|} \right]^{-2} . \tag{3.7}$$

The problem is that this formula works only for orbits where the eigenvalues and the difference of the action of stable and unstable orbit $\Delta S = (S_u - S_s)/2$ can be resolved numerically in the simulations which is the case only for a few orbit pairs. It turns out that the four shortest investigated orbit pairs with the highest symmetries ($(M_1, M_2) = (8, 1)$, $(12, 1)$, $(16, 3)$ and $(20, 3)$) fit on the curve while the others do not. The fact that the most accurate orbits fit on the curve suggests that the first method is valid and therefore it will be used for further calculations. Nevertheless, there are three orbits ($(M_1, M_2) = (5, 1)$,

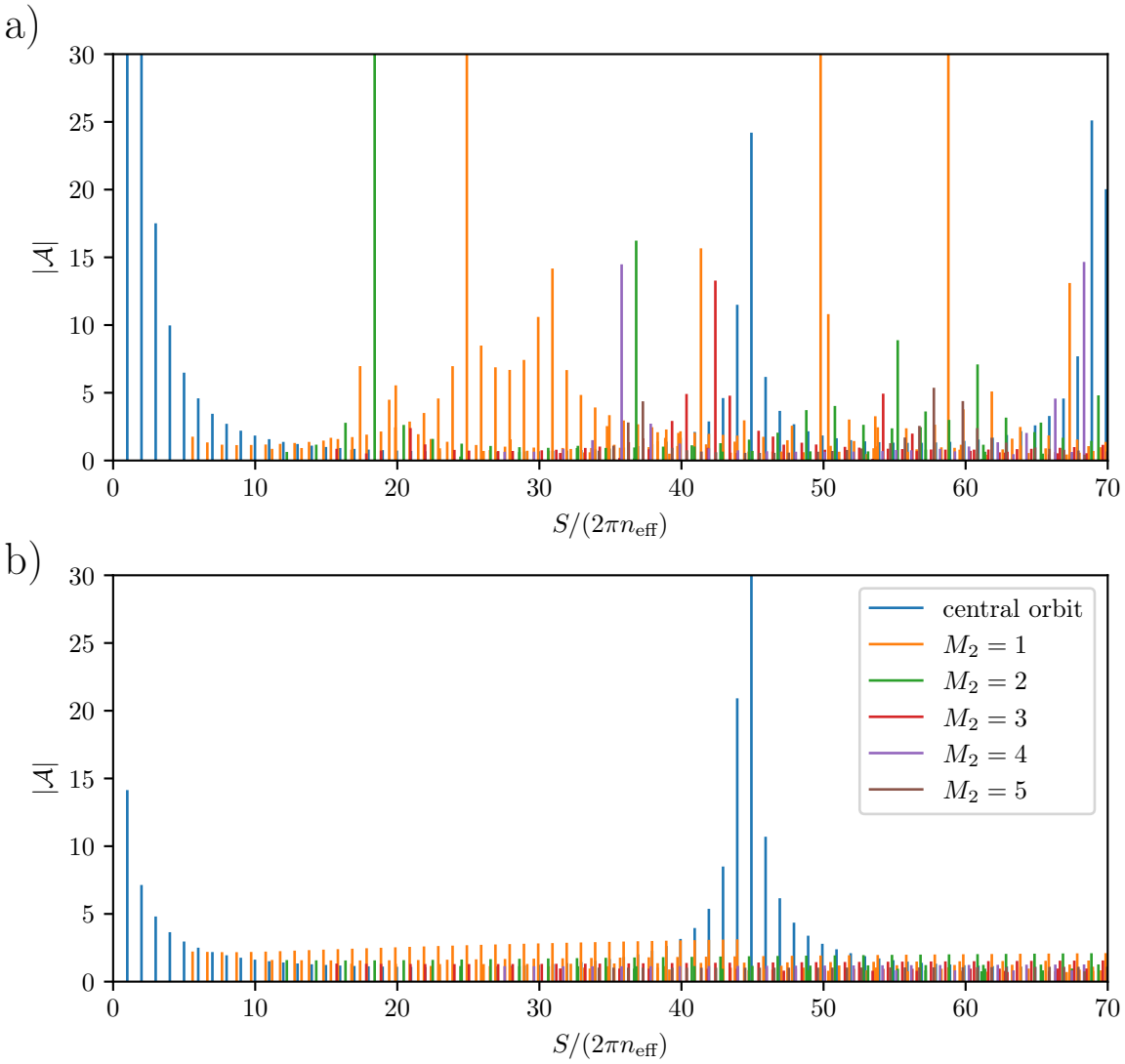

Figure 3.8: Figure a) contains the amplitudes $|\mathcal{A}|$ of the trace formulas over the action scaled with $S/(2\pi n_{\text{eff}})$. The amplitudes are the contribution of one specific orbit without the oscillating phase $\cos(i(S - \pi\mu/2 - \pi/4))$ (like a Fourier transform). The contribution of the central orbit is calculated with Gutzwiller's trace formula (3.4) while for the other orbit pairs a mixed Berry-Tabor and Gutzwiller formula (3.6) is used with g''_E taken from the interpolation in figure 3.7. It is possible to identify some similarities to the Fourier transformed scaled quantum mechanical spectrum in figure 2.4. There are main peaks arising from the central orbit and secondary peaks from the orbit pairs. A more detailed comparison is shown in figure 3.9.
Figure b) shows the same as figure a) but with the difference that the stability eigenvalue λ_z is not taken into account in the formulas ($|\lambda_z^{r/2} - \lambda_z^{-r/2}| \equiv 1$). By comparing the two plots one can see which peaks result from $\lambda_z^r \approx 1$ singularities.

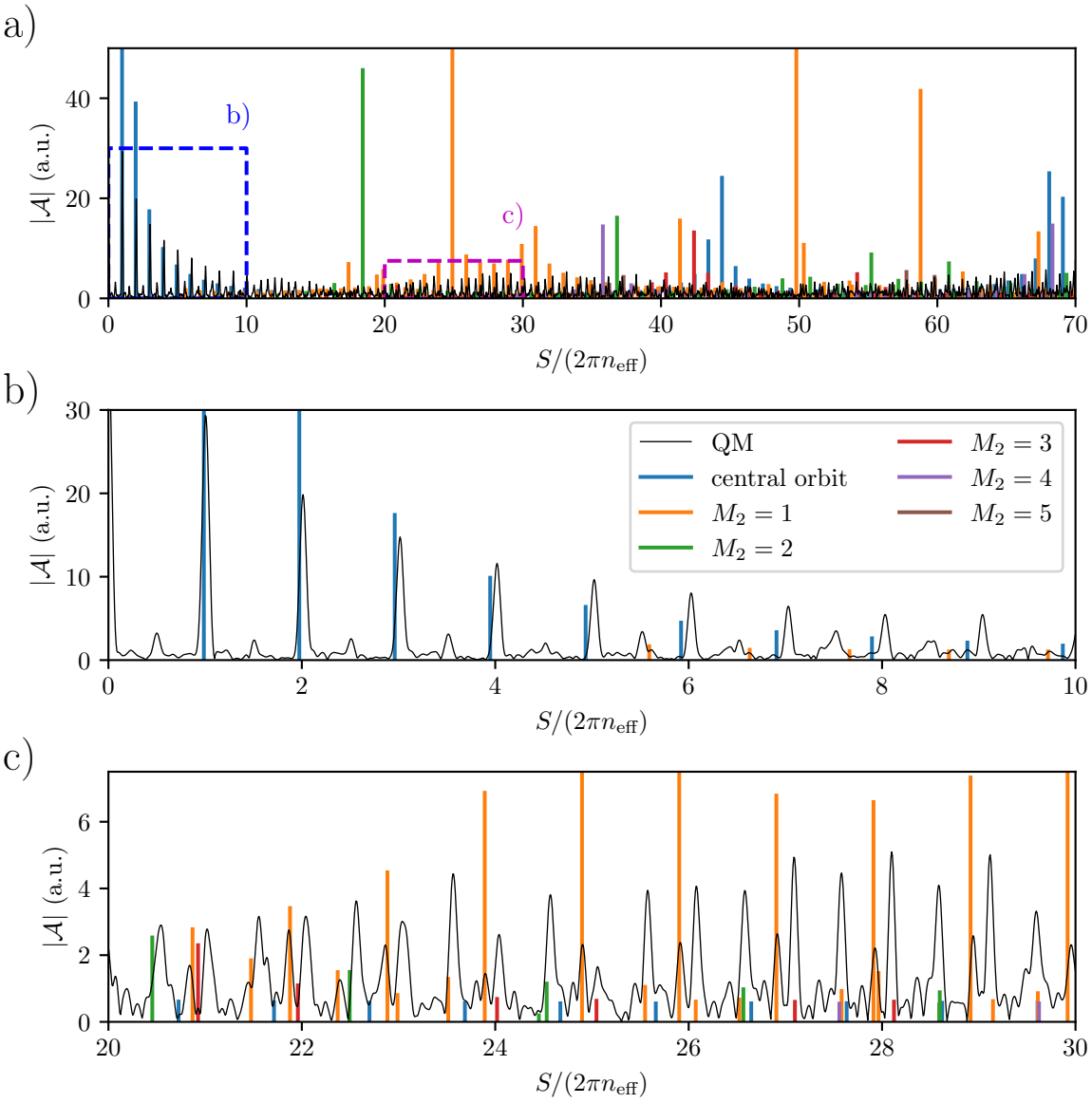

Figure 3.9: The figure shows a comparison of the Fourier transformed scaled quantum mechanical spectrum (QM) at $n_0 = 5$ [31] and the semiclassical amplitudes for $n_{\text{eff}} = 5$ in one plot. The amplitudes are scaled arbitrarily in order to make it easier to compare the positions of the peaks. Subplot b) shows that the peaks from the central orbit do not intersect with the major peaks. It might be that they result from the central orbit in the distinct symmetry plane of Cu_2O. The other subplot c) shows a region where additional peaks occur. As one can see some of the additional peaks can already be identified with specific orbits. Especially the $M_2 = 1$ orbits which are comparably strong are located at peak positions. Nevertheless, some peaks occur at positions where no orbit is located. But of course our semiclassical calculations are limited to one symmetry plane of the crystal and do not take into account the distinct symmetry plane or three-dimensional orbits which is why many orbits are missing here.

$(6,1)$ and $(11,2)$) which differ strongly from the curve but are also simulated with high enough accuracy. The difference is that they do not have that much symmetries as the $M_1 = 4n$ orbits which might imply a connection to the symmetry here. However, the value from the polynomial fit is taken for these orbit pairs too in order to stay consistent.

Finally it is possible to use g_E'' to calculate the amplitudes as described above. They are plotted in figure 3.8 a) in dependence of the action scaled with $S/(2\pi n_{\text{eff}})$. The high peaks result from λ_z being almost one what leads to singularities. This can be verified by calculating the amplitudes without taking λ_z into account (this means setting $|\lambda_z^{r/2} - \lambda_z^{-r/2}| = 1$) which can be seen in figure 3.8 b). In analogy to the hydrogen atom peaks arise close to integer values of $S/2\pi n_{\text{eff}}$. These peaks result from the central orbit. A summary of the peaks resulting from the first twenty repetitions of this orbit are listed in table 3.1. Furthermore, one can see additional peaks which result from the orbit pairs and are a clear deviation from the hydrogen-like behavior. This is also what we expect from the Fourier transform of the scaled quantum mechanical spectrum in figure 2.4 which also shown the major peaks at about integer values and additional peaks.

Figure 3.9 shows both the quantum mechanical (QM) and semiclassical amplitudes in one plot. Note that this comparison is not yet accurate because of slightly different material parameters and due to the fact that the amplitudes of the QM spectrum are not calculated with a precise method. However, we compare them anyway since they should be at least similar.

One can see that the peaks of the central orbit do not coincide with the major peaks of the QM amplitudes but with small secondary peaks nearby. Furthermore, the amplitude of the central orbit decays more strongly with $S/(2\pi n_{\text{eff}})$ than the major QM peaks. This indicates that the major peaks arise from other orbits, maybe from a central orbit in the distinct symmetry plane of the crystal. Nevertheless, some of the QM peaks can be identified with specific orbits as can be seen in subplot c). Especially the $M_2 = 1$ orbits fit well to some of the additional peaks. Another difference are the small QM peaks at half numbers which could not be reproduced in the semiclassical calculations.

In order to compare the amplitudes and parameters of the classical periodic orbits directly they are listed in table 3.2 for all regular orbits with $M_2 = 1$. For winding numbers $M_1 \leq 12$ both the stable and unstable orbit are given in order to compare them. For the other orbit pairs the difference of their parameters is smaller than the numerical accuracy.

Table 3.1: Scaled parameters and Gutzwiller amplitude for the central orbit and for r repetitions of it.

r	$T/(2\pi n_{\text{eff}}^3)$	$S/(2\pi n_{\text{eff}})$	$\lambda_{xy}^r + \lambda_{xy}^{-r}$	$\lambda_z^r + \lambda_z^{-r}$	$\mathcal{A}$
1	0.986 929	0.998 321	1.980	1.992	155.286
2	1.973 858	1.996 641	1.921	1.967	38.958
3	2.960 787	2.994 962	1.825	1.927	17.416
4	3.947 716	3.993 283	1.692	1.870	9.877
5	4.934 645	4.991 604	1.526	1.799	6.388
6	5.921 574	5.989 924	1.329	1.712	4.494
7	6.908 503	6.988 245	1.107	1.612	3.353
8	7.895 432	7.986 566	0.862	1.499	2.613
9	8.882 361	8.984 886	0.601	1.373	2.107
10	9.869 290	9.983 207	0.327	1.236	1.746
11	10.856 219	10.981 528	0.047	1.088	1.480
12	11.843 148	11.979 848	−0.233	0.932	1.278
13	12.830 077	12.978 169	−0.509	0.769	1.123
14	13.817 006	13.976 490	−0.776	0.599	1.001
15	14.803 935	14.974 811	−1.026	0.424	0.904
16	15.790 864	15.973 131	−1.257	0.246	0.826
17	16.777 793	16.971 452	−1.463	0.065	0.763
18	17.764 722	17.969 773	−1.639	−0.116	0.711
19	18.751 651	18.968 093	−1.784	−0.296	0.670
20	19.738 580	19.966 414	−1.893	−0.473	0.636

Table 3.2: Scaled parameters and trace-formula amplitude for the orbits with $M_2 = 1$. The flag s/u denotes the stable or unstable partner orbit. For $M_1 > 12$ only the stable orbits are listed because the parameters of the stable and unstable orbit are identical.

M_1	s/u	$T/(2\pi n_{\text{eff}}^3)$	$S/(2\pi n_{\text{eff}})$	$\lambda_z + \lambda_z^{-1}$	g_E''	$\lvert\mathcal{A}\rvert$
5	s	5.050 455	5.592 702	0.362	22.556	1.662
5	u	5.050 544	5.592 725	0.365	22.556	1.662
6	s	6.062 691	6.630 981	−0.861	33.304	1.241
6	u	6.062 984	6.631 067	−0.876	33.304	1.241
7	s	7.074 496	7.663 237	−1.770	46.210	1.072
7	u	7.074 497	7.663 237	−1.770	46.210	1.072
8	s	8.085 037	8.690 881	−1.988	60.426	1.042
8	u	8.086 217	8.691 237	−1.989	60.426	1.042

9	s	9.096 439	9.715 552	−1.971	75.340	1.052
9	u	9.096 439	9.715 552	−1.971	75.340	1.052
10	s	10.106 949	10.737 367	−1.828	90.755	1.085
10	u	10.106 949	10.737 366	−1.828	90.755	1.085
11	s	11.117 270	11.756 966	−1.613	106.579	1.133
11	u	11.117 270	11.756 966	−1.613	106.579	1.133
12	s	12.127 419	12.774 675	−1.347	122.271	1.199
12	u	12.127 450	12.774 679	−1.348	122.271	1.199
13	s	13.137 473	13.790 751	−1.047	138.680	1.278
14	s	14.147 406	14.805 382	−0.724	155.806	1.374
15	s	15.157 252	15.818 730	−0.387	173.498	1.490
16	s	16.167 023	16.830 924	−0.045	191.631	1.633
17	s	17.176 729	17.842 072	0.293	210.133	1.814
18	s	18.186 378	18.852 265	0.619	228.976	2.046
19	s	19.195 977	19.861 583	0.927	248.158	2.353
20	s	20.205 533	20.870 093	1.210	267.692	2.779
21	s	21.215 047	21.877 854	1.463	287.596	3.413
22	s	22.224 526	22.884 920	1.681	307.892	4.483
23	s	23.233 971	23.891 335	1.861	328.599	6.869
24	s	24.243 387	24.897 142	2.000	349.732	180.786
25	s	25.252 772	25.902 376	2.098	371.299	8.389
26	s	26.262 133	26.907 072	2.152	393.302	6.785
27	s	27.271 470	27.911 262	2.165	415.738	6.591
28	s	28.280 781	28.914 969	2.136	438.599	7.329
29	s	29.290 072	29.918 221	2.067	461.875	10.504
30	s	30.299 341	30.921 040	1.962	485.555	14.077
31	s	31.308 589	31.923 447	1.822	509.625	6.580
32	s	32.317 819	32.925 461	1.652	534.071	4.743
33	s	33.327 029	33.927 100	1.455	558.870	3.821
34	s	34.336 223	34.928 383	1.236	584.000	3.252
35	s	35.345 398	35.929 321	0.999	609.437	2.862
36	s	36.354 553	36.929 929	0.748	635.163	2.578
37	s	37.363 698	37.930 226	0.488	661.169	2.363
38	s	38.372 821	38.930 217	0.223	687.449	2.196
39	s	39.381 931	39.929 919	−0.042	713.985	2.063
40	s	40.391 022	40.929 339	−0.304	740.733	1.956
41	s	41.400 097	41.928 488	−0.557	767.619	1.869
42	s	42.409 158	42.927 378	−0.799	794.631	1.799
43	s	43.418 203	43.926 016	−1.025	822.106	1.741

3.2 Investigations for varying energy

After the investigations at $n_{\text{eff}} = 5$ we want to know more about the energy-dependence of the orbit parameters in order to be able to calculate an energy dependent spectrum. Until now there is not enough data for such calculations but it was possible to derive the energy dependence of the important central orbit which is shown in the following. However, it turned out that using only this orbit is not sufficient. Afterwards the energy dependence of a selection of orbits with small winding numbers is investigated.

3.2.1 Energy dependence of the central fixed point

At first we want to look at the central orbit. As told before it looks almost circular especially for high n_{eff}. The central fixed point is of special interest because it is isolated, stable and belongs to the shortest periodic orbit with the highest angular momentum. It has therefore a very high contribution to the sums in the semiclassical trace formulas which could be verified in the previous section.

Figure 3.10 a) shows the action and period of the central orbit. They are scaled in a way that the scaled action and period would be one in the hydrogen-like case. It seems that they converge to the same value for high n_{eff} which is hydrogen-like behavior but since this value is about 0.993 and not one there are also differences remaining.

The eigenvalues of the central orbit are plotted as stability angles $\mathrm{i}\nu_i = \ln(\lambda_i)$ in figure 3.10 b). As one can see the eigenvalues λ_{xy} and λ_z tend to one for high n_{eff}. The difference from one is thereby larger for λ_{xy} than for λ_z. Both eigenvalues remain stable over the full investigated range of $n_{\text{eff}} \in [1.5, 30]$. Furthermore, the double logarithmic plot reveals a scaling of the angles with n_{eff}^{-2} in the limit of high n_{eff}. By using this it might be possible to extrapolate to higher n_{eff}. This can be useful because it is not easy to access this range in quantum mechanical calculations or experiments.

3.2.2 Behavior of a selection of orbits with $M_2 = 1$

In this section orbits with winding numbers $M_1 = 4$, 5, 6, 7, and 8 are investigated for n_{eff} varying in a range between 3 and 7. They are interesting because they have stability eigenvalues distinct from one, except $M_1 = 7$, and are therefore good examples for investigating the energy dependence of the system.

In this section two orbit pairs occur which behave not quite regular. They are called $M_1 = 4$ and $M_1 = 5$ (a). In order to introduce them they are shown in the Poincaré

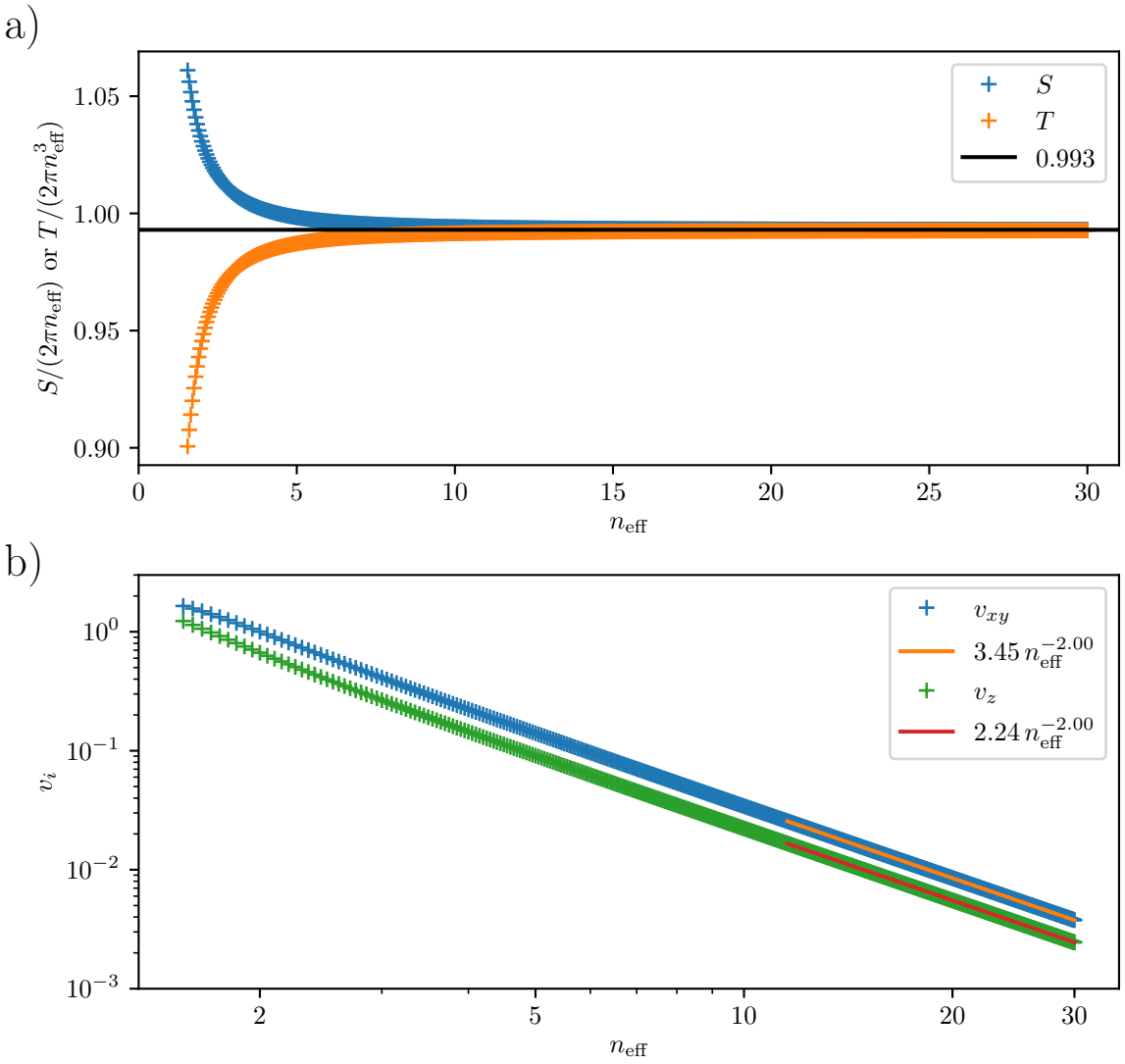

Figure 3.10: Parameters of the central orbit in dependence of n_{eff}. Figure a) shows the scaled action and period of the central orbit for varying n_{eff} in a wide range. One can see that both parameters tend to the same value of about 0.993 in the limit of high n_{eff} while in the hydrogen-like case both would be one.
The stability eigenvalues of the central fixed point can be expressed through the stability angles $\mathrm{i}v_i = \ln(\lambda_i)$ which can be seen in figure b). The eigenvalues tend to one for high n_{eff} since the corresponding angles tend to zero. Furthermore, one can identify a scaling of the angles with n_{eff}^{-2} in the limit of high n_{eff}. This may be useful for further investigations e.g. using Gutzwiller's trace formula to calculate the density of states and to extrapolate further values without explicitly simulating them.

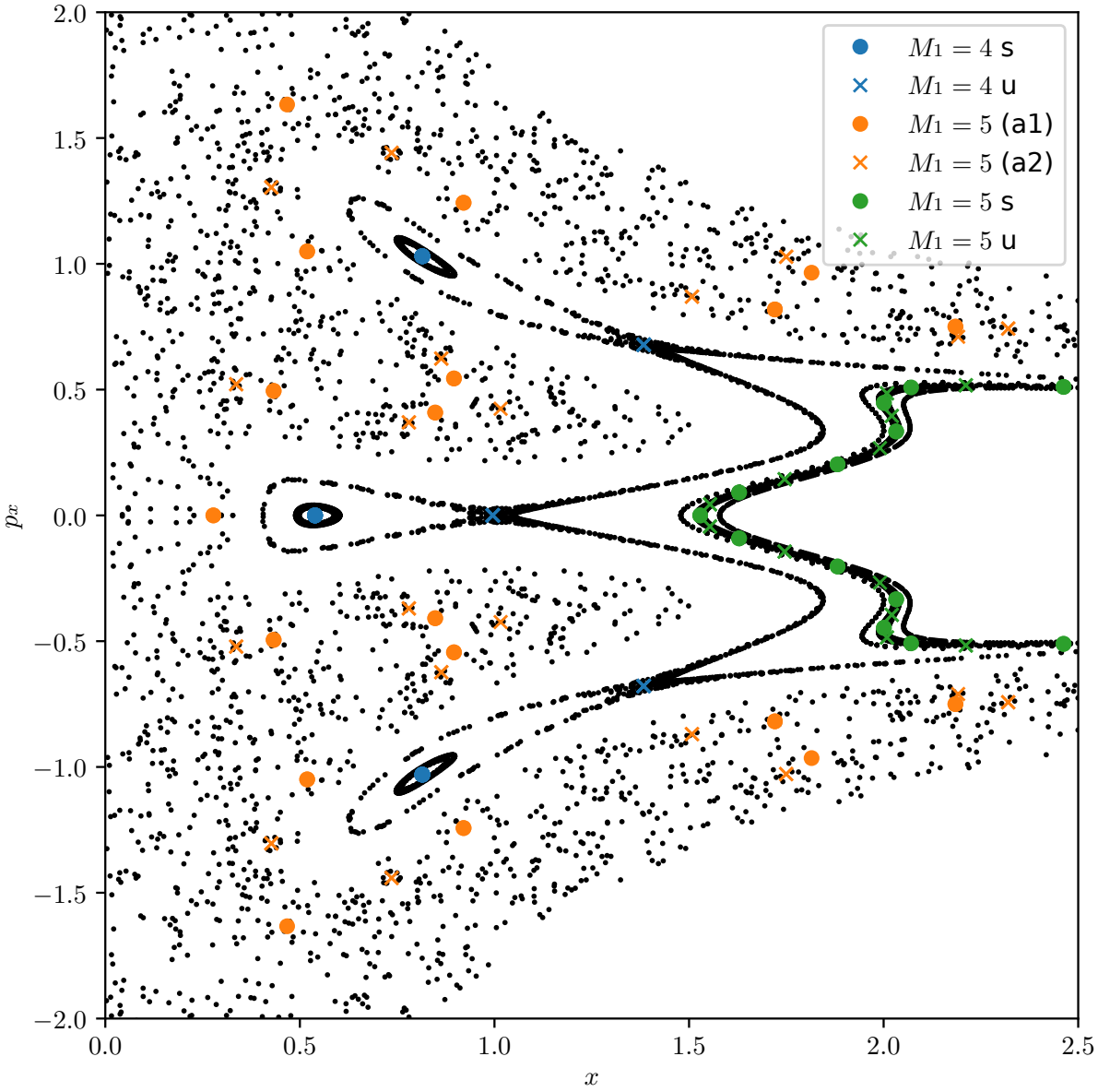

Figure 3.11: Poincaré surface of section for the $M_1 = 4$ and both $M_1 = 5$ orbit pairs at $n_{\text{eff}} = 3$. One can see that the $M_1 = 5$ (a) pair is located inside the chaotic region while the other $M_1 = 5$ pair shows regular behavior. The $M_1 = 4$ pair shows a special behavior. It seems to be not chaotic but in contrast to other regular pairs the stable and unstable fixed points do not alter but form loops.

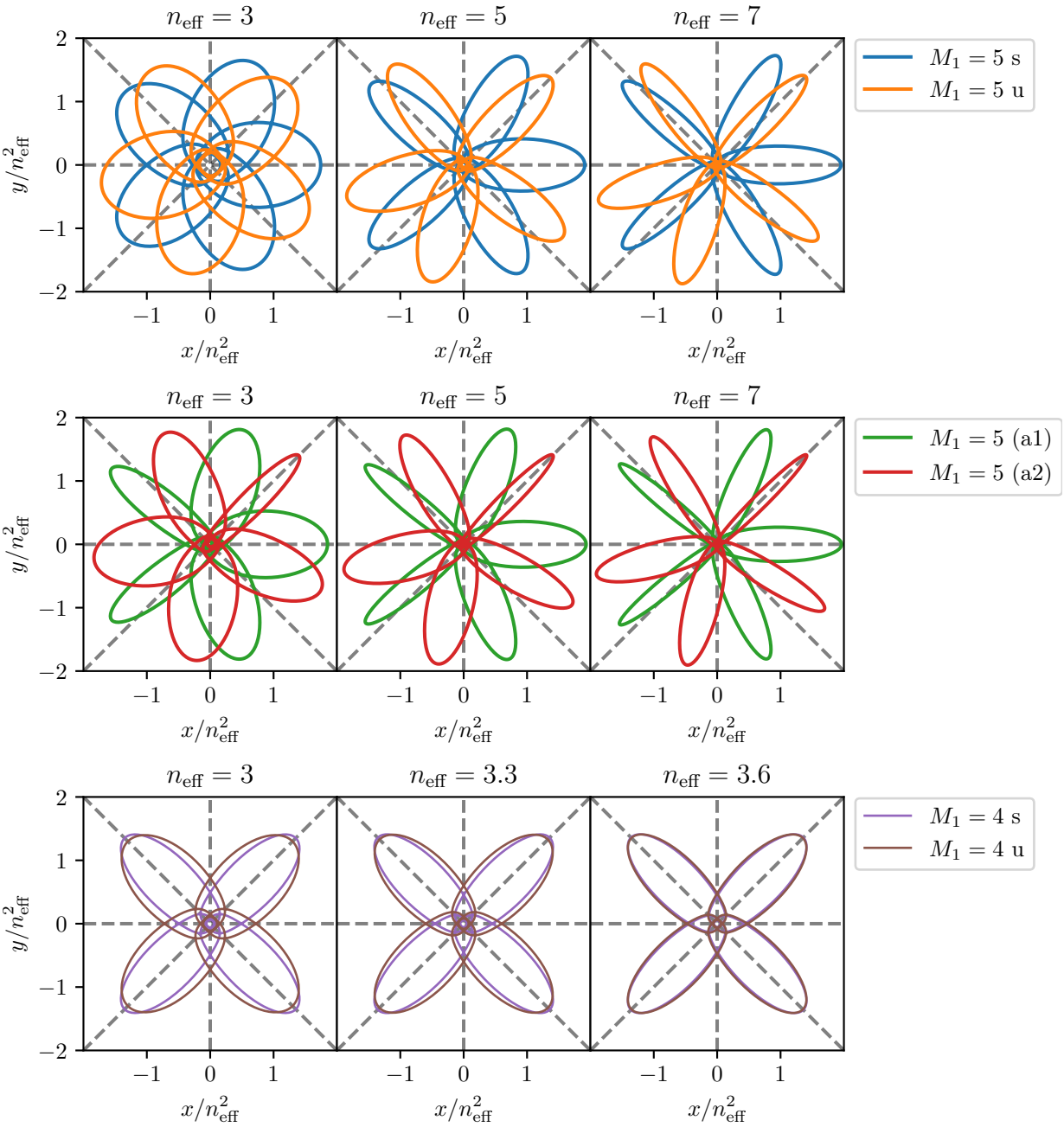

Figure 3.12: The figure shows an example for how the appearance of the orbits change with n_{eff}. As one can see the ellipses of the orbits become narrower with increasing n_{eff} but the orientation of the stable (s) and unstable (u) orbit does not change. Furthermore, the radius of the orbit increases with n_{eff}^2. The upper plots belong to the regular $M_1 = 5$ orbits while the orbits in the middle are located in the chaotic region. The orbits with $M_1 = 4$ in the lower plots are different. As one can see they share the same symmetry and become similar for increasing n_{eff}. They indeed disappear between $n_{\text{eff}} = 3.6$ and 3.65. The other way around they are created at this point in a tangent bifurcation.

surface of section (PSOS) in figure 3.11. As one can see the $M_1 = 5$ (a) orbits are located in the chaotic region while the regular $M_1 = 5$ orbits are not. The $M_1 = 4$ orbits are not chaotic and show a clear separation in elliptic stable and hyperbolic unstable fixed points. However, they appear to be different from the other regular pairs since the fixed points are arranged in a different way. While they alter on the torus for other pairs they are arranged in loops here.

In order to investigate how the orbits' shape behaves under a change of energy, orbits with $M_1 = 5$ and different n_{eff} are plotted in figure 3.12. It turns out that for high n_{eff} the ellipses become narrower but that their orientation remains the same. The radius of the orbits scales with about n_{eff}^2. One can see that the ellipses of the chaotic $M_1 = 5$ (a) orbits are narrower than for the regular $M_1 = 5$ orbits. The orbits with $M_1 = 4$ behave different since both the stable and unstable orbit share the same arrangement of their ellipses. The only difference is that the stable ellipses are narrower. With increasing n_{eff} the difference between both orbits becomes smaller until they become identical somewhere between $n_{\text{eff}} = 3.6$ and 3.65. For higher n_{eff} they cannot be found which is why they are created here in a tangent bifurcation.

In figure 3.13 a) the period of the orbit pairs is plotted. It turns out that both orbits of a pair have about the same period except $M_1 = 4$, even the $M_1 = 5$ (a) pair has similar periods. In the hydrogen-like case the period would scale with $2\pi n_{\text{eff}}^3$. The plot shows that this behavior is approximated in the limit of high n_{eff} since the curves seem to saturate but because they do not approximate a value of one there is an additional factor which is different for each pair. The action is plotted in figure 3.13 b). Scaling it with $2\pi n_{\text{eff}}$ and n_{cycle} reveals deviations from the hydrogen-like behavior. The action is thereby almost identical for both orbits of a pair. In contrast to the period the curves do not saturate but it is likely that they will do outside the investigated range of $n_{\text{eff}} \in [3, 7]$ since the second derivative seems to be positive.

Having a look at figure 3.14 one can see the stability eigenvalues in the plane of symmetry λ_{xy} for the different orbits. The regular orbit pairs all show a similar behavior. Their eigenvalues' difference from one increases with increasing n_{eff}. For the unstable orbits this means an increasing instability while for the stable orbits the sum $\lambda_{\text{s}} + \lambda_{\text{s}}^{-1}$ shrinks for increasing n_{eff}. The sum thereby remains between -2 and 2 what means that these orbits do not become unstable. When taking a close look at the curves one can see that the second derivative of $\lambda_{\text{u}} + \lambda_{\text{u}}^{-1}$ is positive for low n_{eff} and becomes negative for high n_{eff}. This indicates the hypothesis that the stability eigenvalues might saturate at some point but it would need a wider range of n_{eff} for testing it. Furthermore, a closer look at the $M_1 = 7$ orbits reveals that they split up into a stable and unstable orbit for high n_{eff}. Though the splitting is small this indicates that for high n_{eff} more tori break up.

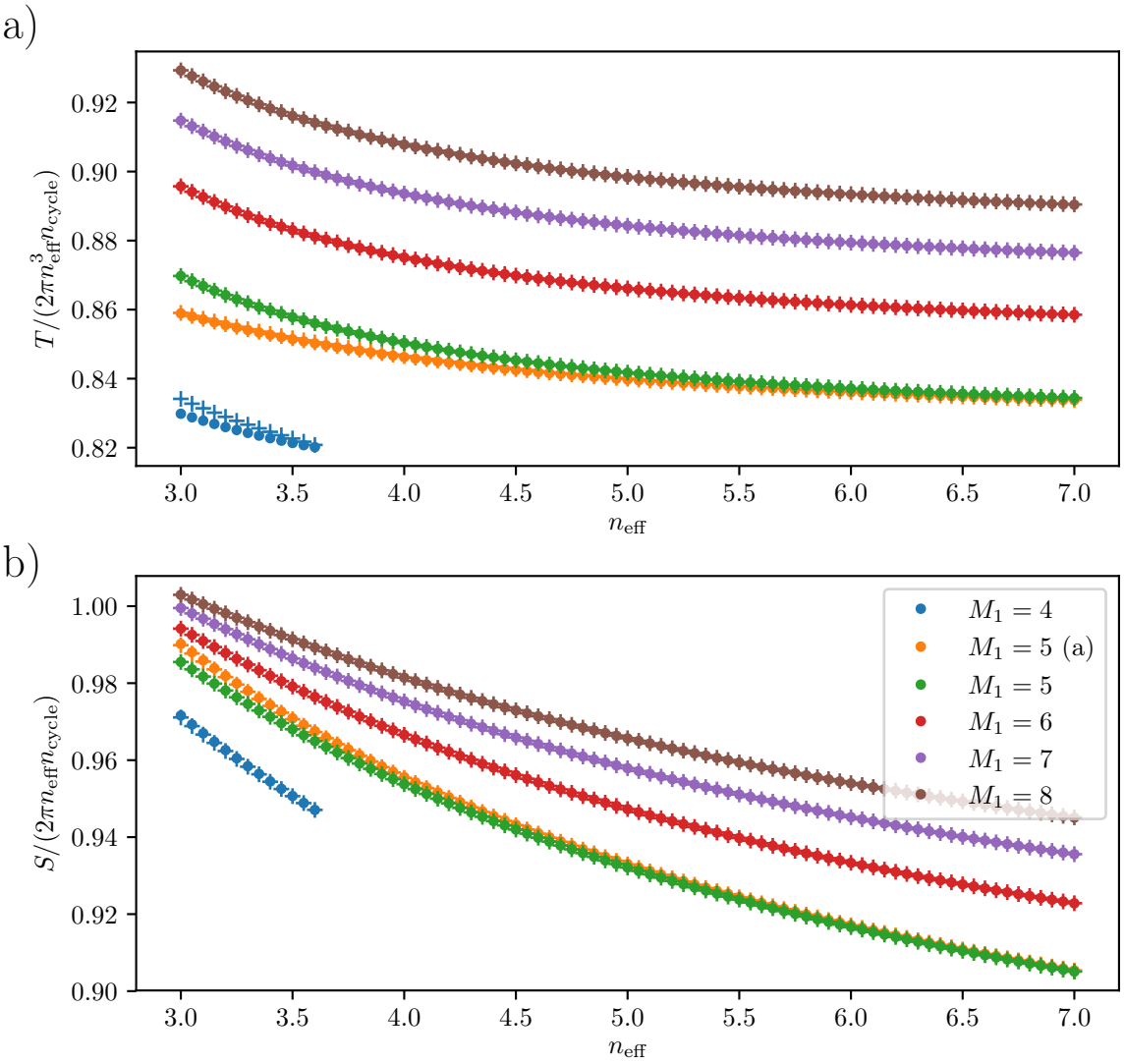

Figure 3.13: Figure a) shows the time period and figure b) the action in dependence of n_{eff}. The stable and unstable orbit have almost the same period except for $M_1 = 4$. For high n_{eff} the curves seem to converge. The action on the other hand does not saturate for high n_{eff} but it is likely that it does for even higher n_{eff} outside the simulated range because the second derivative is positive. The action of both $M_1 = 4$ orbits seems to be similar too which was not the case for the period.

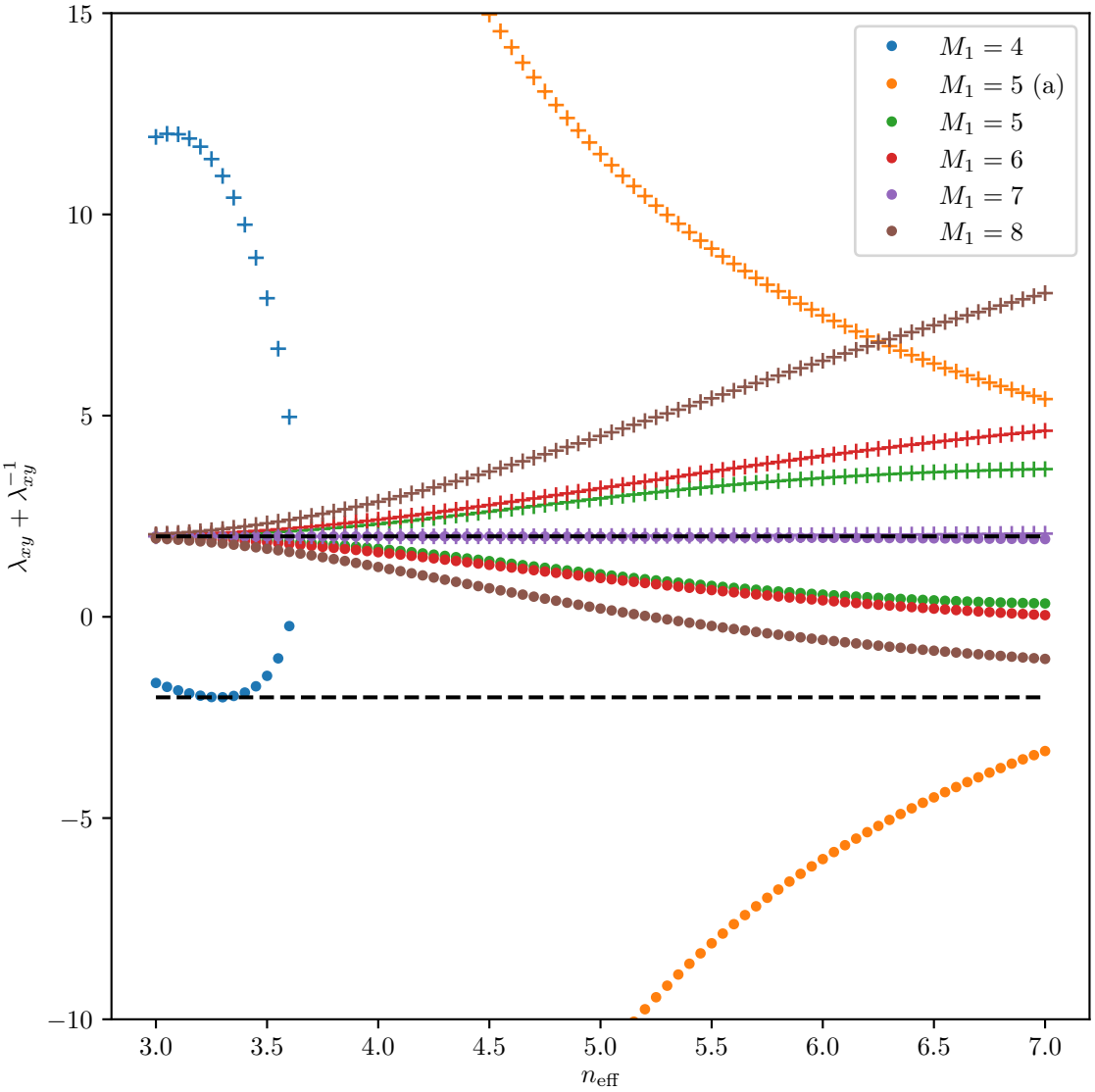

Figure 3.14: The figure shows the stability eigenvalues of orbits with low M_1 and $M_2 = 1$ for varying n_{eff}. The dots represent the stable orbits while the crosses represent their unstable partners. All pairs except $M_1 = 4$ and $M_1 = 5$ (a) show the same behavior. The instability of the unstable orbit increases with increasing n_{eff} while the stable orbit remains stable since the sum of the eigenvalues remains between -2 and 2. For the $M_1 = 4$ orbits it is the other way around. The orbit seems to be generated in a tangent bifurcation somewhere between $n_{\text{eff}} = 3.6$ and 3.65 and the eigenvalues difference from one increases with decreasing n_{eff}. The other exception is the orbit pair $M_1 = 5$ (a) which provides two highly unstable orbits which nevertheless share some common properties as their eigenvalues seem to scale similarly. Note that the curves continue like this outside the visible range ($\lambda_{xy} + \lambda_{xy}^{-1} \in [-10, 15]$).

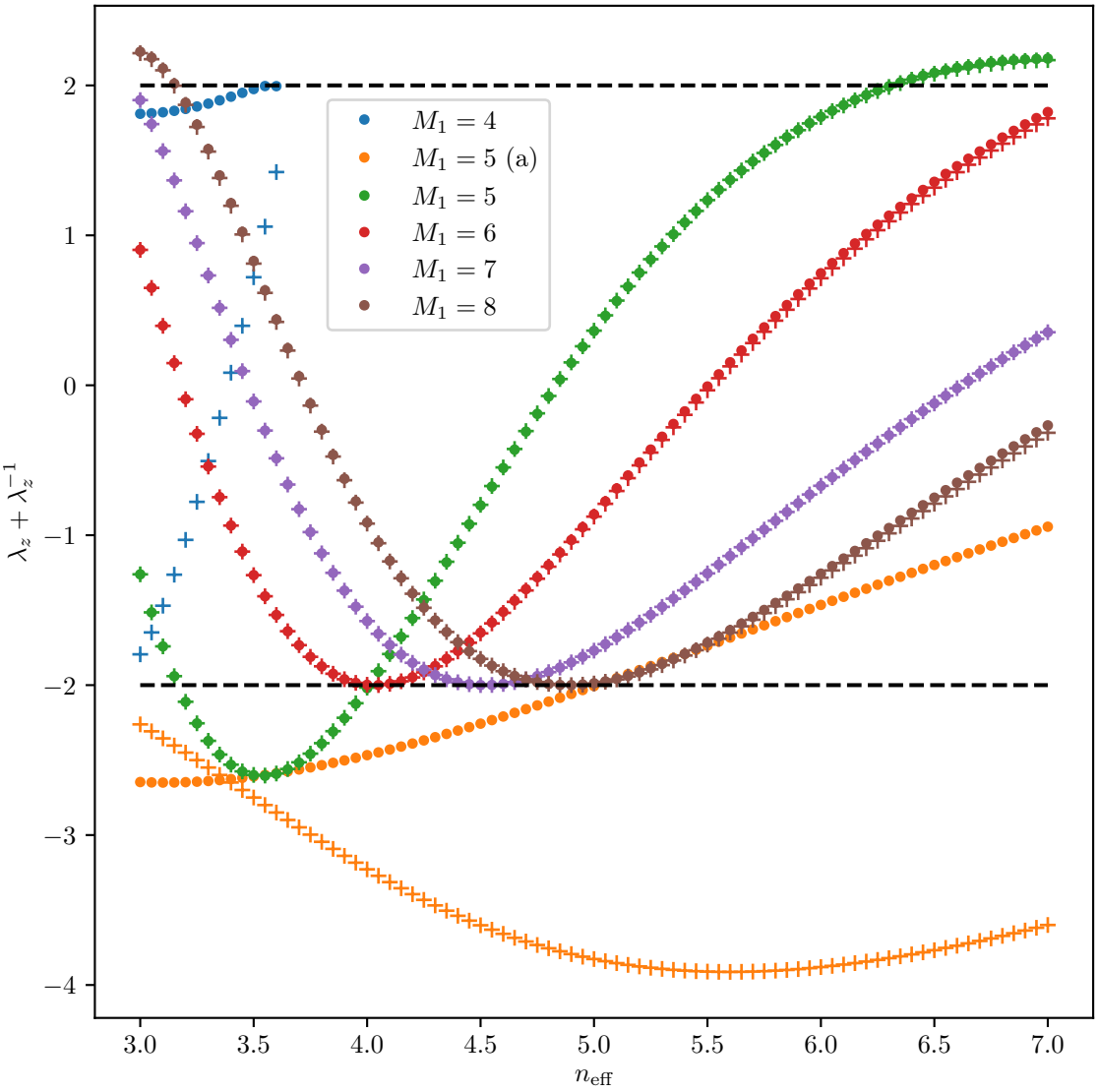

Figure 3.15: The dots represent the stable orbits while the crosses represent the unstable orbits. For both orbits of a pair the stability out of the plane of symmetry is almost the same except for high n_{eff} where small deviations occur. There are two exceptions which are explained later. The regular orbits have smooth curves which are different for each pair but exhibit some similarities, for example they all have a minimum. This minimum shifts towards higher n_{eff} for higher M_1. Some of the curves leave the stable region between -2 and 2 somewhere but $M_1 = 5$ is the only orbit pair where the minimum is below -2 while it seems to be exactly -2 for the other pairs.
The orbits with $M_1 = 4$ differ strongly but have nevertheless some similarities as their stability eigenvalues λ_z approximate one at the bifurcation point. The $M_1 = 5$ (a) orbits do not show a similar behavior. While one of them is always unstable in z-direction the other one becomes stable for high n_{eff}.

The orbits with $M_1 = 4$ behave the other way around. Their eigenvalues approximate one as n_{eff} increases. When they reach it somewhere between $n_{\text{eff}} = 3.6$ and 3.65 the orbit pair disappears in a tangent bifurcation which was mentioned before. Furthermore, for very low n_{eff} the eigenvalues distance from one shrinks slightly which means that there is a maximum respectively a minimum in the curves. The chaotic $M_1 = 5$ (a) orbits are both unstable and their instability increases strongly with decreasing n_{eff}.

Figure 3.15 shows the stability eigenvalue out of the plane of symmetry. It turns out that this eigenvalue is about the same for the stable and unstable partner unless for high n_{eff} where small deviations appear. In general the sum of the stability eigenvalues of each regular orbit pair has a minimum shifting to higher n_{eff} for increasing M_1. Except for $M_1 = 5$, all regular orbits have their minimum at $\lambda_z + \lambda_z^{-1} = -2$. For $M_1 = 5$ the minimum is below -2 which means that the orbit becomes unstable in z-direction here. In addition, two of the curves show unstable regions where the absolute of the sum becomes larger than two and the orbit therefore unstable but because of the general trends it is likely that the other pairs also show such unstable regions but outside the investigated range.

Again the pair with $M_1 = 4$ shows a different behavior because the eigenvalues of the both orbits are not the same. This might be explained by the PSOS in figure 3.11 where one can see that the fixed points of both orbits are located in different regions because their torus deforms strongly. This can cause different stability properties for both orbits. The stability becomes similar at the bifurcation point since both orbits become identical here. Also the eigenvalues of $M_1 = 5$ (a) orbits do not fit together at all.

All in all, it seems to be possible to interpolate the orbits' action, period and stability eigenvalues for arbitrary n_{eff} in the investigated range because they form smooth curves. An example for this is given in appendix F. Although this interpolation may become important when calculating the density of states in dependence of n_{eff} it is not possible to extrapolate the curves to higher n_{eff}. Unfortunately it is also not possible to tell anything about the other orbits with higher M_1 so there is a lot of work left to do finding at least all $M_2 = 1$ orbits in a wide range of n_{eff}. Like described in section 3.1 it might be possible to derive the parameters of most of the other orbits from them.

4 Conclusion and Outlook

In this thesis we investigated the classical dynamics of excitons in cuprous oxide in the symmetry plane of the crystal orthogonal to the [001] axis for a fixed effective quantum number $n_{\mathrm{eff}} = 5$. Two-dimensional classical orbits occur in this plane because of the cubic O_{h} symmetry of the crystal. We accounted for the band structure of cuprous oxide by introducing a quasispin interacting with the hole spin where we treated the spin dynamics quantum mechanically by using an adiabatic approach. A Poincaré surface of section showed that there is one central fixed point which is stable and isolated, it belongs to the shortest periodic orbit. According to the Poincaré-Birkhoff theorem we expected the surrounding tori to break up leaving pairs of a stable and an unstable partner orbit but it turned out that both partner orbits are stable except for a few orbit pairs with small angular momentum. Furthermore, we investigated the period, action and stability properties of these periodic orbits and used them to calculate the frequencies and amplitudes of the scaled energy spectrum by using semiclassical trace formulas. Comparing the frequencies to a quantum mechanical equivalent revealed a similar behavior although the spectra are not yet comparable quantitatively.

Future work should focus on improving both the semiclassical and the quantum mechanical spectrum. In the semiclassical case one needs to take into account orbits in the chaotic region and from the distinct symmetry plane so as three-dimensional orbits in order to get a complete spectrum. In the quantum mechanical case the accuracy of the frequencies and amplitudes of the spectrum needs to be improved e.g. by using harmonic inversion [33] and the spectrum should be scaled correctly. In addition, one should use exactly the same material parameters for both spectra. Then it becomes possible to compare them quantitatively.

If it succeeds and the semiclassical methods turn out to work one can extend them to other energies and finally one might be able to derive a continuous energy spectrum. In order to do so one can make use of the fact that action, period and the stability out of the plane can be described through smooth curves in dependence of the effective quantum number but also in dependence of the winding numbers which classify the periodic orbits. This makes it possible to extrapolate the parameters of most of the regular periodic orbits at least in the symmetry plane orthogonal to the [001] axis. For three-dimensional periodic orbits it might be more complicated.

A Zusammenfassung in deutscher Sprache

Exzitonen sind atomähnliche Zustände in Halbleitern wie Kupferoxydul (Cu_2O), bestehend aus einem Elektron und einem positiv geladenen Loch. Sie entstehen, indem ein Elektron aus dem Valenz- ins Leitungsband angeregt wird, wo es sich mit dem im Valenzband verbliebenem Loch zu einem wasserstoffartigen, gebundenen Zustand verbindet. Diese Arbeit beschäftigt sich mit Exzitonen der gelben Serie, deren Anregungsenergien Wellenlängen von etwa 590 nm [1] entsprechen.

Es wurden bereits Untersuchungen zu Exzitonen in Kupferoxydul durchgeführt, sowohl experimentell [1–3], als auch mit quantenmechanischen Rechnungen [4, 5]. Diese Untersuchungen zeigen Ähnlichkeiten zum Wasserstoffatom auf, aber auch, dass es durch die Bandstruktur zu Abweichungen kommt. Für das Wasserstoffatom hat sich gezeigt, dass es möglich ist, eine Verbindung zwischen dem quantenmechanischen Energiespektrum und den Kepler-Ellipsen des Bohr-Sommerfeld Modells herzustellen. Das wirft die Frage auf, ob etwas Vergleichbares auch für Exzitonen in Kupferoxydul möglich ist.

Mittels semiklassischer Spurformeln ist es möglich die Fluktuationen in der Zustandsdichte in Relation zu klassischen periodischen Bahnen zu setzen, wobei die Frequenzen durch die Periodendauern oder Wirkungen gegeben sind, während die Amplituden durch die Stabilität der Bahnen bestimmt werden. In dieser Arbeit werden diese semiklassischen Theorien angewandt um die Spektren der Exzitonen zu berechnen und zu interpretieren.

Um die Bandstruktur bei der Berechnung klassischer Bahnen zu berücksichtigen wird eine adiabatische Näherung für Quasispin und Lochspin verwendet. Dabei wird angenommen, dass die Spin-Dynamik viel schneller ist, als die klassische Bewegung, wodurch es möglich wird, die Spin-Freiheitsgrade quantenmechanisch zu behandeln, während die Exzitonenbahnen klassisch gerechnet werden.

Kupferoxydul hat eine kubische O_h Symmetrie. Deshalb gibt es unterschiedliche Symmetrieebenen, in denen zweidimensionale klassische Exzitonenbahnen auftreten. Um das Problem zu vereinfachen werden in dieser Arbeit nur Bahnen in der Symmetrieebene senkrecht zur [001] Achse betrachtet.

In der Arbeit wird die klassische Dynamik der Exzitonen untersucht, indem ein Poincaré-Schnitt erstellt und periodische Bahnen in der Ebene gesucht werden. Für diese Bahnen werden Wirkung, Periodendauer und die Stabilitätseigenschaften bestimmt, welche anschließend für semiklassische Berechnungen verwendet werden.

B Material parameters of cuprous oxide

The following table lists the parameters for cuprous oxide as they are used in this thesis.

Table B.1: Material parameters of Cu_2O used in this thesis.

parameter	symbol	value	
band gap energy	E_g	2.172 08 eV	[1]
electron mass	m_e	$0.99m_0$	[34]
hole mass	m_h	$0.58m_0$	[34]
dielectric constant	ε	7.5	[35]
spin-orbit coupling	Δ	0.131 eV	[3]
valence band parameters	γ_1	1.76	[3]
	γ_2	0.7532	[3]
	γ_3	-0.3668	[3]
	η_1	-0.02	[3]
	η_2	-0.00367	[3]
	η_3	-0.03367	[3]

C Exciton-Hartree units

For the hydrogen system it is usual to use Hartree units defined by setting

$$e = m_0 = \hbar = \frac{1}{4\pi\varepsilon_0} \equiv 1 \tag{C.1}$$

with unit charge e, electron mass m_0, Planck's constant $\hbar$ and vacuum permittivity ε_0. For excitons in cuprous oxide one has to account for the permittivity ε so as the differing effective mass of the electron which is done by setting

$$e = \frac{m_0}{\gamma_1'} = \hbar = \frac{1}{4\pi\varepsilon\varepsilon_0} \equiv 1 \tag{C.2}$$

where $\gamma_1' = 2.77$ and $\varepsilon = 7.5$. The unit of length a_{exc} and the energy unit E_{exc} change to

$$a_{\mathrm{exc}} = \frac{4\pi\varepsilon\varepsilon_0\hbar^2\gamma_1'}{e^2 m_0}, \qquad E_{\mathrm{exc}} = \frac{\hbar^2\gamma_1'}{a_{\mathrm{exc}}^2 m_0}. \tag{C.3}$$

The most important quantities so as their conversion to SI units are listed in table C.1.

Table C.1: Exciton-Hartree units and conversion to SI units for the most important quantities. It is $\gamma_1' = 2.77$ and $\varepsilon = 7.5$. For the hydrogenlike case it would be $\gamma_1' = \varepsilon = 1$.

quantity	symbol	unit	SI
charge	q	e	$1.602 \times 10^{-19}\,\mathrm{C}$
mass	m	$m_0\gamma_1'^{-1}$	$3.228 \times 10^{-31}\,\mathrm{kg}$
angular momentum	L	$\hbar$	$1.055 \times 10^{-34}\,\mathrm{J\,s}$
length	r	a_{exc}	$1.099 \times 10^{-9}\,\mathrm{m}$
momentum	p	$\hbar a_{\mathrm{exc}}^{-1}$	$9.593 \times 10^{-26}\,\mathrm{kg\,m\,s^{-1}}$
energy	E	E_{exc}	$1.399 \times 10^{-20}\,\mathrm{J}$
time	t	$\hbar E_{\mathrm{exc}}^{-1}$	$3.769 \times 10^{-15}\,\mathrm{s}$
action	S	$\hbar$	$1.055 \times 10^{-34}\,\mathrm{J\,s}$

D Summary of periodic orbits

This appendix contains images of all regular periodic orbits with $M_2 = 1$ at $n_{\text{eff}} = 5$.

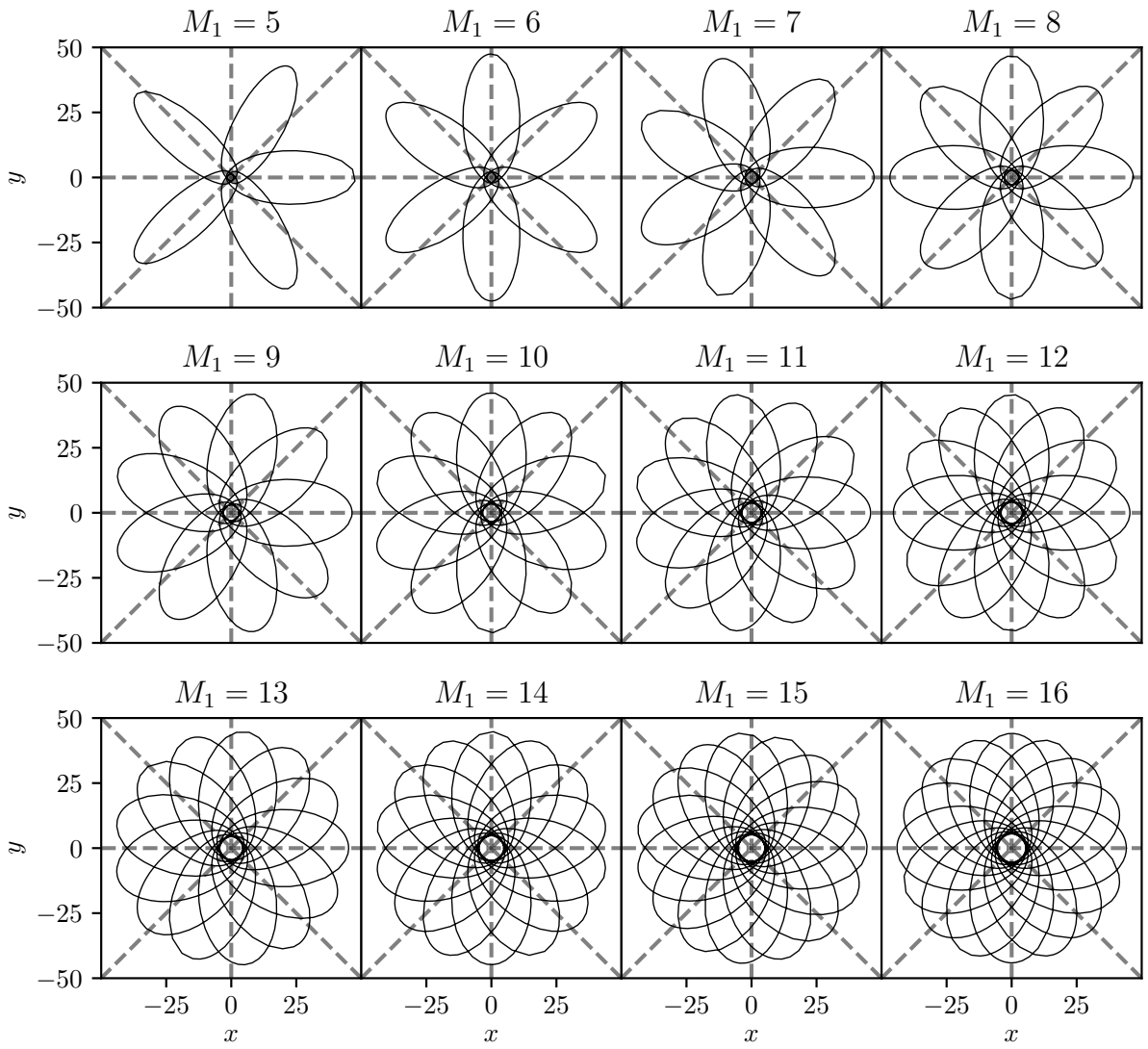

Figure D.1: Stable periodic orbits for $M_2 = 1$ at $n_{\text{eff}} = 5$, part 1.

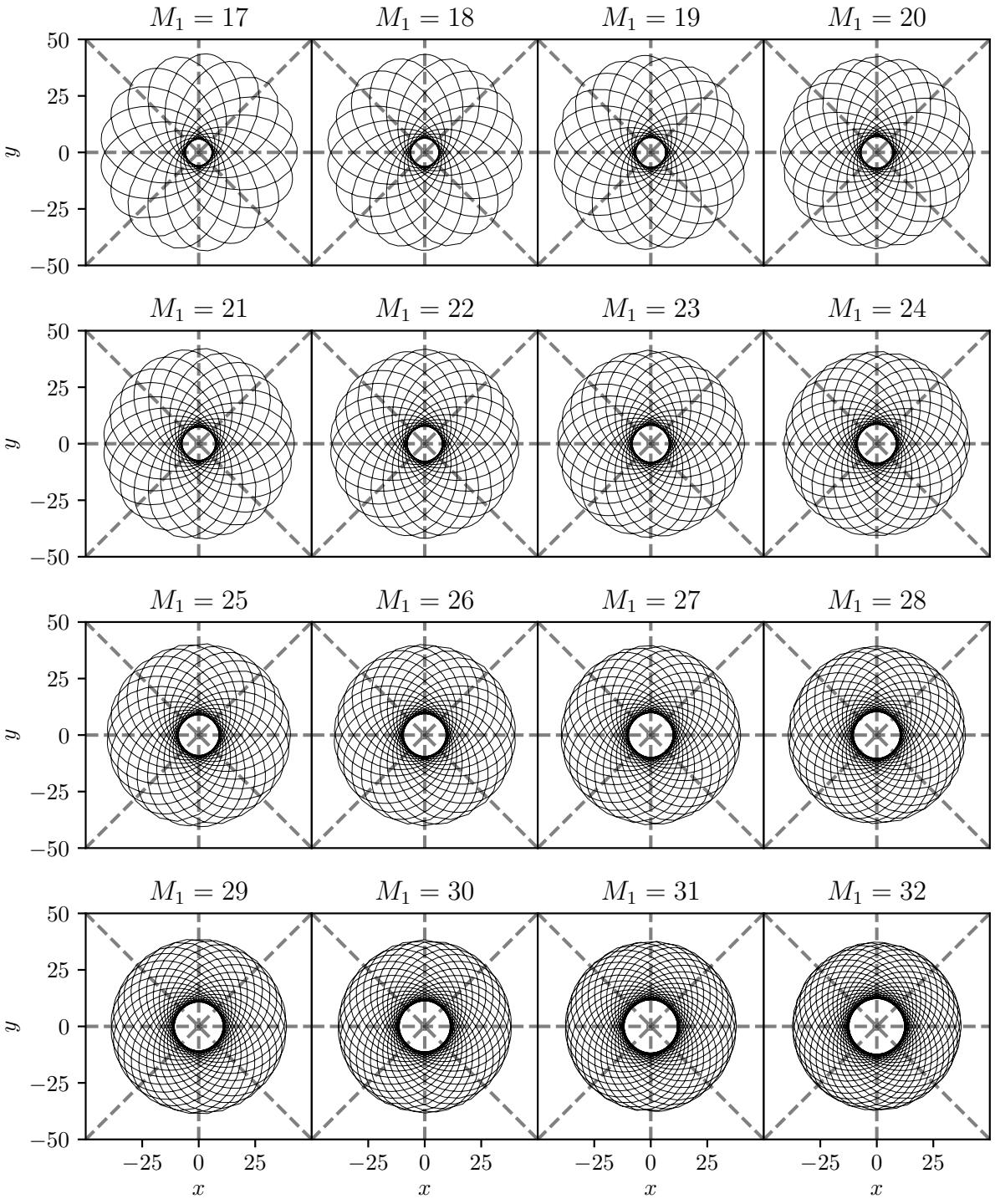

Figure D.2: Stable periodic orbits for $M_2 = 1$ at $n_{\text{eff}} = 5$, part 2.

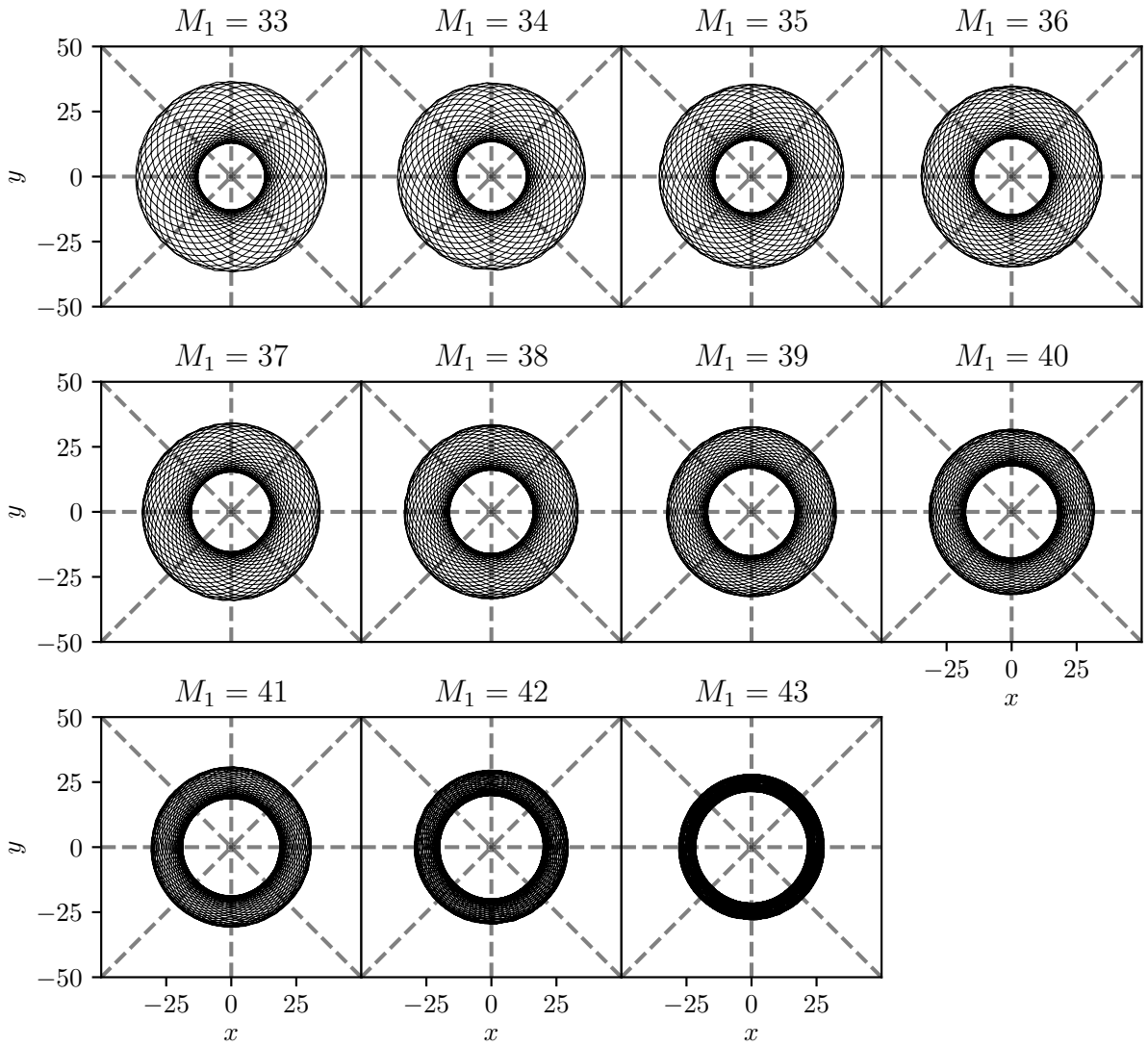

Figure D.3: Stable periodic orbits for $M_2 = 1$ at $n_{\text{eff}} = 5$, part 3.

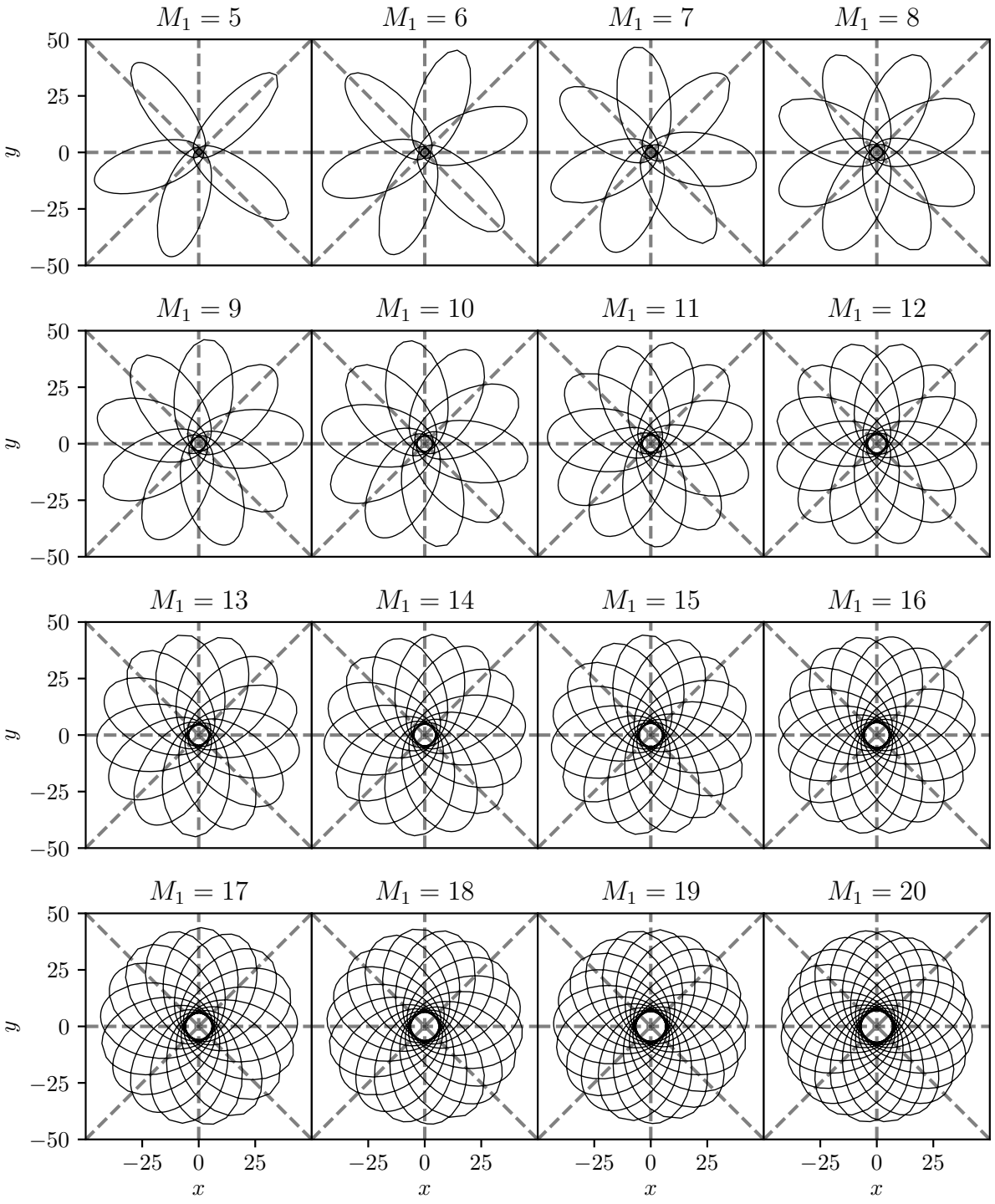

Figure D.4: Unstable periodic orbits for $M_2 = 1$ at $n_{\text{eff}} = 5$, part 1.

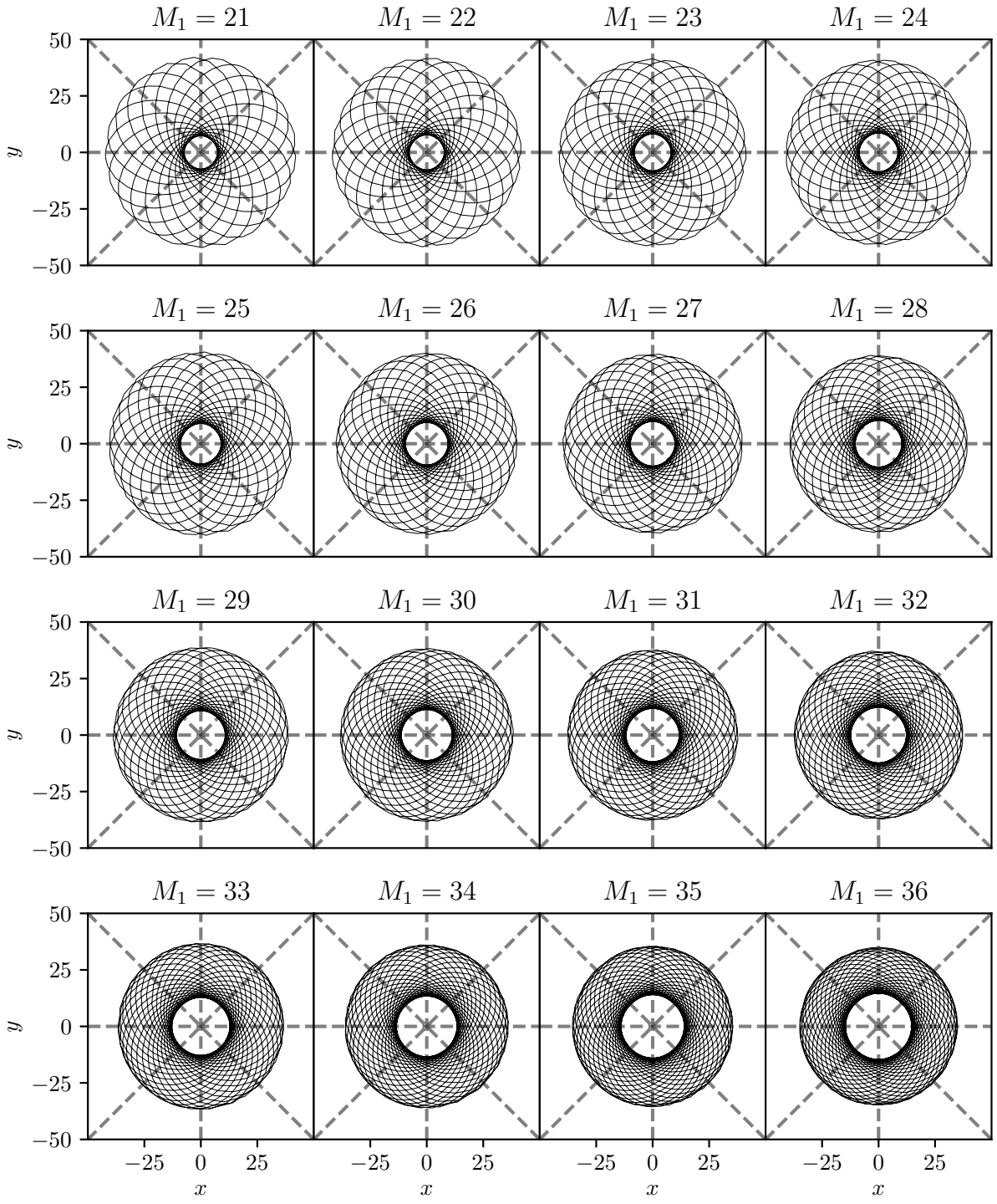

Figure D.5: Unstable periodic orbits for $M_2 = 1$ at $n_{\text{eff}} = 5$, part 2.

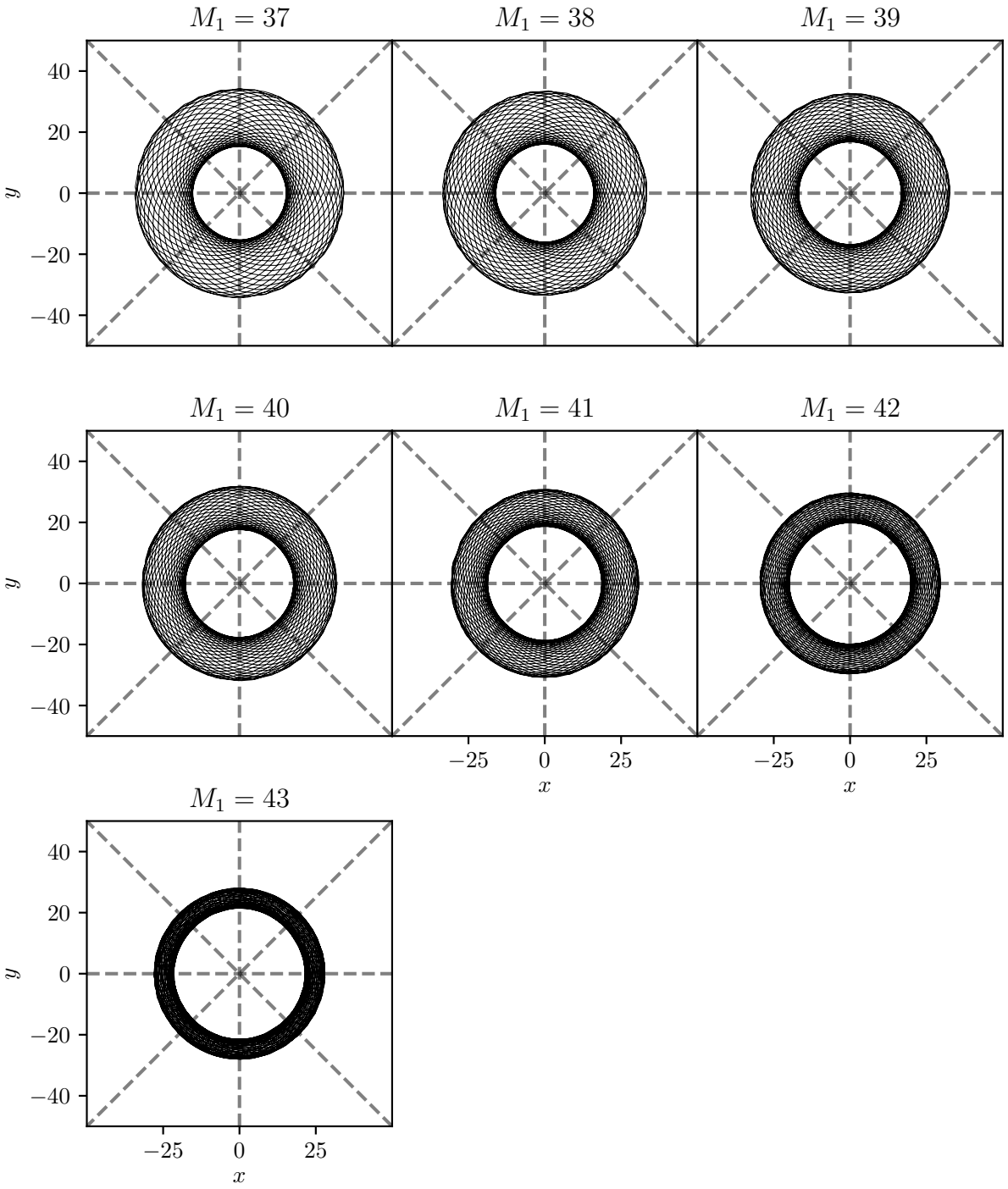

Figure D.6: Unstable periodic orbits for $M_2 = 1$ at $n_{\text{eff}} = 5$, part 3.

E Sorting of the stability eigenvectors

As mentioned in the results the stability eigenvalues of the periodic orbits are sorted corresponding to the direction of their eigenvectors. The stability matrix is an 8×8 matrix in KS coordinates which makes the interpretation of the resulting eigenvectors being not quite intuitive. In this appendix it will be shown how the eigenvalues are sorted and how the eigenvectors can be interpreted.

In order to investigate the meaning of the eigenvectors they are transformed into real space coordinates using the representation

$$U = \begin{pmatrix} \sqrt{2r}\cos\left(\frac{\theta}{2}\right)\cos\left(\frac{\varphi+\alpha}{2}\right) \\ \sqrt{2r}\cos\left(\frac{\theta}{2}\right)\sin\left(\frac{\varphi+\alpha}{2}\right) \\ \sqrt{2r}\sin\left(\frac{\theta}{2}\right)\cos\left(\frac{\varphi-\alpha}{2}\right) \\ \sqrt{2r}\sin\left(\frac{\theta}{2}\right)\sin\left(\frac{\varphi-\alpha}{2}\right) \end{pmatrix}. \tag{E.1}$$

The unit vectors into the direction of the corresponding variables read

$$\hat{e}_r = \text{normalized}\left(\partial_r \boldsymbol{U}\right) = \begin{pmatrix} \cos\left(\frac{\theta}{2}\right)\cos\left(\frac{\varphi+\alpha}{2}\right) \\ \cos\left(\frac{\theta}{2}\right)\sin\left(\frac{\varphi+\alpha}{2}\right) \\ \sin\left(\frac{\theta}{2}\right)\cos\left(\frac{\varphi-\alpha}{2}\right) \\ \sin\left(\frac{\theta}{2}\right)\sin\left(\frac{\varphi-\alpha}{2}\right) \end{pmatrix}, \tag{E.2}$$

$$\hat{e}_\varphi = \text{normalized}\left(\partial_\varphi \boldsymbol{U}\right) = \begin{pmatrix} -\cos\left(\frac{\theta}{2}\right)\sin\left(\frac{\varphi+\alpha}{2}\right) \\ \cos\left(\frac{\theta}{2}\right)\cos\left(\frac{\varphi+\alpha}{2}\right) \\ -\sin\left(\frac{\theta}{2}\right)\sin\left(\frac{\varphi-\alpha}{2}\right) \\ \sin\left(\frac{\theta}{2}\right)\cos\left(\frac{\varphi-\alpha}{2}\right) \end{pmatrix}, \tag{E.3}$$

$$\hat{e}_\theta = \text{normalized}\left(\partial_\theta \boldsymbol{U}\right) = \begin{pmatrix} -\sin\left(\frac{\theta}{2}\right)\cos\left(\frac{\varphi+\alpha}{2}\right) \\ -\sin\left(\frac{\theta}{2}\right)\sin\left(\frac{\varphi+\alpha}{2}\right) \\ \cos\left(\frac{\theta}{2}\right)\cos\left(\frac{\varphi-\alpha}{2}\right) \\ \cos\left(\frac{\theta}{2}\right)\sin\left(\frac{\varphi-\alpha}{2}\right) \end{pmatrix}, \tag{E.4}$$

$$\hat{e}_\alpha = \text{normalized}\left(\partial_\alpha \boldsymbol{U}\right) = \begin{pmatrix} -\cos\left(\frac{\theta}{2}\right)\sin\left(\frac{\varphi+\alpha}{2}\right) \\ \cos\left(\frac{\theta}{2}\right)\cos\left(\frac{\varphi+\alpha}{2}\right) \\ \sin\left(\frac{\theta}{2}\right)\sin\left(\frac{\varphi-\alpha}{2}\right) \\ -\sin\left(\frac{\theta}{2}\right)\cos\left(\frac{\varphi-\alpha}{2}\right) \end{pmatrix}. \tag{E.5}$$

Unfortunately the unit vectors $\hat{e}_\varphi$ and $\hat{e}_\alpha$ are not orthogonal which means that they cannot be used both in an orthonormal transformation. The solution is to replace $\hat{e}_\alpha$ with the orthogonal vector

$$\hat{e}_\perp = \begin{pmatrix} -\sin\left(\frac{\theta}{2}\right)\sin\left(\frac{\varphi+\alpha}{2}\right) \\ \sin\left(\frac{\theta}{2}\right)\cos\left(\frac{\varphi+\alpha}{2}\right) \\ \cos\left(\frac{\theta}{2}\right)\sin\left(\frac{\varphi-\alpha}{2}\right) \\ -\cos\left(\frac{\theta}{2}\right)\cos\left(\frac{\varphi-\alpha}{2}\right) \end{pmatrix}. \tag{E.6}$$

The stability matrix can now be transformed as $\boldsymbol{M}^{(1)} = \boldsymbol{T}^\intercal \boldsymbol{M} \boldsymbol{T}$ with

$$\boldsymbol{T} = \begin{pmatrix} \hat{e}_r & \hat{e}_\varphi & \hat{e}_\theta & \hat{e}_\perp & \mathbf{0} & \mathbf{0} & \mathbf{0} & \mathbf{0} \\ \mathbf{0} & \mathbf{0} & \mathbf{0} & \mathbf{0} & \hat{e}_r & \hat{e}_\varphi & \hat{e}_\theta & \hat{e}_\perp \end{pmatrix}. \tag{E.7}$$

Such a transformation changes the eigenvectors $\boldsymbol{\Lambda}_i$ but not the eigenvalues λ_i because of

$$\begin{aligned} \boldsymbol{M}^{(1)}\boldsymbol{\Lambda}_i^{(1)} &= \boldsymbol{T}^\intercal \boldsymbol{M} \boldsymbol{T} \boldsymbol{T}^\intercal \boldsymbol{\Lambda}_i \\ &= \boldsymbol{T}^\intercal \boldsymbol{M} \boldsymbol{\Lambda}_i \\ &= \lambda_i \boldsymbol{T}^\intercal \boldsymbol{\Lambda}_i \\ &= \lambda_i \boldsymbol{\Lambda}_i^{(1)} \end{aligned} \tag{E.8}$$

with transformed eigenvector $\boldsymbol{\Lambda}_i^{(1)}$.

The following example shows the eigenvalues and eigenvectors of the stable $M_1 = 5$, $M_2 = 1$ orbit at $n_{\text{eff}} = 5$. The two eigenvalue pairs which are different from one belong to

$$\lambda_i = \qquad 0.5285 \pm 0.8489\mathrm{i}, \qquad\qquad 0.1809 \pm 0.9835\mathrm{i} \tag{E.9}$$

$$\boldsymbol{\Lambda}_i = \begin{pmatrix} -0.699 \\ 0 \\ 0 \\ 0 \\ 0 \\ 0.313 \\ 0 \\ 0 \end{pmatrix} \pm \mathrm{i} \begin{pmatrix} 0 \\ 0.319 \\ 0 \\ 0 \\ 0.557 \\ 0 \\ 0 \\ 0 \end{pmatrix}, \qquad \begin{pmatrix} 0 \\ 0 \\ 0 \\ 0.701 \\ 0 \\ 0 \\ -0.529 \\ 0 \end{pmatrix} \pm \mathrm{i} \begin{pmatrix} 0 \\ 0 \\ -0.238 \\ 0 \\ 0 \\ 0 \\ 0 \\ -0.416 \end{pmatrix} \tag{E.10}$$

and the four eigenvalues close to one are

$$\lambda_i = \quad 1.0052, \quad 0.9948, \quad 1.0000 \pm 0\mathrm{i} \tag{E.11}$$

$$\mathbf{\Lambda}_i = \begin{pmatrix} 0 \\ 0 \\ 0 \\ 0.497 \\ 0 \\ 0 \\ 0.867 \\ 0 \end{pmatrix}, \quad \begin{pmatrix} 0 \\ 0 \\ 0 \\ 0.497 \\ 0 \\ 0 \\ 0.867 \\ 0 \end{pmatrix}, \quad \begin{pmatrix} 0.010 \\ 0.871 \\ 0 \\ -0.026 \\ -0.392 \\ 0.018 \\ -0.045 \\ 0 \end{pmatrix} \pm \mathrm{i} \begin{pmatrix} 0.073 \\ 0 \\ 0 \\ 0.123 \\ 0 \\ 0.128 \\ 0.216 \\ 0 \end{pmatrix}. \tag{E.12}$$

The coordinates in which the eigenvectors are given are $(\hat{e}_r, \hat{e}_\varphi, \hat{e}_\theta, \hat{e}_\perp)^\intercal$ (for position and momentum) which equals $(\hat{e}_r, \hat{e}_\varphi, \hat{e}_z, \hat{e}_\perp)^\intercal$ because the orbits remain in the $z = 0$ plane. Note that the zero components are not necessarily exact zero but only smaller than 0.001.

As one can see the eigenvectors are not all orthogonal and in some cases they are almost degenerate. For the both first eigenvectors in (E.12) there are only differences in the small components which are set to zero here. The stability matrix can therefore actually not be diagonalized but only brought to a Jordan normal form. This in fact does not change the case that one can calculate the trace as product of the eigenvalues and does therefore not affect our semiclassical calculations.

The other orbits (at least at $n_{\mathrm{eff}} = 5$) have quite similar eigenvectors which allows for sorting them. The eigenvectors of other orbits have the same components being unequal zero and having identical signs. The absolute of the components on the other hand changes strongly.

The first eigenvalue pair belongs to a movement in the xy-plane and can therefor be assigned to the actual stability inside the plane. The second eigenvalue pair has components in z-direction but also in the direction of the orthogonal unit vector. This unit vector has only limited physical meaning and the eigenvalue must therefore be connected to the stability out of the plane.

The other four eigenvalues are close to one but it was expected that they are strictly one because of conserved quantities. For varying simulation parameters the eigenvalues are sometimes real and sometimes complex what indicates that it is only a numerical artifact. Nevertheless, investigations showed that other orbits also have the same systematic. There is one eigenvalue pair very close to one having eigenvectors similar to the last eigenvector and one pair which is not that close to one and has two almost identical eigenvectors.

The general trend is that with increasing M_1/M_2 the difference of the eigenvalues in xy-direction to one shrinks and in consequence the eigenvectors start to mix since there are three eigenvalue pairs which are quite close to one. Also some of the small components become bigger (sometimes even dominant). What remains is one eigenvector having almost zero components along x- and y-direction describing the stability in z-direction.

At last let us take a look at the eigenvectors of the unstable partner of the former shown orbit. The xy and z eigenvectors are

$$\lambda_i = \quad 2.5537, \qquad 0.3916, \qquad 1.1824 \pm 0.9832\mathrm{i} \tag{E.13}$$

$$\mathbf{\Lambda}_i = \begin{pmatrix} 0.078 \\ 0.624 \\ 0 \\ 0 \\ 0.776 \\ -0.026 \\ 0 \\ 0 \end{pmatrix}, \quad \begin{pmatrix} -0.078 \\ 0.624 \\ 0 \\ 0 \\ 0.776 \\ 0.026 \\ 0 \\ 0 \end{pmatrix}, \quad \begin{pmatrix} 0 \\ 0 \\ 0.582 \\ 0 \\ 0 \\ 0 \\ 0 \\ 0.657 \end{pmatrix} \pm \mathrm{i} \begin{pmatrix} 0 \\ 0 \\ 0 \\ 0.474 \\ 0 \\ 0 \\ -0.251 \\ 0 \end{pmatrix}. \tag{E.14}$$

The first two eigenvectors are now real and almost identical like it was the case for the third pair from before. They remain in the xy-plane regardless. The eigenvectors for the second pair look different but a complex eigenvector can of course be multiplied with any complex number. When multiplying with $-\mathrm{i}$ one can see that the same components are unequal zero and that they have the same sign.

F Interpolating stability eigenvalues and angles

This appendix explains how the stability eigenvalue λ_z can be interpolated for further orbits with higher M_2.

The eigenvalues λ_z form smooth curves when plotted in dependence of M_1/M_2 as well as in dependence of n_{eff} interrupted only when changing between real and complex eigenvalues. This behavior can be seen in the right graphs of figure F.1. Fortunately the sum $b_z \equiv \lambda_z + \lambda_z^{-1}$ is smooth also at this transition points. This is why we use a fit to b_z instead of λ_z to interpolate values in between. Figure F.1 shows an example for a polynomial fit of tenth order used to approximate the sum for $M_1 = 5$. Using

$$b_z = \lambda_z + \lambda_z^{-1} \tag{F.1}$$

$$0 = \lambda_z^2 - b_z \lambda_z + 1$$

$$\lambda_z, \lambda_z^{-1} = \frac{b_z \pm \sqrt{b_z^2 - 4}}{2}. \tag{F.2}$$

one can calculate the eigenvalues from the real variable b_z without knowledge of any other quantity. In figure F.1 it is shown that the results fit to the simulated data.

Although the square root returns imaginary values in the case of complex eigenvalues one has to be careful when implementing the routine. When calculating the stability exponents ϕ_z one has to make sure that the right eigenvalue is taken for the calculation in order to get the correct sign. The sums $b_z < -2$ between $n_{\text{eff}} = 3$ and 4 are a good example for this. The complex stability angle was defined as

$$\phi_z = \ln(\lambda_z) \tag{F.3}$$

and can take two values in general because one can also use λ_z^{-1}. In this thesis we choose the exponent ϕ_z to have a positive real and imaginary part. In case of the eigenvalue being real and negative the logarithm can still be defined as

$$\phi_z = \ln(\lambda_z) = \ln(-\lambda_z) + \mathrm{i}\pi \tag{F.4}$$

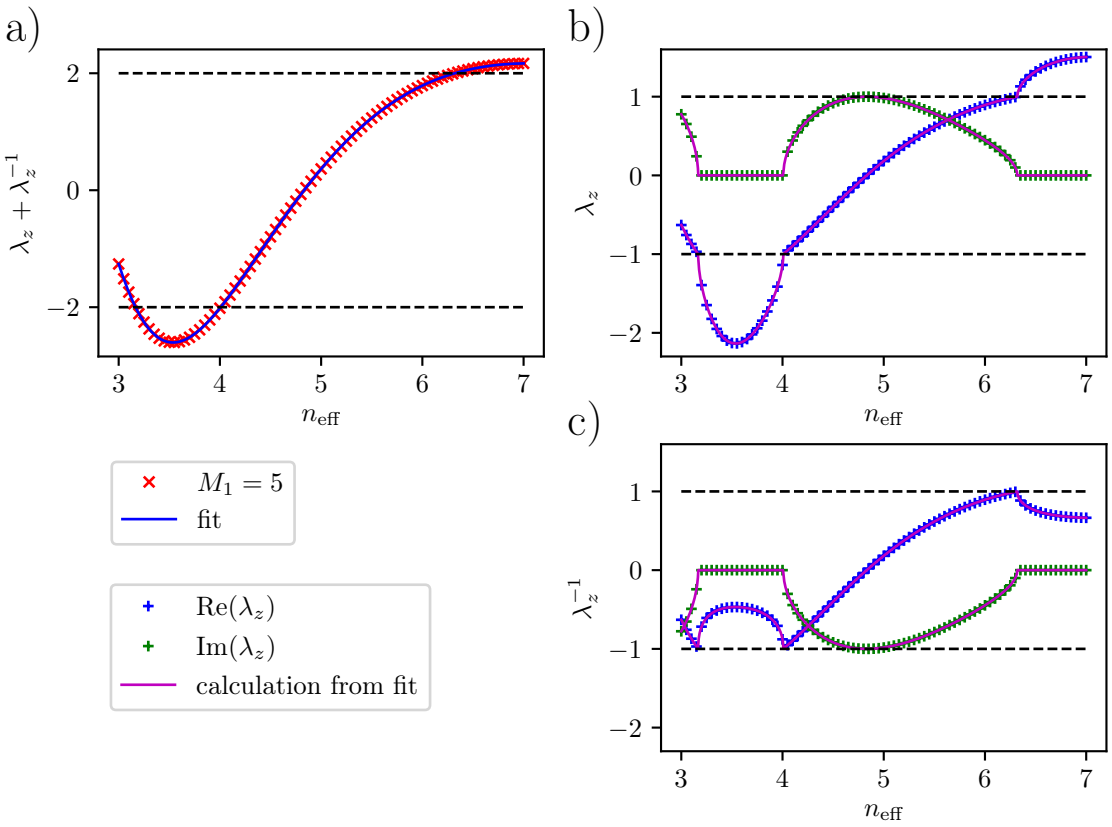

Figure F.1: The eigenvalues λ_z cannot be easily interpolated with a simple fit function because of discontinuities but the sum $\lambda_z + \lambda_z^{-1}$ forms a smooth curve. This appendix explains how λ_z can be calculated by fitting a (tenth order) polynomial to the sum like shown in figure a). The figures b) and c) show that all eigenvalues can be interpolated correctly.

which will return the correct results for $\lambda_z = \exp(\phi_z)$. The angle is defined by the smaller λ_z in that case which has the bigger absolute value.

For the case of fixed n_{eff} it is desired to have a fit to the $M_2 = 1$ orbits, which are most easy to find, and to interpolate all remaining orbits with higher M_2 like shown in figure F.2. In that case λ_z has to be scaled like $\lambda_z^{M_2^{-1}}$ in order to fit in. This is complicated by the fact that $\lambda = \exp(\phi_z) = \exp(u_z + \mathrm{i}v_z)$ is a complex number which means that there are M_2 possible outcomes for $\lambda_z^{M_2^{-1}}$. Fortunately this does not account for the inverse case when calculating λ_z from the interpolated value but it has to be taken into account

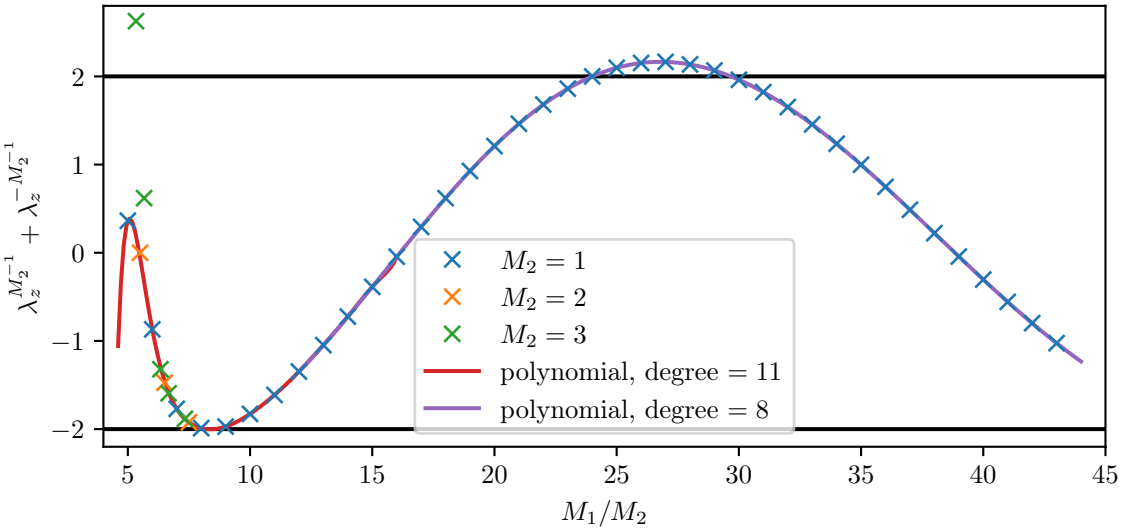

Figure F.2: For the case of varying n_{eff} it seems sufficient to use one polynomial for approximating the whole curve (in the investigated range of n_{eff}). In case of varying M_1/M_2 for fixed $n_{\text{eff}} = 5$ this is not the case any more. In order to reach an acceptable accuracy one needs two polynomials defined on different intervals where the right polynomial can be used for $M_1/M_2 > 14$ the left one for values below. The polynomials are fitted to the $M_2 = 1$ orbits only but they can be used to interpolate for $M_2 > 2$. This works well for all values even between $M_1/M_2 = 24$ and 30 but not for $M_1/M_2 < 6$. In this area the behavior of the eigenvalues seems chaotic which may be explained by the orbits being near the chaotic region. Note that the left $M_2 = 2$ orbit ($M_1 = 11$) seems to fit on the curve but that there is a special case here, namely the case of $\lambda_z < 0$ which makes it impossible to calculate the eigenvalue from the sum.

when comparing the data. The sum can be written as

$$\begin{aligned} b_z^{(M_2)} &= \lambda_z^{M_2^{-1}} + \lambda_z^{-M_2^{-1}} \\ &= \exp(\phi_z + \mathrm{i}2\pi n)^{M_2^{-1}} + \exp(-\phi_z - \mathrm{i}2\pi n)^{M_2^{-1}} \\ &= \cosh\left(\frac{1}{M_2}\left(\phi_z + \mathrm{i}2\pi n\right)\right) \end{aligned} \tag{F.5}$$

with $n \in \mathbb{N}$. Unfortunately there is one case where it becomes impossible to interpolate the correct λ_z namely when $\lambda_z < 0$ and $M_2 = 2n$. For example at $M_2 = 2$ the sum becomes

$$\begin{aligned} b_z^{(M_2=2)} &= \cosh\left(\frac{1}{2}\left(u_z + \mathrm{i}\pi\right)\right) \\ &= \mathrm{i}\exp\left(\frac{u_z}{2}\right) - \mathrm{i}\exp\left(-\frac{u_z}{2}\right) \end{aligned} \tag{F.6}$$

which has a zero real but a non-zero imaginary part which cannot be interpolated from the real function $b_z(M_1/M_2)$. As one can see in the figure this is indeed the case for one orbit with $M_2 = 2$ and $M_1 = 11$. Furthermore, there are some additional data points below $M_1/M_2 = 6$ which do not fit on the curve. The formula can therefore only be used for ratios of $M_1/M_2 >= 6$. This reduces the simulation effort at least to only finding the few shortest orbits of each M_2 one wants to take into account. The remaining orbit's parameters can be interpolated. The corresponding fit parameters are listed in table F.1.

Table F.1: Coefficients of the polynomials fitted to $b_z^{(M_2)} = \lambda_z^{M_2^{-1}} + \lambda_z^{-M_2^{-1}}$ in figure F.2.

quantity	coefficients		range
$b_z^{(M_2)}(M_1/M_2)$	$+7.693\,839\,127\,239\,867\,5 \times 10^{-8}$	x^{11}	$M_1/M_2 \in [6, 14]$
	$-9.186\,641\,565\,038\,194\,6 \times 10^{-6}$	x^{10}	
	$+4.938\,881\,811\,090\,857\,9 \times 10^{-4}$	x^9	
	$-1.577\,561\,237\,372\,266\,5 \times 10^{-2}$	x^8	
	$+3.325\,283\,562\,079\,463\,0 \times 10^{-1}$	x^7	
	$-4.854\,798\,428\,543\,735\,3$	x^6	
	$+5.007\,163\,170\,078\,514\,7 \times 10^{1}$	x^5	
	$-3.646\,383\,540\,718\,250\,1 \times 10^{2}$	x^4	
	$+1.836\,247\,800\,480\,701\,5 \times 10^{3}$	x^3	
	$-6.084\,812\,064\,352\,566\,3 \times 10^{3}$	x^2	
	$+1.192\,730\,177\,269\,112\,4 \times 10^{4}$	x	
	$-1.046\,056\,944\,897\,752\,1 \times 10^{4}$		
$b_z^{(M_2)}(M_1/M_2)$	$-1.569\,782\,680\,533\,240\,3 \times 10^{-12}$	x^8	$M_1/M_2 \in [14, 43]$
	$+7.697\,300\,561\,474\,088\,3 \times 10^{-10}$	x^7	
	$-1.245\,738\,808\,102\,300\,8 \times 10^{-7}$	x^6	
	$+9.482\,303\,688\,053\,998\,0 \times 10^{-6}$	x^5	
	$-3.592\,124\,888\,364\,810\,3 \times 10^{-4}$	x^4	
	$+5.895\,561\,430\,732\,325\,4 \times 10^{-3}$	x^3	
	$-1.529\,068\,958\,184\,019\,9 \times 10^{-2}$	x^2	
	$-2.224\,374\,669\,141\,482\,3 \times 10^{-1}$	x	
	$-1.231\,146\,593\,157\,067\,8$		

G Calculation of the action variables

This appendix explains how the action variables J_1 and J_2 are calculated in this thesis. They are connected to the action by

$$S = 2\pi M_1 J_1 + 2\pi M_2 J_2. \tag{G.1}$$

In order to calculate J_1 one can use the derivative

$$\frac{\partial S}{\partial M_1} = 2\pi J_1 \tag{G.2}$$

which is calculated numerically from the action of the orbits with $M_2 = 1$. In order to get reliable results the numerical derivative is done using two different ways. The first is a simple two point derivative interpolating the value between two neighboring data points with

$$\frac{\partial S}{\partial M_1}\left(\frac{M_{1,i} + M_{1,i+1}}{2}\right) = \frac{S_{i+1} - S_i}{M_{1,i+1} - M_{1,i}}. \tag{G.3}$$

The second way is to use the analytic derivative of a polynomial fit to $S(M_1)$. Figure G.1 shows the accuracy of the fit polynomial in dependence of the polynomial degree. Thereby a degree of 14 seems to be sufficient but a degree of 15 leads to better results in the derivative especially for the extrapolation of values outside the fitting range. The final fit curve (figure G.2) is now differentiated with respect to M_1 in order to calculate J_1 according to equation (G.2). The second action variable J_2 is calculated by subtracting J_1 from the action S using the fit function so as the derivative. Figure G.3 shows that both ways return the same results. For the calculations in this thesis the derivative of the polynomial is used because it can be used for arbitrary M_1/M_2.

It was mentioned in the thesis that the action is almost the same for the stable and unstable orbit of a pair but in figure G.4 it is proven to be true. It is worth mentioning that this difference is indeed important when calculating g''_E directly from the orbit parameter (equation (3.7)) instead of using the action variables but except for the cases when λ_{xy} is significantly different from one ($M_1 = [5, 6, 8, 12]$) the difference in S is of the order of numerical accuracy and cannot be assumed to be resolved good enough for such calculations.

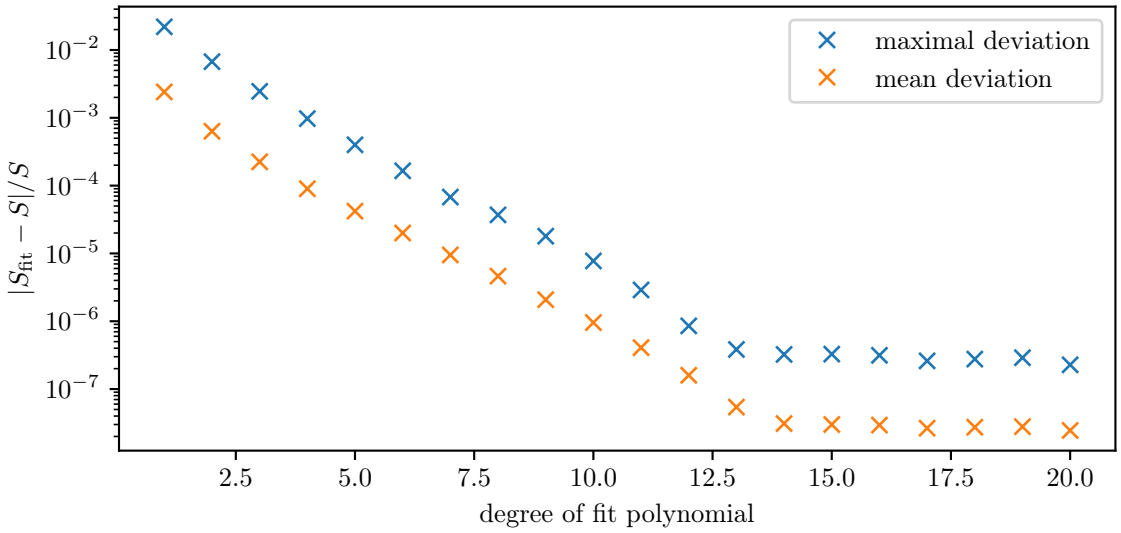

Figure G.1: The accuracy of the polynomial fit to $S(M_1)$ increases with increasing polynomial degree up to a degree of 14 but it turns out that a degree of 15 results in a better behavior at the boundaries of the M_1 range.

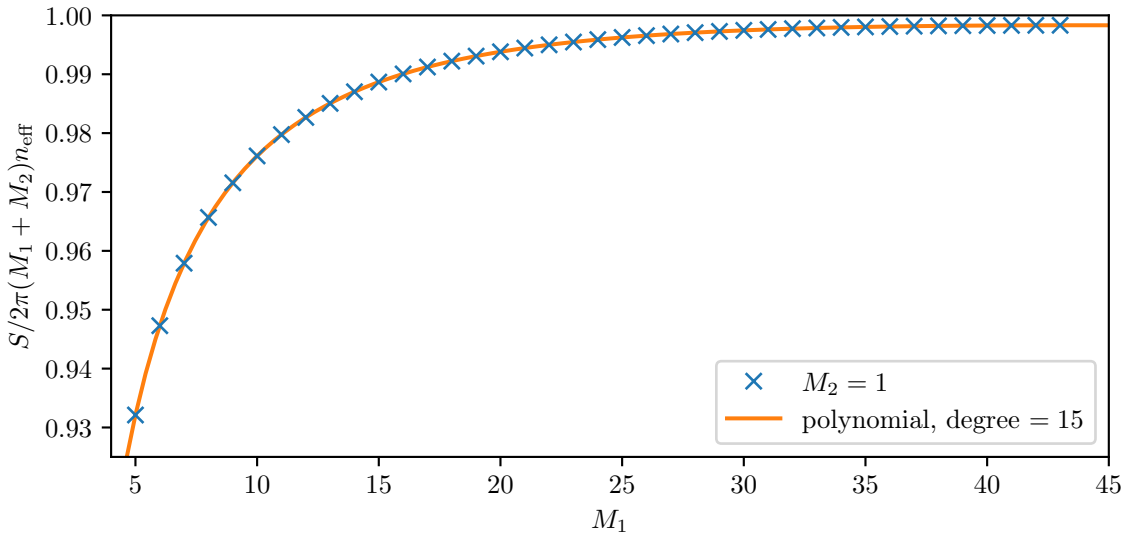

Figure G.2: A polynomial of degree 15 is fitted to the action for the $M_2 = 1$ orbits which allows for using the polynomial to interpolate the action for orbits with higher M_2 as well as for calculating the derivative $\mathrm{d}S/\mathrm{d}M_1$.

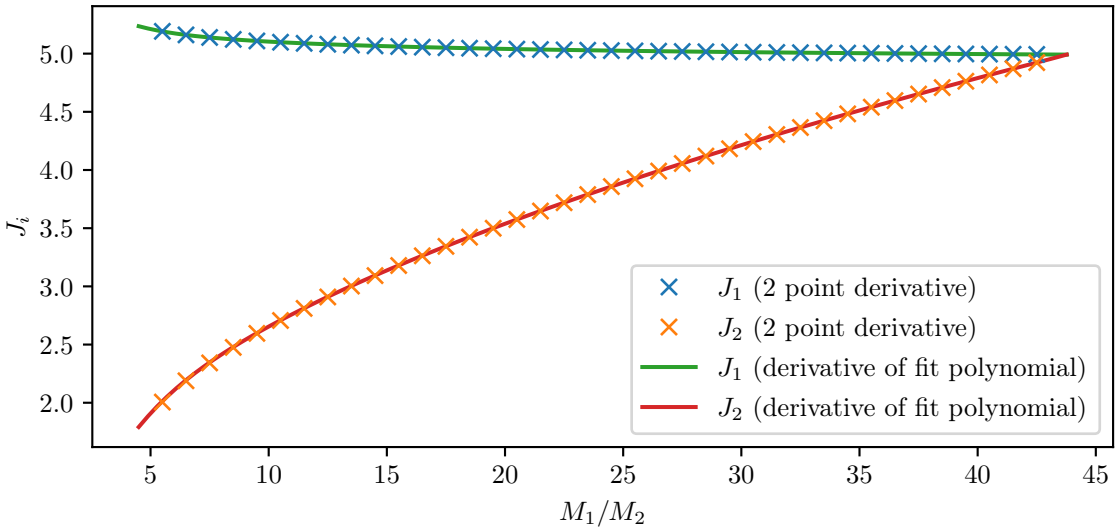

Figure G.3: The plot shows the action variables J_1 and J_2 calculated by using the two-point derivative and the derivative of a polynomial fit to $S(M_1)$. Both ways lead to the same results which is why the polynomial fit is used for further calculations.

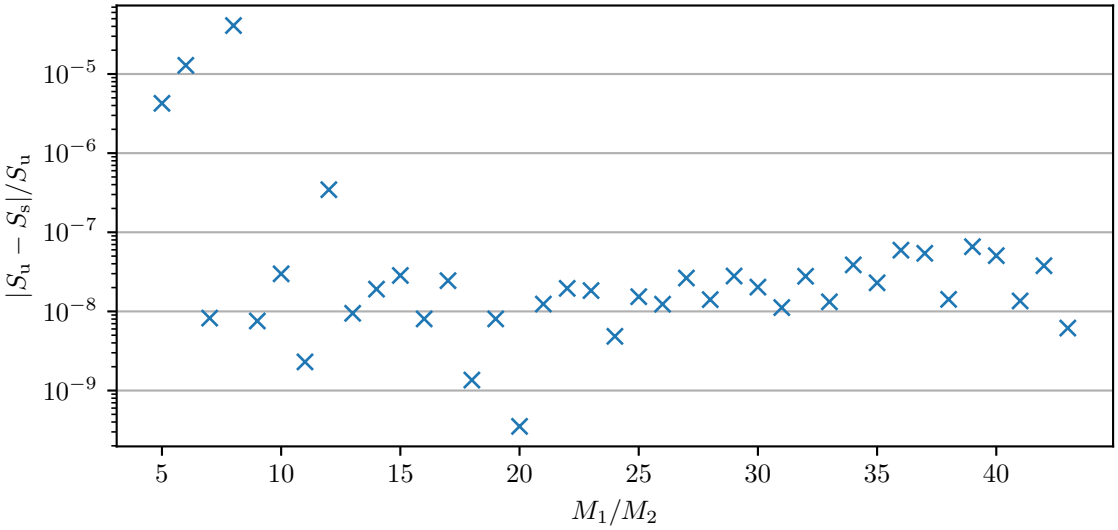

Figure G.4: In figure G.2 a polynomial was used to interpolate the action for different ratios M_1/M_2. But when there are pairs of two orbits a stable (s) and an unstable (u) one for each (M_1, M_2) the question arises whether it is possible to do so. The plot shows that the relative difference in action between the partners is indeed small enough to do so. Furthermore, one can see that the difference is significantly larger for orbit pairs which also have stability eigenvalues λ_{xy} different from one. But even those values are only of order 10^{-5} what means that the fit can be used to calculate a valid average.

When interpolating parameters for higher M_2 one will also need to interpolate the period T. Because the derivative of this fit is not needed it is sufficient to approximate T with a polynomial of degree 10. The coefficients of the fit polynomials for action and period are listed in table G.1. Note that the coefficients seem to be very small for high exponents of x but the full given accuracy is needed to reproduce the polynomial correctly. Additionally the fit coefficients for g''_E from figure 3.7 are given in table G.2.

Table G.1: Coefficients of the fit polynomials for action and period.

quantity	coefficients		range
$S(M_1/M_2)$	$+7.528\,514\,388\,436\,460\,5 \times 10^{-21}$	x^{15}	$M_1/M_2 \in [5, 43]$
	$-3.171\,941\,050\,461\,375\,7 \times 10^{-18}$	x^{14}	
	$+6.127\,021\,378\,984\,744\,4 \times 10^{-16}$	x^{13}	
	$-7.197\,357\,892\,446\,447\,4 \times 10^{-14}$	x^{12}	
	$+5.749\,715\,278\,816\,727\,6 \times 10^{-12}$	x^{11}	
	$-3.308\,814\,143\,903\,416\,7 \times 10^{-10}$	x^{10}	
	$+1.417\,219\,971\,142\,308\,3 \times 10^{-8}$	x^9	
	$-4.602\,404\,830\,656\,148\,8 \times 10^{-7}$	x^8	
	$+1.143\,528\,417\,844\,090\,4 \times 10^{-5}$	x^7	
	$-2.177\,428\,538\,769\,049\,4 \times 10^{-4}$	x^6	
	$+3.161\,381\,743\,579\,337\,9 \times 10^{-3}$	x^5	
	$-3.458\,117\,369\,433\,046\,1 \times 10^{-2}$	x^4	
	$+2.796\,085\,048\,984\,263\,7 \times 10^{-1}$	x^3	
	$-1.640\,224\,500\,146\,046\,3$	x^2	
	$+3.866\,020\,450\,143\,041\,4 \times 10^{1}$	x	
	$+2.851\,636\,009\,038\,511\,3$		
$T(M_1/M_2)$	$-1.881\,934\,799\,312\,289\,3 \times 10^{-13}$	x^{10}	$M_1/M_2 \in [5, 43]$
	$+5.154\,230\,884\,123\,309\,1 \times 10^{-11}$	x^9	
	$-6.244\,393\,934\,727\,318\,7 \times 10^{-9}$	x^8	
	$+4.407\,067\,574\,883\,838\,7 \times 10^{-7}$	x^7	
	$-2.008\,243\,533\,295\,071\,3 \times 10^{-5}$	x^6	
	$+6.188\,201\,923\,025\,073\,2 \times 10^{-4}$	x^5	
	$-1.312\,683\,461\,051\,171\,3 \times 10^{-2}$	x^4	
	$+1.914\,646\,189\,323\,381\,0 \times 10^{-1}$	x^3	
	$-1.890\,730\,715\,542\,091\,6$	x^2	
	$+8.049\,371\,559\,460\,452\,1 \times 10^{2}$	x	
	$-2.814\,561\,669\,418\,478\,1 \times 10^{1}$		

Table G.2: Coefficients of the polynomials fitted to g''_E in figure 3.7.

quantity	coefficients		range
$g''_E(J_1)$	$-5.587\,905\,994\,843\,958\,3 \times 10^7$	x^5	$J_1 \in [4.993, 5.105]$
	$+1.417\,470\,026\,635\,234\,4 \times 10^9$	x^4	
	$-1.438\,282\,141\,542\,306\,1 \times 10^{10}$	x^3	
	$+7.297\,093\,062\,825\,294\,5 \times 10^{10}$	x^2	
	$-1.851\,106\,687\,759\,681\,7 \times 10^{11}$	x	
	$+1.878\,360\,514\,667\,785\,0 \times 10^{11}$		
$g''_E(J_1)$	$-3.156\,448\,119\,932\,510\,3 \times 10^5$	x^5	$J_1 \in [5.105, 5.221]$
	$+8.225\,098\,486\,700\,657\,8 \times 10^6$	x^4	
	$-8.575\,112\,629\,199\,299\,2 \times 10^7$	x^3	
	$+4.471\,014\,655\,465\,763\,8 \times 10^8$	x^2	
	$-1.165\,845\,895\,275\,227\,3 \times 10^9$	x	
	$+1.216\,287\,550\,164\,564\,8 \times 10^9$		

Bibliography

[1] T. Kazimierczuk, D. Fröhlich, S. Scheel, H. Stolz, and M. Bayer. "Giant Rydberg excitons in the copper oxide Cu_2O". In: *Nature* 514.7522 (Oct. 2014), pp. 343–347. ISSN: 1476-4687. DOI: 10.1038/nature13832. URL: https://doi.org/10.1038/nature13832.

[2] EF Gross. "Optical spectrum of excitons in the crystal lattice". In: *Il Nuovo Cimento (1955-1965)* 3.4 (1956), pp. 672–701.

[3] F. Schöne, S.-O. Krüger, P. Grünwald, H. Stolz, S. Scheel, M. Aßmann, J. Heckötter, J. Thewes, D. Fröhlich, and M. Bayer. "Deviations of the exciton level spectrum in Cu_2O from the hydrogen series". In: *Phys. Rev. B* 93 (7 Feb. 2016), p. 075203. DOI: 10.1103/PhysRevB.93.075203. URL: https://link.aps.org/doi/10.1103/PhysRevB.93.075203.

[4] J. M. Luttinger. "Quantum Theory of Cyclotron Resonance in Semiconductors: General Theory". In: *Phys. Rev.* 102 (4 May 1956), pp. 1030–1041. DOI: 10.1103/PhysRev.102.1030. URL: https://link.aps.org/doi/10.1103/PhysRev.102.1030.

[5] Frank Schweiner, Jörg Main, Matthias Feldmaier, Günter Wunner, and Christoph Uihlein. "Impact of the valence band structure of Cu_2O on excitonic spectra". In: *Phys. Rev. B* 93 (19 May 2016), p. 195203. DOI: 10.1103/PhysRevB.93.195203. URL: https://link.aps.org/doi/10.1103/PhysRevB.93.195203.

[6] K Kawaguchi, R Kita, M Nishiyama, and T Morishita. "Molecular beam epitaxy growth of CuO and Cu2O films with controlling the oxygen content by the flux ratio of Cu/O+". In: *Journal of crystal growth* 143.3-4 (1994), pp. 221–226.

[7] Paul R Markworth, Robert PH Chang, Y Sun, GK Wong, and John B Ketterson. "Epitaxial stabilization of orthorhombic cuprous oxide films on MgO (110)". In: *Journal of Materials Research* 16.4 (2001), pp. 914–921.

[8] George F Koster, John O Dimmock, Robert G Wheeler, and Hermann Statz. *Properties of the thirty-two point groups*. Vol. 24. MIT press, 1963.

[9] Jan Ertl. "Adiabatic approximation for the dynamics of magnetoexcitons in Cu_2O". Master's thesis. Universität Stuttgart, Nov. 2019.

[10] R. W. G. Wyckoff. *Crystal Structures, Vol. 1.* New York: Springer-Verlag, 1965.

[11] Frank S. Schweiner. "Theory of excitons in cuprous oxide". PhD thesis. Universität Stuttgart, Dez 2017.

[12] Michel Mom. "Klassische Bahnen und Poincaré-Schnitte in Kupferoxydul mittels adiabatischer Näherung für die Dynamik von Exzitonen". Bachelor's thesis. Universität Stuttgart, Oct. 2019.

[13] Patric Rommel, Jörg Main, Andreas Farenbruch, Johannes Mund, Dietmar Fröhlich, Dmitri R. Yakovlev, Manfred Bayer, and Christoph Uihlein. "Second harmonic generation of cuprous oxide in magnetic fields". In: *Phys. Rev. B* 101 (11 Mar. 2020), p. 115202. DOI: 10.1103/PhysRevB.101.115202. URL: https://link.aps.org/doi/10.1103/PhysRevB.101.115202.

[14] Patric Rommel, Jörg Main, Andreas Farenbruch, Dmitri R. Yakovlev, and Manfred Bayer. "Exchange interaction in the yellow exciton series of cuprous oxide". In: *Phys. Rev. B* 103 (7 Feb. 2021), p. 075202. DOI: 10.1103/PhysRevB.103.075202. URL: https://link.aps.org/doi/10.1103/PhysRevB.103.075202.

[15] Frank Schweiner, Jörg Main, Günter Wunner, and Christoph Uihlein. "Even exciton series in Cu_2O". In: *Phys. Rev. B* 95 (19 May 2017), p. 195201. DOI: 10.1103/PhysRevB.95.195201. URL: https://link.aps.org/doi/10.1103/PhysRevB.95.195201.

[16] JR Rydberg. "London, Edinburgh, Dublin Phil. Mag". In: *J. Sci* 29 (1890), pp. 331–7.

[17] Jörg Main. *Nichtlineare Dynamik*. lecture Notes. 2014.

[18] Michael Victor Berry and Michael Tabor. "Closed orbits and the regular bound spectrum". In: *Proceedings of the Royal Society of London. A. Mathematical and Physical Sciences* 349.1656 (1976), pp. 101–123.

[19] Martin C Gutzwiller. "Periodic orbits and classical quantization conditions". In: *Journal of Mathematical Physics* 12.3 (1971), pp. 343–358.

[20] Martin C Gutzwiller. *Chaos in Classical and Quantum Mechanics*. New York: Springer-Verlag, 1990.

[21] Jonathan Luft. "Closed-Orbit Theorie für Magnetoexzitonen in Kupferoxydul". Master's thesis. Universität Stuttgart, 2018.

[22] C. Deter. "Klassische Bahnen in Kupferoxydul unter Berücksichtigung des Quasispins". Bachelor's thesis. Universität Stuttgart, 2019.

[23] Jan Ertl, Patric Rommel, Michel Mom, Jörg Main, and Manfred Bayer. "Classical and semiclassical description of Rydberg excitons in cuprous oxide". In: *Phys. Rev. B* 101 (24 June 2020), p. 241201. DOI: 10.1103/PhysRevB.101.241201. URL: https://link.aps.org/doi/10.1103/PhysRevB.101.241201.

[24] Franz Schwabl. *Quantenmechanik für Fortgeschrittene (qm ii)*. Springer-Verlag, 2008.

[25] Paul Kustaanheimo, A Schinzel, H Davenport, and E Stiefel. "Perturbation theory of Kepler motion based on spinor regularization." In: *Journal für die reine und angewandte Mathematik* 1965.218 (1965), pp. 204–219.

[26] C.J. Budd, A. Iserles, and Benedict Leimkuhler. "Reversible adaptive regularization: perturbed Kepler motion and classical atomic trajectories". In: *Philosophical Transactions of the Royal Society of London. Series A: Mathematical, Physical and Engineering Sciences* 357.1754 (1999), pp. 1101–1133. DOI: 10.1098/rsta.1999.0366. eprint: https://royalsocietypublishing.org/doi/pdf/10.1098/rsta.1999.0366. URL: https://royalsocietypublishing.org/doi/abs/10.1098/rsta.1999.0366.

[27] Kenneth E. Hillstrom Burton S. Garbow and Jorge J. More. *MINPACK subroutine HYBRD1*. https://www.math.utah.edu/software/minpack/minpack/hybrd1.html. Accessed: 2021-02-27. 1980.

[28] I. Gladwell R.W. Brankin and L.F. Shampine. *RKSUITE*. http://www.netlib.org/ode/rksuite/. Accessed: 2021-03-01. 1991.

[29] Jörg Main and Günter Wunner. "Periodic Orbit Quantization of Mixed Regular Chaotic Systems". In: *Phys. Rev. Lett.* 82 (15 Apr. 1999), pp. 3038–3041. DOI: 10.1103/PhysRevLett.82.3038. URL: https://link.aps.org/doi/10.1103/PhysRevLett.82.3038.

[30] Denis Ullmo, Maurice Grinberg, and Steven Tomsovic. "Near-integrable systems: Resonances and semiclassical trace formulas". In: *Phys. Rev. E* 54 (1 July 1996), pp. 136–152. DOI: 10.1103/PhysRevE.54.136. URL: https://link.aps.org/doi/10.1103/PhysRevE.54.136.

[31] Moritz Schumacher. Master's thesis in preparation. 2021.

[32] Moritz Schumacher and Patric Rommel. Private communication. 2021.

[33] Jacob Fuchs, Jörg Main, Holger Cartarius, and Günter Wunner. "Harmonic inversion analysis of exceptional points in resonance spectra". In: *Journal of Physics A: Mathematical and Theoretical* 47.12 (Mar. 2014), p. 125304. DOI: 10.1088/1751-8113/47/12/125304. URL: https://doi.org/10.1088/1751-8113/47/12/125304.

[34] J W Hodby, T E Jenkins, C Schwab, H Tamura, and D Trivich. "Cyclotron resonance of electrons and of holes in cuprous oxide, Cu2O". In: *Journal of Physics C: Solid State Physics* 9.8 (Apr. 1976), pp. 1429–1439. DOI: 10.1088/0022-3719/9/8/014. URL: https://doi.org/10.1088/0022-3719/9/8/014.

[35] O. Mandelburg, U. Rössler, and M. Schulz. *Landolt-Börnstein - Group III Condensed Matter*. Berlin Heidelberg: Springer-Verlag, 1998.

Danksagung (Acknowledgment)

Dies ist die Stelle, and der ich den vielen Menschen danken möchte die mir geholfen haben diese Arbeit zu schreiben.

Zuerst möchte ich mich bei meinem Betreuer Jan Ertl, M.Sc. und meinem Prüfer Apl. Prof. Dr. Jörg Main bedanken, die wohl am meisten beigetragen haben. Als mein Betreuer für die Masterarbeit hat Jan sehr gute Arbeit geleistet, mich unterstützt und sich Zeit für meine Anliegen und Vorschläge genommen. Auch Jörg war stets an meinen Fortschritten interessiert und hat sich mit vielen interessanten Gedanken eingebracht.

Außerdem bedanke ich mich bei Prof. Dr. Maria Daghofer dafür, den Mitbericht meiner Arbeit übernommen zu haben, und auch dafür stets zeitnah erreichbar gewesen zu sein.

Des weiteren möchte ich der aktuellen Exzitonen Arbeitsgruppe des Instituts für Theoretische Physik 1 (ITP1) danken: Jörg Main, Jan Ertl, Patric Rommel, M.Sc., Patrick Egenlauf, B.Sc. und Moritz Schumacher, B.Sc. Ihr seid ein sehr motiviertes und kommunikatives Team mit interessanten Diskussionen und einem offenen Ohr bei Fragen und Ideen.

Außerdem möchte ich Michel Mom, B.Sc. danken, der mit seiner Bachelorarbeit die Vorarbeit für meine Masterarbeit gelegt hat, zusammen mit Jan Ertl. Es soll auch nicht unerwähnt bleiben, dass sie mir ein Simulationsprogramm hinterlassen haben, dass ich in Teilen weiter benutzen konnte.

Darüber hinaus will ich mich bei unserem Systemadministrator Johannes Reiff, M.Sc. und Frau Monika Bund für die sehr gute Verwaltung und Organisation am Institut bedanken, welche mir die Arbeit sehr erleichtert hat.

Nun steht das Jahr 2020/21 ganz im Zeichen der Corona-Krise und auch am ITP1 ist diese nicht spurlos vorübergegngen. Ich befand mich die meiste Zeit im Homeoffice ohne den direkten Kontakt zu anderen Studenten und Institutskollegen. Umso wichtiger war es für mich, dass wir täglich unsere virtuelle Kaffeerunde abgehalten haben. Vierzig Minuten, in denen wir privat oder (zum Leidwesen der TST Arbeitsgruppe) über Exzitonen gesprochen haben. An dieser Stelle möchte ich mich bei den ständigen Mitgliedern der Kaffeerunde bedanken: Die gesamte Exzitonen Gruppe sowie Johannes Reiff, Micha Schleeh, B.Sc. und Melissa Lober, B.Sc.

Und natürlich will ich auch den anderen Forschern und Arbeitsgruppen danken, die sich mit Exzitonen beschäftigen, allen voran Moritz Schumacher und Patric Rommel, die mir Fouriertransformierte quantenmechanische Spektren zum Vergleich gegeben haben.

Außerdem durfte ich am „4th International Workshop on Rydberg Excitons in Semiconductors“ teilnehmen, bei dem ich viele interessante Vorträge hören konnte und noch sehr viel mehr über Exzitonen gelernt habe. Auch wenn die Konferenz aus gegebenem Anlass nur online stattfinden konnte war sie außerordentlich gut organisiert. Ein Dankeschön an die Organisatoren in Rostock und die Teilnehmer aus allen Ecken der Welt.

Darüber hinaus möchte ich meiner Familie danken, besonders meinen Eltern, bei denen ich noch wohne. Ihr habt mich während meines Studiums immer unterstützt, sei es finanziell, mental oder durch das unschlagbar leckere und vielseitige Mittagessen meiner Mutter.

Erklärung

Ich versichere,

- dass ich diese Masterarbeit selbstständig verfasst habe,
- dass ich keine anderen als die angegebenen Quellen benutzt und alle wörtlich oder sinngemäß aus anderen Werken übernommenen Aussagen als solche gekennzeichnet habe,
- dass die eingereichte Arbeit weder vollständig noch in wesentlichen Teilen Gegenstand eines anderen Prüfungsverfahrens gewesen ist,
- und dass das elektronische Exemplar mit den anderen Exemplaren übereinstimmt.

Stuttgart, den 18. März 2021 *Michael Marquardt*